The Astrophysical Journal Supplement Series, 175:229–276, 2008 March

MODELS OF THE SOLAR CHROMOSPHERE AND TRANSITION REGION FROM SUMER AND HRTS OBSERVATIONS: FORMATION OF THE EXTREME-ULTRAVIOLET SPECTRUM OF HYDROGEN, CARBON, AND OXYGEN

Eugene H. Avrett and Rudolf Loeser
Harvard-Smithsonian Center for Astrophysics, 60 Garden Street, Cambridge, MA 02138; avrett@cfa.harvard.edu
Received 2007 May 21; accepted 2007 September 13

ABSTRACT

We present the results of optically thick non-LTE radiative transfer calculations of lines and continua of H, C I–IV, and O I–VI and other elements using a new one-dimensional, time-independent model corresponding to the average quiet-Sun chromosphere and transition region. The model is based principally on the Curdt et al. SUMER atlas of the extreme ultraviolet spectrum. Our model of the chromosphere is a semiempirical one, with the temperature distribution adjusted to obtain optimum agreement between calculated and observed continuum intensities, line intensities, and line profiles. Our model of the transition region is determined theoretically from a balance between (*a*) radiative losses and (*b*) the downward energy flow from the corona due to thermal conduction and particle diffusion, and using boundary conditions at the base of the transition region established at the top of the chromosphere from the semiempirical model. The quiet-Sun model presented here should be considered as a replacement of the earlier model C of Vernazza et al., since our new model is based on an energy-balance transition region, a better underlying photospheric model, a more extensive set of chromospheric observations, and improved calculations. The photospheric structure of the model given here is the same as in Table 3 of Fontenla, Avrett, Thuiller, & Harder. We show comparisons between calculated and observed continua, and between the calculated and observed profiles of all significant lines of H, C I–IV, and O I–VI in the wavelength range 67–173 nm. While some of the calculated lines are not in emission as observed, we find reasonable general agreement, given the uncertainties in atomic rates and cross sections, and we document the sources of the rates and cross sections used in the calculation. We anticipate that future improvements in the atomic data will give improved agreement with the observations.

Subject headings: atomic data — line: profiles — radiative transfer — Sun: chromosphere — Sun: transition region — Sun: UV radiation

1. INTRODUCTION

The Curdt et al. (2001) SUMER atlas of the quiet-Sun disk-center spectrum between 67 and 161 nm together with the corresponding Brekke (1993a) HRTS spectrum to 173 nm contain a wealth of information about the structure and composition of the upper photosphere, chromosphere, transition region, and low corona, as well as about some of the detailed atomic processes involved in producing the spectra. These observations provide data that can be used to reveal the structure of the solar atmosphere.

The Curdt et al. and Brekke observations correspond to the combined intensities from the brighter network regions and the fainter internetwork regions. The model in this paper corresponds to these combined intensities, but we comment briefly here on the observed spatial and temporal variations. At disk center, the SUMER continuum intensity in the network is greater than in internetwork regions, typically by a factor of 3 shortward of 110 nm and a factor of 2 at longer wavelengths. In many lines the network-to-internetwork intensity ratios are much larger than the continuum ratios, particularly at short wavelengths. These continuum and line ratios are plotted in Fig. 4 of Curdt et al. (2001) (and in our Fig. 1 below). Observed temporal variations are often smaller than these spatial variations, typically around 40% (Wilhelm et al. 2005; Wilhelm & Kalkofen 2003). Larger temporal variations were reported by Carlsson et al. (1997) (factors of 2 as shocks pass, sometimes a factor of 3 within about 30 s). We find that such observed spatial and temporal intensity variations in quiet regions can be the result of kinetic temperature variations of order 10% in our model calculations (Avrett 2006, 2007a). Given these relatively moderate temperature variations, it is of interest to determine the temperature distribution with height in the atmosphere corresponding to the average quiet-Sun spectrum, based on the extensive SUMER and HRTS observations. Separate models of network and internetwork regions, and models representing temporal variations, are needed for detailed studies of chromospheric heating, but here we model only the average quiet Sun.

Carlsson & Stein (1992, 1994, 1995, 1997, 2002) simulated chromospheric heating in internetwork regions by acoustic shock waves (see the recent review by Carlsson 2007). The Carlsson & Stein calculated chromospheric intensity fluctuations are much larger than observed, and their models predict *intermittent* line emission, contrary to the persistent, ubiquitous emission seen in SUMER observations. Carlsson et al. (1997) examined the SUMER spectrum to see if any chromospheric lines ever appeared in absorption, corresponding to intervals of time between the passage of strong shocks. They concluded that, contrary to their model predictions, all lines showed emission at all locations and at all times, and that “something important is missing from the calculations.” Fossum & Carlsson (2005a, 2005b, 2006) subsequently concluded that *TRACE* observations (Handy et al. 1999) were not consistent with chromospheric heating by acoustic waves, and they suggested that magnetic fields might play a major role in heating the internetwork chromosphere, but they did not discuss specific mechanisms. Chromospheric heating by motions that interact with magnetic fields has been discussed by Fontenla (2005) and by Kazeminezhad & Goodman (2006). Views in support of acoustic heating are discussed by Ulmschneider et al. (2005) and by Cuntz et al. (2007). See also the earlier comments on the Carlsson & Stein modeling by Kalkofen et al. (1999) and

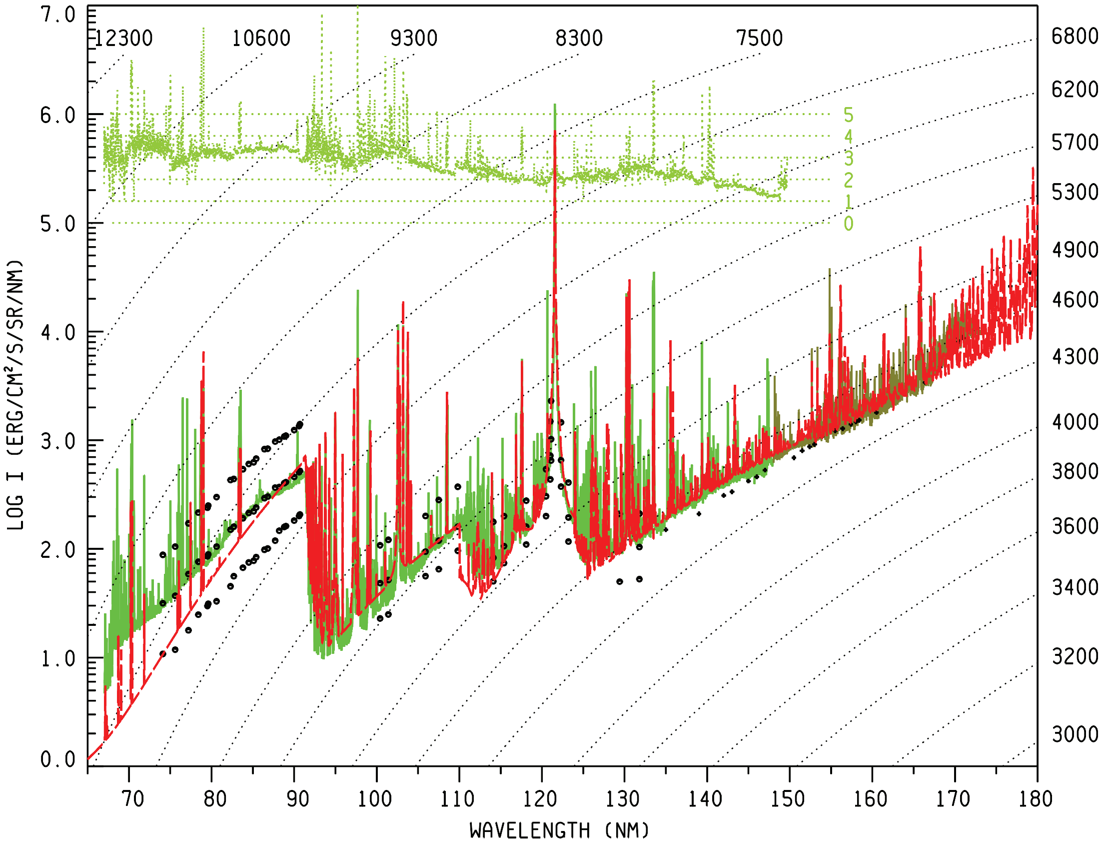

FIG. 1.—SUMER (*solid green line*), HRTS (*solid brown line*), and other quiet-Sun observations between 67 and 173 nm, and the spectrum calculated from model C7 (*dashed red line*). The plot at the top of the figure shows the observed bright-network to cell-interior intensity ratio (scale 0–5) vs. wavelength.

Kalkofen (2001). Judge et al. (2001) give a detailed discussion of chromospheric oscillations on the basis of *SOHO* and *TRACE* observations. An up-to-date review of semiempirical and theoretical modeling of the solar chromosphere is given by Carlsson (2007). For a general introduction, see Rutten (2007).

Our model, based on SUMER and HRTS average quiet-Sun observations, is one-dimensional and time independent and does not include a magnetic field. We have argued in two recent papers (Avrett et al. 2006; Avrett 2006) that the observed spatial and temporal variations of chromospheric intensities correspond to temperature variations of only a few hundred degrees, but time-dependent studies show effects of long radiative-recombination times that could mask the effects of sporadic heating, particularly in the upper chromosphere where hydrogen is partially ionized. Kneer (1980), Carlsson & Stein (2002), Leenaarts & Wedemeyer-Böhm (2006), and Leenaarts et al. (2007) have shown that ionization/recombination timescales in hydrogen can be longer than typical hydrodynamical timescales in the solar chromosphere. We assume that the kinetic temperature variations are not significantly larger than the moderate brightness temperature variations that are observed with high spatial and temporal resolution.

An objective of this paper is to determine how well a model of the average quiet Sun can account for the observed quiet-Sun EUV line and continuum spectrum. Our one-dimensional, steady-state modeling has many features in common with models that include spatial and temporal variations since both solve many of the same basic equations. The models involving temporal and spatial variations should, ideally, include at least the level of detail included in the non-LTE calculations reported here.

Our one-dimensional, time-independent model is semiempirical, based on a fit to the observed spectrum. A theoretical one-dimensional, time-independent model of the solar chromosphere was calculated by Anderson & Athay (1989a). Instead of adjusting the temperature distribution to get agreement between calculated and observed spectra, they introduced a distribution of nonradiative heating to produce a temperature distribution similar to that in the semiempirical average model of Vernazza et al. (1981, hereafter VAL). They found 14 kW m $^{-2}$ as the nonradiative input needed to balance the chromospheric radiative losses (see Carlsson 2007).

Much of this paper is concerned with the rates and cross sections of atomic interactions that influence the calculated spectrum. We include collisions with hydrogen atoms in the low chromosphere for atomic transitions that can be treated as Rydberg transitions but find that such collisions do not greatly affect the results shown here.

We give selected results for the continua and lines of H, C I–IV, and O I–VI in order to provide a reasonable overall presentation of the results of our average quiet-Sun model, extending from the low chromosphere into the low corona. Our full calculations also include He I–II, N I–IV, Ne I–VIII, Na I–II, Mg I–II, Al I–II, Si I–IV, S I–IV, Ca I–II, and Fe I, but we defer the presentation and discussion of these results to subsequent papers. We have not included all published rates and cross sections and line-broadening parameters for C I–IV and O I–VI since this would be a greater undertaking than is feasible in this study. We have tried to include all available data we consider to be critical but use many approximations for rates that seem to us to be of lesser importance. For example, in many cases we use the analytic fits of Verner et al. (1996) to the available cross sections for photoionization from the ground level of various atoms and ions, and use the hydrogenic approximation for levels 2 and higher, rather than adopt the

TABLE 1

V versus $n_{\rm H}$

log $n_{\rm H}$	V (km s^{-1})
16.0	0.34
15.5	0.37
15.0	0.4
14.5	0.5
14.0	0.6
13.5	0.7
13.0	1.0
12.5	1.5
12.0	2.5
11.8	3.1
11.5	3.8
11.3	4.7
11.0	6.0
10.8	7.6
10.5	9.3
10.3	11.4
10.0	15.0
9.8	19.8
9.5	24.5
9.3	29.3
$\leq$9	34.0

extensive calculated cross sections as functions of frequency, including many resonances, from the Opacity Project.[1] We hope to introduce such improvements in subsequent papers.

Given the assumed atomic data, and the solar elemental abundances, the entire calculated line and continuum spectrum depends on two specified functions of height in the photosphere and chromosphere: temperature $T(h)$ and a turbulent pressure velocity $V_{\rm tp}(h)$. The effect of this second function is to distend the atmosphere a few hundred kilometers so the transition region between the chromosphere and corona occurs at a greater height, consistent with limb observations, outside of spicules. As in earlier papers we assume that $V_{\rm tp}$ is the same as the nonthermal, microturbulent velocity $V_{\rm nt}$ that, in principle, can be inferred from lines, formed at various heights, that have observed Doppler line widths larger than thermal values. [Hereafter, these two identical functions of height are called $V(h)$.] In the photosphere out to the height of 400 km (where the total hydrogen density $n_{\rm H}$ is 10^{16} cm^{-3}) we use $V(h)$ from Fontenla et al. (2006, Table 3 for model C). Above this height we obtain $V(h)$ by interpolation from the values of V versus log $n_{\rm H}$ given in Table 1 (as a simpler approach than giving V for each value of h).

The value 34 km s^{-1} at $n_{\rm H} = 10^9$ cm^{-3} in Table 1 is based on the observed nonthermal Doppler width of the O vi lines at 103.2 and 103.8 nm determined by Warren et al. (1997). We arbitrarily let $V = 34$ km s^{-1} for $n_{\rm H} < 10^9$ cm^{-3}.

This approximate table of values has been obtained not from theory but in a simple way from the observed widths of lines included in the present study. For example, in our model calculation we find that for the 6/1 C i triplet lines at 161 nm (see Tables 3 and 4 for our notation based on level indices), the maximum contribution to the line-center emergent intensity is located in the low chromosphere at a height of 854 km where the temperature in our model is 5430 K and where the total hydrogen density is $n_{\rm H} = 9.1 \times 10^{13}$ cm^{-3}. (See Tables 27 and 26.) Then from Table 1 we obtain $V = 0.61$ km s^{-1}. The observed Doppler widths of these lines are close to thermal values, and a larger V would make the calculated line cores too broad. At much greater heights in the model calculation, the 2/1 C iv doublet lines at 155 nm have their maximum contribution to the line-center emergent intensities at 2170 km, where $T = 68{,}000$ K and $n_{\rm H} = 3.8 \times 10^9$ cm^{-3} and where we have $V = 23$ km s^{-1}. The observed Doppler widths of these lines are much larger than thermal values, and using a smaller V would make the calculated lines too narrow. We subsequently show, in Figures 9–12, calculated profiles with and without this nonthermal broadening, and with and without a further convolution of the calculated profiles that is needed before they can be directly compared with the observed ones. This convolution also broadens the lines, masking part of the effects of nonthermal broadening. Thus, the values given in Table 1 are only schematic and need to be refined by comparisons with observations that have higher spatial and temporal resolution than the ones considered here. A careful analysis of the nonthermal velocities of lines formed at different temperatures in the transition region is given by Akiyama et al. (2005) based on SUMER observations. We believe that the values in Table 1 (which are model dependent) are generally consistent with their results.

Given $V(h)$ determined in this way, we obtain the temperature distribution $T(h)$ from a best fit to the observations. A different choice of $V(h)$ would lead to a different $T(h)$, mainly due to a change in the height scale. (Increasing V increases the pressure at a given height and causes $n_{\rm H}$ to decrease less rapidly with height.) We discuss the $V_{\rm nt}$ and $V_{\rm tp}$ distributions further in § 10.

We adopt a minimum temperature of 4400 K simply to match our present non-LTE calculations to the average SUMER and HRTS continua near 160 nm, even though molecular observations indicate lower minimum temperatures. In § 3 we comment on the problem of modeling the temperature-minimum region consistent with observations of continua and lines at different wavelengths. Fontenla et al. (2007) have an alternative explanation to account for the temperature-minimum and molecular observations, in which the temperature has a lower minimum value located at a greater height compared with the model given here.

In the transition region, the temperature distribution is determined theoretically using the boundary conditions established at the top of the model chromosphere, based on a balance between (1) the inward transport of energy from the corona by thermal conduction and particle diffusion and (2) the net radiative losses, from Cox & Tucker (1969) (see Fontenla et al. 1990, 1991, 1993, 2002). This calculation does not include any other nonradiative heating in the transition region.

2. OVERVIEW OF THE RESULTS

Figure 1 shows, in green for wavelengths 67–147 nm, the SUMER atlas spectrum from the average quiet Sun at disk center from Curdt et al. (2001) and, in brown for wavelengths 147–173 nm, the HRTS quiet-Sun spectrum from Brekke (1993a). The SUMER atlas spectrum extends to 160.9 nm but includes an additional second-order intensity contribution from the Lyman continuum. The HRTS spectrum extends to 119 nm but lacks good absolute calibration for wavelengths below about 145 nm. We have joined the two spectra at 147 nm where they agree. (The Curdt et al. SUMER atlas also includes spectra from an equatorial coronal hole and from a sunspot, but we do not discuss these observations here.) In this figure and in subsequent ones the scale on the left is the log of the disk-center intensity in ergs s^{-1} sr^{-1} cm^{-2} nm^{-1}. Brightness temperatures, in K, corresponding to these intensities are included as dashed lines for reference. The observed ratio of bright-network to cell-interior intensity from the Curdt et al. atlas is superposed across the upper left part of this figure.

---

[1] Available at http://aeldata.nist.gov/nist_atomic_spectra.html.

The plus symbols in Figure 1 indicate the disk-center intensity at continuum wavelengths measured by Samain (1978, 1980). The upper, middle, and lower circular symbols are the observed *Skylab* continuum intensities from VAL corresponding to bright network, average quiet Sun, and faint cell centers, respectively, indicating the spatial variation of observed intensities in quiet regions.

The distribution plotted in red is the intensity calculated from our current model of the average quiet Sun, which we call model C7, using the Pandora computer program of Avrett & Loeser (2003). The chromospheric temperature distribution was adjusted by trial and error to obtain an optimum match to the overall continuum intensity distribution. Some additional adjustments were made to improve general agreement with line intensities.

The chromospheric temperature distribution up to the base of the transition region was adjusted to fit the continuum observations. The atmospheric parameters at the top of the chromosphere provide boundary conditions for an energy-balance calculation of the transition region structure, as described earlier. In later sections we will show that, even though there are substantial uncertainties in many of the rates and cross sections used in our calculations, most of the calculated line profiles are in general agreement with the observed ones. However, in some cases the calculated line intensities disagree with observations in showing very little emission. In many other cases, the calculated lines are in emission with central aborption features that are too narrow to appear in the observed lines at the resolution of the SUMER atlas spectrum (see § 14).

The temperature distribution for model C7 is shown in Figure 2 along with plots of the distributions versus height of the contributions dI/dh to the emergent continuum intensities at the wavelengths 160, 150, 140, 130, 120, 110, 91.17, 80, and 70 nm in the extreme ultraviolet, and at the long wavelengths 0.2, 0.5, 1, 2, and 5 mm, and 1, 2, and 5 cm. The contribution functions shown in Fig. 2 for each wavelength represent the contribution to the emergent intensity I per unit height, normalized so that the maximum contribution plotted is the same in each case. Each shaded distribution is shown as a symmetric plot about a horizontal line. (See Fig. 14 in § 15 for plots of normalized values of dI/dh vs. h.) At the long wavelengths in Figure 2 the increase of opacity with increasing wavelength (due mostly to hydrogen free-free absorption) causes the intensity to be formed progressively higher in the atmosphere, just as the increasing opacity with decreasing wavelength between 160 and 70 nm (due mostly to bound-free absorption by various neutral atoms) causes the intensity to be formed progressively higher. This figure shows that at some wavelengths the intensity originates in a fairly localized region in height, while at other wavelengths the formation region is extended over a significant range of heights.

The contribution function for 110 nm (the head of the C I level-1 continuum) in Figure 2 also approximately represents the continuum underlying the many emission lines in the interval between 110 nm and 91.17 (the head of the hydrogen level-1 continuum). Many carbon and oxygen lines are formed in this interval, as we show later in Figures 19 and 23.

The contribution functions indicate where in the atmosphere, and over what extent of height, the intensity at any wavelength is formed. Generally we determine the model by raising or lowering the temperature in the relevant height range to raise or lower the computed intensity to match the observed intensities (except in the special case of the Lyman continuum intensity as discussed in § 12).

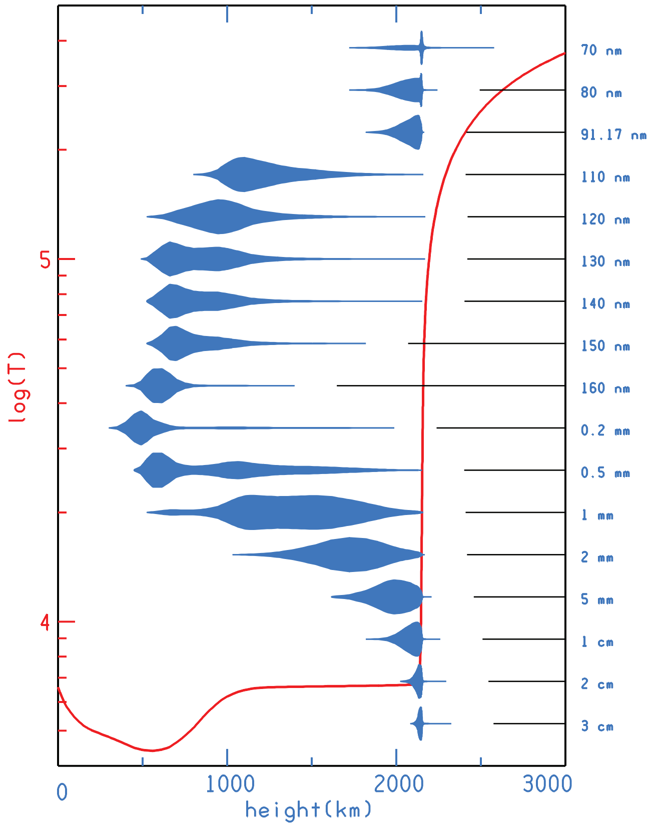

FIG. 2.—Model C7 temperature distribution along with plots of the contributions dI/dh to the continuum intensities at 160, 150, 140, 130, 120, 110, 91.17, 80, and 70 nm in the extreme ultraviolet, and at the long wavelengths 0.2, 0.5, 1, 2, and 5 mm and 1, 2, and 5 cm. The dI/dh plots shown here are nomalized to a common maximum value.

Figure 3 shows the available observations of brightness temperature in the wavelength range 0.04–40 mm, from Loukitcheva et al. (2004), Boreiko & Clark (1987), and Degiacomi et al. (1985), along with the full-disk brightness temperature distribution that we compute from model C7. Since LTE (with no scattering) prevails in this wavelength range, the observed brightness temperatures correspond to the kinetic temperatures near unit monochromatic optical depth, and we can compare our model temperatures directly with the observed values (which represent spatial and temporal averages). The scatter in the available observations permits only an approximate check on our model temperature distribution, but the model is roughly consistent with the observations in showing similar minimum temperatures, a rapid temperature increase in the low chromosphere, a chromospheric plateau, and an abrupt temperature increase in the transition region. These observations correspond to large areas of the solar disk that include active regions when they are present, but corrections were made to exclude the effect of active regions. Hence, the figure shows little correlation between the observed brightness temperaures and the level of solar activity at the time of observation. Because mostly full-disk observations are shown in Figure 3 for the longer wavelengths, we plot the calculated brightness temperatures corresponding to the solar flux. In the minimum region, however, the observations correspond to central rather than to full-disk areas. Our calculated disk-center brightness temperatures near 0.4 mm are lower than the calculated flux brightness temperatures in Figure 3 by 100-200 K (in rough agreement with the minimum brightness temperature values in Fig. 1). Loukitcheva et al. give the area of the solar disk corresponding to each observation.

Figure 3 shows that our calculated brightness temperatures near 0.4 mm are higher than observed. Lower temperature-minimum

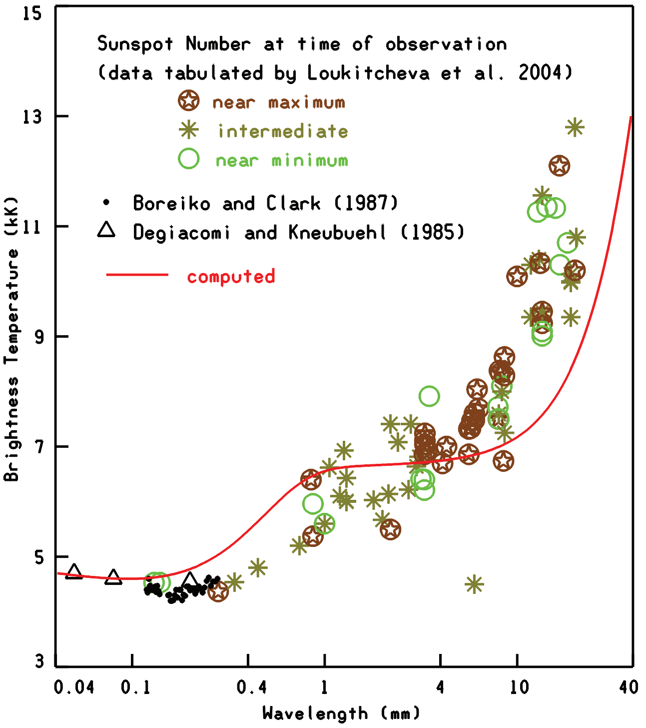

Fig. 3.—Observed brightness temperatures from 0.04 to 40 mm (4 μm–4 cm) and the full-disk brightness temperature distribution calculated from model C7. The observations in the minimum region correspond to areas near disk center while those at longer wavelengths used beam sizes from 2″ to 15″. See Loukitcheva et al. (2004).

values would not match observations near 160 nm, but it should be noted that temporal and spatial temperature fluctuations are linearly averaged in the millimeter region but are averaged according to $\exp(-h\nu/kT)$ in the UV, giving greater weight in the UV to higher temperatures. Thus, our average model that matches observations around 160 nm may overestimate the minimum temperature.

Figure 3 also shows that the calculated increase in the transition-region occurs at longer wavelengths than observed. Moving the model transition region to a smaller height, which would move the location of the transition region in Figure 3 to a shorter wavelength, would cause problems in matching other observations. This lack of agreement could be related to our difficulty in matching the slope of the Lyman continuum, discussed in § 12. These inconsistencies require further study.

3. PREVIOUS MODELING

VAL used *Skylab* observations of the quiet Sun in the EUV wavelength range 42–132 nm to model the inhomogeneous structure of the solar chromosphere. Their models A–F were based on six observed brightness components, ranging from a dark cell center to a very bright network element. Model C represented the average quiet Sun. In the transition region just above 20,000 K, an artificial temperature plateau had to be introduced to provide sufficient thickness of the atmosphere in this temperature range to account for the intensity of the observed hydrogen Lyα line, assuming local statistical equilibrium. Such a plateau is no longer needed since the transition region is now treated theoretically by the methods developed by Fontenla et al. (1990, 1991, 1993, 2002) as described later in this section.

Here we digress briefly to comment on the temperature minimum problem, which is not discussed elsewhere in this paper. The *Skylab* chromospheric observations provided no information about the temperature minimum and photosphere, but the VAL models included these regions for completeness using other data. The temperature minimum region presented a difficulty then, and remains a problem to be resolved.

Observations pertaining to the minimum region include (1) the UV continuum near 160 nm, (2) the H1 and K1 intensity minima in the near wings of the Ca II H and K lines, (3) the submillimeter brightness temperatures near 150 μm, and (4) the central intensities of the strong infrared lines of carbon monoxide (Ayres 2002, 2003).

1. The observed 160 nm minimum brightness temperature is roughly 4400 K, which implies either (*a*) a comparable minimum kinetic temperature if the Si I level populations are roughly in LTE or (*b*) temperatures as low as 4100 K if there are substantial departures from LTE. Or, as discussed by Fontenla et al. (2007), cool temperatures could occur in a region so limited in optical thickness that while the region contributes substantially to temperature-sensitive molecular aborption, very little absorption occurs in other spectra. (A similar effect was shown by Avrett 2003.)

2. According to Cram & Damé (1983) the H1 and K1 minima have an average brightness temperature of about 4400 K, and vary from about 4200 K to 4600 K, respectively, in the faintest and brightest 10% of quiet-Sun areas observed at high spatial resolution (see Avrett 1985, Figs. 3 and 4). Model calculations with gradual temperature variations with height show a close correspondence between the H1 and K1 brightness temperatures and the minimum atmospheric temperature.

3. Two measurements of the lowest observed average submillimeter brightness temperatures give (*a*) 4550 K at 200 μm (Degiacomi et al. 1985) and (*b*) 4200 K at 160 μm (Boreiko & Clark 1987). Model calculations with gradual temperature variations with height indicate that the minimum brightness temperature in this wavelength region corresponds to the minimum atmospheric temperature, but the observations in this region are spatial (and temporal) averages.

4. The strongest space- and time-averaged infrared CO absorption lines are observed to have central brightness temperatures of 4100 K at disk center (see Avrett 1995), and 3800 K near the limb (Noyes & Hall 1972). Studies by Ayres & Wiedemann (1989) and Uitenbroek (2001) demonstrate that these CO lines are formed in LTE, so that average kinetic temperatures comparable to these low brightness temperatures should occur somewhere in the atmosphere.

A minimum temperature of 4170 K was chosen for VAL model C. Later Avrett (1985) corrected this to 4400 K to agree with Ca II observations. Further corrections of the deep layers of the photosphere to account for the observed brightness temperature maximum at 1.6 μm were made by Maltby et al. (1986) and by Fontenla et al. (2006, Table 3 for model C).

Thus, there is a disparity at disk center between the 4100 K CO value and the 4400 K value from the three other sources described above, unless the low temperatures occur in regions that are limited in geometrical thickness (as noted in point 1 above). This 300 K difference is much larger than observational errors or temporal variations. Avrett (2003) attempted to resolve this difference by pointing out that, first, the strongest CO lines could be formed in the temperature-minimum region at a height near 500 km, rather than near 800 km in the midchromosphere as determined by steady-state modeling (see Ayres 2003), thus making this a temperature-minimum discrepancy rather than a question of whether or not the temperature generally increases in the chromosphere. The CO lines could be formed deeper in the atmosphere than in steady-state calculations due to their observed temporal variations of ±200 K caused by wave motions, and due to the property that the CO number density quickly decreases as T increases but is slow to increase again as T decreases, as shown by Asensio Ramos et al. (2003) (see also Avrett et al. 1996 and more recently by Wedemeyer-Böhm & Steffen 2007), thus causing a systematic decrease in opacity and a deeper formation depth. Second, the minimum temperature in internetwork regions could be as low as 3800 K, accounting for the CO observations near the limb, and still be consistent with the other observations noted above provided that the geometrical thickness of the low-temperature region is no more than about 200 km. The low temperatures within such a small height range would not greatly contribute to the three other spectral regions but would significantly affect CO absorption. An alternative model is given by Fontenla et al. (2007) with the temperature minimum located higher in the atmosphere.

This concludes our comments on the temperature minimum issue, and we now return to the main discussion of previous modeling work.

New models of the transition region were calculated by Fontenla et al. (1990, 1991, 1993, 2002) eliminating the ad hoc plateau in the VAL models. The parameters at the top of the VAL semiempirical chromospheric models were used as the lower boundary conditions for model transition regions determined theoretically from a balance between (1) the inward transport of energy from the corona by thermal conduction and particle diffusion and (2) the net radiative losses. The introduction of particle diffusion solved the problem that thermal conduction alone cannot transport sufficient energy down to the Lyα emitting region to account for the observed Lyα emission. The downward flow of ions into the neutral region (as a counterpart to the upward flow of neutrals into the ionized region) carries ionization energy that is released by recombination and emitted by the resonance lines of hydrogen, helium, and other elements.

These models of the transition region for the quiet Sun used modified versions of the VAL chromospheres, with the updated temperature-minimum and photopheric values described above. Fontenla et al. (1993) listed the atmospheric parameters at all depths for the new versions of models A, C, and F and for a bright plage model P based on the chromospheric plage model of Lemaire et al. (1981). Fontenla et al. (1999) showed plots of improved versions of models A, C, F, and P, along with models E, H, and S for the average network, an average plage, and an average sunspot umbra, respectively. Fontenla et al. (2002) gave results for hydrogen and helium mass flows with diffusion.

Fontenla et al. (2006, Table 3 for model C) used new observations in the visible and infrared to improve the photospheric portions of these component models and provided a new sunspot penumbra model. Tables are given for the atmospheric parameters at photospheric heights for model C, defined as having the same intensity as the median in a histogram of a Ca II K image of a quiet area of the Sun, and for models E, F, H, P, R, and S, corresponding to quiet-Sun network, active network, plage, faculae, sunspot penumbra, and sunspot umbra, respectively. The chromospheric portions of these component models, included in their plots, were based in part on VAL and other previous chromospheric models.

Thus, new models have been determined for the transition regions and photospheres, but the chromosphere in between for model C has not been redetermined in these previous papers. As noted above, problems remain in interpreting the temperature-minimum region. The present paper uses new EUV observations of the average quiet Sun to construct a new version of the chromosphere and transition region of model C. While this new chromospheric model should be considered as a replacement of the VAL average chromosphere, there are clearly further improvements to be made. Hence we designate this 2007 version as model C7.

Fuhrmeister et al. (2006) used VAL model C and the PHOENIX general-purpose atmosphere code of Hauschildt et al. (1999) to calculate the solar hydrogen spectrum. They discuss the influence of background lines on the ionization equilibrium of hydrogen. We comment on their results later in this paper and discuss several other model calculations involving the EUV carbon and oxygen lines considered here.

4. ATOMIC DATA

4.1. *Hydrogen*

We use a model hydrogen atom with 15 bound energy levels and calculate in detail the 15 bound-free continua and 105 lines, ignoring fine structure. Wavelengths, Einstein A-coefficients, line-broadening coefficients, and photoionization cross sections are from standard sources and are not listed here.

To obtain the rate of collisional ionization from level 1, we use the cross sections for electron impact ionization measured by Shah et al. (1987) over the energy range 14.6–3998.1 eV. For the cross section variation in the energy range between the threshold at 13.6 eV and 14.6 eV, we use equation (5) of Scholz & Walters (1991) from Rau (1971). We have compared our results with those obtained with the collisional ionization rates of Arnaud & Rothenflug (1985) for level 1, as used by Ferguson & Ferland (1997) in their hydrogen simulations, and find only minor differences.

For levels 2–15 we use the collisional ionization rates from Johnson (1972). We have also compared our results with those using (1) the rates based on the Coulomb-Born cross sections calculated by Clark et al. (1991) and (2) the rates of Vriens & Smeets (1980) also used by Ferguson & Ferland, and again we find only minor differences in the calculated profiles.

For the collisional excitation rates, we use the calculated collision strengths given by Przybilla & Butler (2004a) for transitions $n \rightarrow n'$ with $n' \leq 7$. For all higher transitions, we use the values given by Johnson (1972).

We have repeated the hydrogen non-LTE calculations using the following alternative set of collisional excitation rates: for the $1 \rightarrow 2$ rate, we use the results from Scholz et al. (1990) for $n \rightarrow n'$ with $n' \leq 5$ the values from Aggarwal et al. (1991) and the remaining ones from Johnson (1972). (See Chang et al. 1991 for a comparison of various rates, including those of Giovanardi et al. 1987 and Giovanardi & Palla (1989.) While many of the rates in this set are not close to those of Przybilla & Butler, the spectra calculated in the two cases do not differ substantially.

In addition to these rates for collisions with electrons, various studies, e.g., Fabbian et al. (2006) have indicated that it is important to include the rates for collisions with hydrogen atoms in regions of the atmosphere where hydrogen is essentially neutral and the atomic hydrogen number density is 3–4 orders of magnitude larger than the electron number density. We use the results calculated for Rydberg atoms given by Kaulakys (1985, 1986) to obtain these additional bound-free rates for hydrogen level 2 and higher and for the bound-bound rates for hydrogen transitions with lower level 2 and higher. The Kaulakys results appear to be more reliable than (1) the earlier ones of Drawin (1968, 1969) and (2) those of Steenbock & Holweger (1984), which were based on Drawin. Baumüller & Gehren (1996) in their study of line formation of neutral aluminum in the Sun found that the Kaulakys rates gave better agreement with observations than those of Drawin. See also Mauas et al. (2002). Caccin et al. (1993) in their study of the formation of Na I and K I lines in sunspot umbrae reached a similar conclusion.

We do no include hydrogen collisions for transitions involving level 1 of hydrogen, since the required excitation and ionization energies from the ground state far exceed the energies available from collisions with other hydrogen atoms. In the case of our solar model C7, we find that as long as transitions involving hydrogen level 1 are excluded, the hydrogen-hydrogen collisions do not greatly affect the solutions.

The Kaulakys rates apply to hydrogen-atom collisions as well as to hydrogen-hydrogen collisions, but only for hydrogen-like Rydberg atomic levels and only for moderate excitation and ionization energies. We use the equations given by Kaulakys for the collisional excitation or ionization of any atom or ion from levels having ionization energies no larger than that for level 2 of hydrogen. Thus for C I and O I, we use the added Kaulakys rates only for levels 7–19 and 8–20, respectively, and we find that our solar model C7 calculations are largely unaffectd by these high-level hydrogen-atom collisions.

4.2. *Charge Transfer and Dielectronic Recombination*

In our ionization equilibrium calculations for the atoms and ions of carbon, oxygen, and other elements, we include the rates for charge transfer with hydrogen, from Kingdon & Ferland (1996) and with helium from Arnaud & Rothenflug (1985).

Also in these calculations we include the dielectronic recombination rates from Badnell et al. (2003) using their fitting parameters.[2] The paper of Badnell et al. includes the dependence on electron density, but the on-line tables we use do not. Our results may change when density-dependent rates are available and are included.

4.3. *Photoionization Cross Sections*

Verner et al. (1996) give analytic fits to available cross sections for photoionization from the ground level of various atoms and ions. We use these results except where otherwise noted in subsequent sections. For levels 2 and higher, we use the hydrogenic approximation except where noted.

4.4. *Abundances*

We adopt the solar elemental abundances listed in Table 2. The electron number density as a function of height in the atmosphere is determined from charge neutrality, taking into account the calculated non-LTE ionization equibrium of H, He, C, N, O, Na, Mg, Al, S, Ca, and Fe and assuming LTE ionization for the remaining elements listed. A recent study of the solar oxygen abundance by Socas-Navarro & Norton (2007) concludes that the log abundance of oxygen lies between 8.63 and 8.93. The value 8.66 in Table 2 is in this range.

4.5. *Carbon and Oxygen Models*

Our atomic models for C I–IV and O I–VI have been chosen to include all the energy levels corresponding to the significant line transitions that appear in the SUMER and HRTS wavelength ranges. Particularly for C I and O I (see Tables 4 and 13 below), we must include a large number of energy levels and line transitions in our non-LTE calculations.

4.6. *Line Strengths*

For C I–IV and for O I–VI, we obtain Einstein *A* coefficients for all individual radiative transitions from the *gf* values in the line lists of R. L. Kurucz, given at http://kurucz.harvard.edu.

TABLE 2

List of Abundances

No.	Element	Ratio	Log	Reference
1	H	1.000E+00	12.00	
2	He	1.000E−01	11.00	
3	Li	1.122E−11	1.05	3
4	Be	2.399E−11	1.38	3
5	B	5.012E−10	2.70	1
6	C	2.455E−04	8.39	4
7	N	7.079E−05	7.85	5
8	O	4.571E−04	8.66	2
9	F	3.631E−08	4.56	1
10	Ne	6.918E−05	7.84	3
11	Na	1.479E−06	6.17	3
12	Mg	3.388E−05	7.53	3
13	Al	2.344E−06	6.37	3
14	Si	3.236E−05	7.51	3
15	P	2.291E−07	5.36	3
16	S	1.380E−05	7.14	3
17	Cl	3.162E−07	5.50	1
18	Ar	1.514E−06	6.18	3
19	K	1.202E−07	5.08	3
20	Ca	2.042E−06	6.31	3
21	Sc	1.122E−09	3.05	3
22	Ti	7.943E−08	4.90	3
23	V	1.000E−08	4.00	1
24	Cr	4.365E−07	5.64	3
25	Mn	2.455E−07	5.39	1
26	Fe	2.818E−05	7.45	3
27	Co	8.318E−08	4.92	1
28	Ni	1.698E−06	6.23	3
29	Cu	1.622E−08	4.21	1
30	Zn	3.981E−08	4.60	1
31	Ga	7.586E−10	2.88	1
32	Ge	3.802E−09	3.58	3
37	Rb	3.981E−10	2.60	1
38	Sr	8.318E−10	2.92	3
39	Y	1.622E−10	2.21	3
40	Zr	3.890E−10	2.59	3
56	Ba	1.479E−10	2.17	3

References.— (1) Grevesse & Sauval 2000; (2) Asplund et al. 2004; (3) Asplund et al. 2005a; (4) Asplund et al. 2005b; (5) Asplund 2005.

4.7. C I *Energy Levels and Wavelengths*

The energy levels for our C I atomic model are shown in Figure 4 and are listed in Table 3. We group the 128 individual C I energy levels from Moore (1993, pp. 24-27) into 19 reference levels. In Table 3 the number of individual levels in each reference level is given in parentheses when only the first and last individual levels are given. Reference level 8, e.g., consists of 10 individual levels that we center at 70,744 cm^{-1}. The individual levels within each reference level are close together in energy and are assumed to be collisionally coupled and in equilibrium with each other, so that we solve the statistical equilibrium equations for 19 C I levels, and the C II continuum, with 171 transitions, rather than solving the equations for all 128 levels with 8192 transitions. Such grouping of energy levels not only simplifies the calculations but is a good approximation for levels so close together that line transitions are blended together. The transitions and individual wavelengths are listed in Table 4.

Of our 171 transitions, 86 are considered radiative, i.e., have nonnegligible *A* or *gf* values, and 29 of these 86 transitions appear in the SUMER and HRTS wavelength ranges. These 29 transitions

---

[2] University of Strathclyde, Department of Physics, Fits for Total Dielectric Recombination Rate Coefficients, http://amdpp.phys.strath.ac.uk/tamoc/DR.

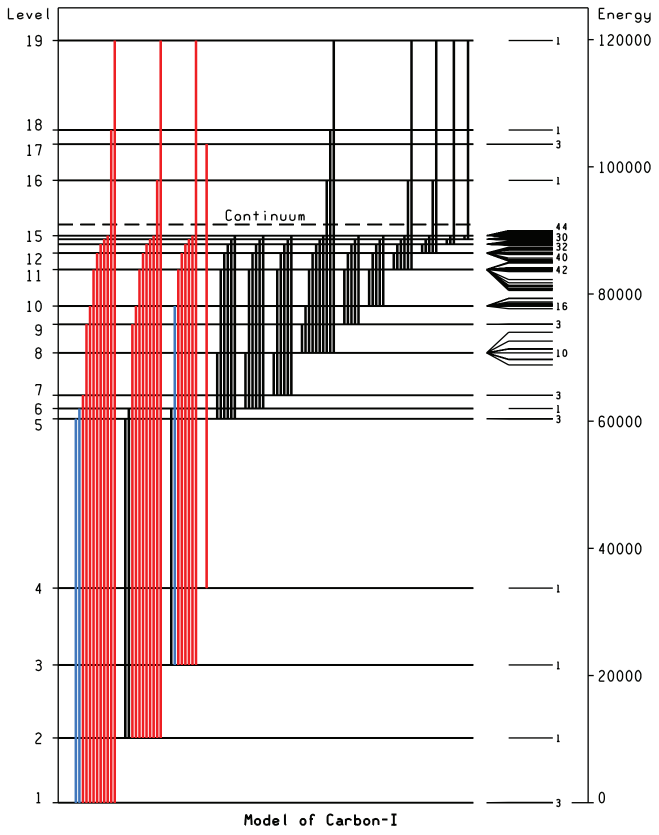

Fig. 4.—Energy levels for C I. The 19 reference levels are numbered on the left, and the energy scale in cm^{-1} is shown on the right. Individual levels are plotted on the near right, with the number of levels in each reference level indicated. SUMER transitions are shown in red and HRTS transitions in blue.

TABLE 3
C I Energy Levels

Level	Energy (cm^{-1})	Level	Energy (cm^{-1})
1............................	0	11(42).........................	81105
	16		. . .
	43		84985
2............................	10193	12(40).........................	85170
3............................	21648		. . .
4............................	33735		87113
5............................	60333	13(32).........................	87218
	60353		. . .
	60393		88198
6............................	61982	14(30).........................	88260
7............................	64087		. . .
	64090		88874
	64091	15(44).........................	88914
8(10).....................	68856		. . .
	. . .		89448
	72611	C II.............................	90917
9............................	75254	16...............................	97878
	75255	17...............................	103542
	75256		103563
10(16)...................	78105		103578
	. . .	18...............................	105799
	80835	19...............................	119878

TABLE 4
C I Line Wavelengths

Transition	Wavelengths (nm)
19/1	83.42, 83.43, 83.45 (a)
19/2	91.17 (b)
18/1	94.52, 94.53, 94.56
19/3	101.80 (c)
15/1	111.72, 111.74, 111.75, 111.76, 111.77, 111.78, 111.79, 111.81, 111.82, 111.84, 111.85, 111.87, 112.15, 112.15, 112.16, 112.17, 112.18, 112.20, 112.21, 112.22, 112.23, 112.24, 112.25, 112.26, 112.27, 112.28, 112.30, 112.30, 112.31
14/1	112.81, 112.82, 112.83, 112.84, 112.85, 112.86, 112.87, 112.88, 112.89, 112.90, 112.91, 112.92, 112.93, 112.94, 112.95, 112.96, 112.98, 112.99, 113.00, 113.02, 113.05
13/1	113.84, 113.86, 113.87, 113.89, 113.91, 113.93, 113.94, 113.95, 113.97, 113.98, 113.99, 114.00, 114.01, 114.02, 114.03, 114.04, 114.06, 114.07, 114.13, 114.17
16/2	114.04
12/1	115.58, 115.60, 115.62, 115.64, 115.66, 115.68, 115.72, 115.73, 115.74, 115.78, 115.79, 115.80, 115.81, 115.83, 115.84, 115.85, 115.87, 115.89, 115.90, 115.91, 116.05, 116.09
11/1............................	118.88, 118.90, 118.91, 118.93, 118.95, 118.96, 119.00, 119.03, 119.06, 119.22, 119.25, 119.28, 119.30, 119.32, 119.33, 119.34, 119.37, 119.40, 119.41, 119.42, 119.43, 119.44, 119.45, 119.46, 119.83
15/2	126.05, 126.06, 126.07, 126.08, 126.17, 126.18, 126.20, 126.62, 126.63, 126.64, 126.65, 126.66, 126.75, 126.76, 126.81
10/1	126.07, 126.09, 126.10, 126.11, 126.14, 126.16, 127.01, 127.08, 127.41, 127.65, 127.67, 127.72, 127.73, 127.75, 127.77, 127.86, 127.91, 127.92, 127.95, 127.99, 128.01, 128.03, 128.04, 128.06, 128.08, 128.76, 128.81
14/2	127.46, 127.48, 127.50, 127.52, 127.53, 127.61, 127.62, 127.63, 127.70
13/2	128.78, 128.80, 128.84, 128.87, 128.89, 128.90, 128.96, 128.99, 129.00, 129.01, 129.13
12/2	131.02, 131.06, 131.14, 131.19, 131.22, 131.29, 131.34, 131.35, 131.59
9/1	132.88, 132.91, 132.91, 132.91, 132.96
11/2............................	135.28, 135.30, 135.43, 135.58, 135.71, 135.77, 135.79, 135.82, 135.93, 135.94, 135.95, 136.42
17/4	143.16, 143.21, 143.25
10/2	145.90, 146.33, 146.74, 146.79, 146.81, 146.84, 147.01, 147.04, 147.22, 148.18
15/3	147.32, 147.35, 147.48, 148.10, 148.11, 148.15, 148.27, 148.29
14/3	149.26, 149.27, 149.33, 149.45, 149.48
13/3	151.07, 151.10, 151.19, 151.31, 151.35
9/2	153.70 (d)
12/3	154.25, 154.22, 154.40, 154.52, 154.60
7/1	156.03, 156.07, 156.13, 156.14
11/3............................	160.08, 160.30, 160.70, 160.84, 161.02
6/1	161.34, 161.38, 161.45
5/1	165.63, 165.69, 165.70, 165.74, 165.79, 165.81
10/3	173.40, 175.18, 176.39, 176.54, 177.09

Note.—(a): Obscured by blended O II and O III lines. (b): Obscured by the hydrogen Lyman continuum. (c): Obscured by Fe III lines. (d): Obscured by Si I lines.

TABLE 5

C i Collisional Excitation Rates

	2	3	4	5	6	7	8	9	10	11	12	13	14	15	16	17	18	19
1	PA	PA	R	R	R	R	R	R	R	S	S	S	S	S	R	VR	R	R
2		PA	R	R	R	R	R	R	R	S	S	S	S	S	R	VR	R	R
3			R	R	R	R	R	R	R	S	S	S	S	S	R	VR	R	S
4				R	VR	R	R	R	R	VR	VR	VR	VR	VR	R	VR	R	R
5					VR	VR	S	VR	VR	S	S	S	S	S	VR	VR	VR	VR
6						VR	S	VR	VR	S	S	S	S	S	VR	VR	VR	VR
7							S	R	F	S	S	S	S	S	R	VR	R	R
8								S	VR	S	S	S	S	S	S	VR	S	S
9									F	S	S	S	S	S	R	VR	R	R
10										S	S	S	S	S	VR	VR	VR	VR
11											S	S	S	S	S	VR	VR	S
12												S	S	S	S	VR	VR	S
13													S	S	VR	VR	VR	S
14														S	VR	VR	VR	S
15															VR	VR	VR	VR
16																VR	R	R
17																	VR	VR
18																		R

Note.—PA: Pequignot & Aldrovandi; R: Reid, F: Fon; S: Seaton; VR: van Regemorter.

are listed in Table 4 along with the wavelengths of the individual lines within each transition.

While we assume that the individual close-lying lines in each transition are collisionally coupled, we preserve all the individual line wavelengths, so that the absorption profile for the transition is a weighted sum of individual profiles displaced in wavelength. This (1) allows us to treat overlapping lines together as line blends rather than as separate lines that interact with each other (a more complex task) and (2) avoids the problem of the artificially large line-center opacity that would result when the lines of a multiplet are all assumed to have the same central wavelength. This approach in which levels with similar excitation energies and properties are grouped together has been used earlier by Anderson (1989), Anderson & Athay (1989a, 1989b), Hauschildt et al. (1997), Hillier & Miller (1998), and Fabbian et al. (2006).

Some of the individual lines in the 10/1 transition overlap with lines of the weaker transitions 15/2, 14/2, and 13/2. For simplicity we have not taken account of the blending of these overlapping transitions, and in our graphs these appear as separate, unblended lines. However, we include more important line blending, as described in § 8.

4.8. C i *Collisional Excitation*

For transitions 2/1, 3/1, and 3/2 we use the effective collision strengths given by Pequignot & Aldrovandi (1976). In Table 5 we use the designation PA for these three transitions.

The website http://www-amdis.iaea.org/GENIE provides a link to the NIFS AMDIS Database of measured collisional excitation cross sections. These include many cross sections calculated by Dunseath et al. (1993) and by Fon et al. (1994) (see the Abington JET citations there).

Dunseath et al. (1997) give effective collision strengths for many transitions of C i, but for temperatures no smaller than 25,000 K. We need values at much smaller temperatures and have found that some of the collision strengths do not vary monotonically with temperature, so that in these cases the values at 25,000 K and above cannot be reliably extrapolated to lower temperatures.

R. H. G. Reid (2007, private communication) has extended the effective collision strengths for the Dunseath et al. (1997) transitions to lower temperatures, using the methods in the 1997 Dunseath et al. paper and has included collision strengths for the 1993 Dunseath et al. list of transitions. We use the Reid collision strengths for the transitions labeled R in Table 5 and the Fon et al. results for the 10/7 and 10/9 transitions that are not included in the Dunseath or Reid lists.

For the remaining radiative transitions, we determine collision rates by the Seaton (1962) impact parameter method for electron excitation of optically allowed neutral-atom transitions. These rates are labeled S in Table 5. Rates for the remaining forbidden (or negligible A-value) transitions are obtained using the van Regemorter (1962) formula for allowed neutral-atom transitions, with the oscillator strength f in this formula set equal to 0.1. These rates are labeled VR in Table 5.

4.9. C i–iv *Collisional Ionization*

Suno & Kato (2006) review the available experimental and theoretical data on electron-impact ionization of carbon atoms and ions and give parametric fits to the recommended level-1 collisional ionization cross sections for C i–vi. For C i–iv we integrate their cross sections to obtain the collisional ionization rates from level 1 in each case. For the higher levels we use the parametric fits to calculated Coulomb-Born cross sections given by Clark et al. (1991). We obtain collisional ionization rates versus temperature from the cross sections by integrating over a maxwellian electron velocity distribution.

For reference we compare the level-1 collisional ionization rates of Suno & Kato with those of Voronov (1997), Clark et al. (1991), and Arnaud & Rothenflug (1985). The rate coefficient $CI(T)$ is defined such that the number of ionizations per second and per atom in level 1 is $CI(T)n_e \exp(-h\nu/kT)$, where n_e is the electron number density and ν is the threshold frequency. The values of $CI(T)$ from the four sources for C i–iv at typical values of the temperature T in K for each ion are given in Table 6. Our results are based on the Suno & Kato values. Regardless of the differences shown in Table 6, we do not find substantial differences in the C i–iv profiles calculated using the rates from the other three sources.

The Suno & Kato parametric fit for the C i ionization cross section in their Table 7 gives negative values close to threshold, which we have replaced by zeros in the rate integrations.

TABLE 6

Comparison of Collisional Ionization Rates

Reference	C I 6500 K	C II 10,000 K	C III 50,000 K	C IV 65,000 K
Suno & Kato (2006)	2.9E−08	1.2E−08	4.0E−09	1.1E−09
Voronov (1997)	7.1E−09	9.7E−09	4.0E−09	7.5E−10
Clark et al. (1991)	2.7E−08	7.9E−09	2.3E−09	1.8E−09
Arnaud & Rothenflug (1985)	2.8E−08	1.2E−08	4.0E−09	1.1E−09

4.10. C I *Photoionization Cross Sections*

We adopt the photoionization cross sections for the three lowest C I levels from Luo & Pradhan (1989) shown in Fig. 2 of Przybilla et al. (2001). The cross sections for levels 2 and 3 include resonances, which we assume to be independent of dielectronic recombination. We use hydrogenic approximations for levels 4–15 based on effective quantum numbers for each level, e.g., for level 10 the threshold cross section is 2.32×10^{-17} cm^2.

4.11. C II *Energy Levels and Wavelengths*

The energy levels for our C II atomic model are shown in Table 7. As before, the individual levels within each of the 15 reference levels are assumed to be in collisional equilibrium with each other.

Of the 105 transitions between these reference levels, 22 are treated as permitted radiative transitions, and the 15 transitions listed in Table 8 appear in the SUMER wavelength range. The wavelengths of each multiplet component are listed in each case.

4.12. C II *Collisional Excitation*

Wilson et al. (2005) give tables of calculated effective collision strengths for electron impact excitation of C II for values of log T(K) between 3.0 and 5.5. All 105 of our transitions are included, with the exception of the transitions between our levels 4 and 6 to level 8. These are nonradiative transitions for which we use the van Regemorter formula for ion transitions assuming $f = 0.1$ as the oscillator strength. Othewise, we adopt the Wilson et al. collision strengths.

TABLE 8

C II Line Wavelengths

Transition	Wavelengths (nm)
9/1	68.71, 68.73, 68.74
15/3	79.97, 79.99
12/2	80.64, 80.65, 80.66, 80.67, 80.68, 80.69
14/3	80.97, 80.98
6/1	85.81, 85.86
5/1	90.36, 90.40, 90.41, 90.45
15/4	94.60, 94.62
8/2	100.99, 101.01, 101.04
4/1	103.63, 103.70
13/3	106.33, 106.59, 106.61
15/5	109.19, 109.22, 109.24, 109.27
14/5	113.89. 113.93, 113.95
11/3	114.16, 114.17
10/3	132.39, 132.40, 132.60
3/1	133.45, 133.57

The CHIANTI database, http://wwwsolar.nrl.navy.mil/chianti.html (Dere et al. 1997; Landi et al. 2006), gives the effective collision strengths for 17 of the C II transitions we consider (2/1–8/1, 10/1, 13/1, 3/2–8/2, 10/2, and 13/2). We find that calculations of the C II lines using these CHIANTI collision rates in place of those from Wilson et al. give similar results.

TABLE 7

C II Energy Levels

Level	Energy (cm^{-1})	Level	Energy (cm^{-1})
1	0	10	150462
	63		150467
2	43003	11	162518
	43025		162525
	43054	12	166967
3	74930		166991
	74933		167036
4	96494	13	168730
5	110624		168748
	110666		168978
6	116538	C III	196659
7	131724	14	198425
	131736		198436
8	142027	15	199941
9	145549		199983
	145551		202180
			202205

Sigut (1996) and Nieva & Przybilla (2006) have carried out non-LTE studies of stellar C II spectra at visible wavelengths, using more elaborate models of the C II ion than the one considered here.

4.13. C III *Energy Levels and Wavelengths*

The energy levels for our C III atomic model, and the transitions and wavelengths of lines in the SUMER spectrum, are listed in Tables 9 and 10, respectively.

4.14. C III *Collisional Excitation*

We adopt the Suno & Kato rates for those 21 of our transitions they include, namely, 2/1–10/1, 4/2–7/2, 9/2, 10/2, 4/3–6/3, 5/4, 6/4, and 6/5, and use the van Regemorter formula for the remaining 57 transitions.

4.15. C IV *Energy Levels and Wavelengths*

We adopt the 8-level atomic model for C IV listed in Table 11. Only the pair of lines at 154.82 and 155.08 nm (transition 2/1) are in the SUMER wavelength range.

4.16. C IV *Collisional Excitation*

We use the Suno & Kato rates for the 8 transitions 2/1–5/1, 7/1, 3/2, 5/2, and 6/2 and van Regemorter for the remaining 18 transitions.

TABLE 9

C III Energy Levels

Level	Energy (cm^{-1})	Level	Energy (cm^{-1})
1	0	7	238213
2	52367	8	274170
	52391	9	258931
	52447	10	270011
3	102352		270012
4	137426		270015
	137454	11	310006
	137502	12	322404
5	145876	13	343258
6	182520	C IV	386241

TABLE 10

C iii Line Wavelengths

Transition	Wavelengths (nm)
8/3	69.05
3/1	97.70
4/2	117.49, 117.52, 117.56, 117.57, 117.60, 117.64
6/3	124.74

4.17. O i *Energy Levels and Wavelengths*

We use an O i atomic model with 40 individual energy levels grouped into the 20 reference levels shown in Figure 5 and listed in Table 12. In Figure 5, SUMER transitions are shown in red and the HRTS transition in blue. Table 13 lists the wavelengths in nm of the individual O i lines that appear in the SUMER/HRTS spectrum. The first 13 levels represented in this table are the same as those in the atomic model used by Carlsson & Judge (1993) and by Koncewicz & Jordan (2007) in their detailed studies of the O i resonance lines.

4.18. O i *Collisional Excitation*

As indicated in Table 14, we adopt the values given by Zatsarinny & Tayal (2003) for the transitions they include and those of Bhatia et al. (1982) for the additional transitions that they list. Otherwise, we use the Seaton and van Regemorter formulae for radiative and nonradiative transitions, respectively.

4.19. O i *Collisional Ionization*

Following Przybilla et al. (2000) we adopt the experimental cross sections from Thompson et al. (1995) for collisional ionization of the O i ground state and the cross sections from Chung et al. (1993) for collisional ionization from $n = 3$ triplet levels. For the remaining levels we use collisional ionization rates from Seaton (1962).

4.20. O ii *Energy Levels and Wavelengths*

We list in Table 15 the energy levels in our O ii atomic model and in Table 16 the wavelengths of the O ii lines that appear in the SUMER spectrum.

TABLE 11

C iv Energy Levels

Level	Energy (cm^{-1})
1	0
2	64484
	64592
3	302849
4	320050
	320082
5	324880
	324890
6	401348
7	408311
	408324
8	410336
	410340
C v	520178

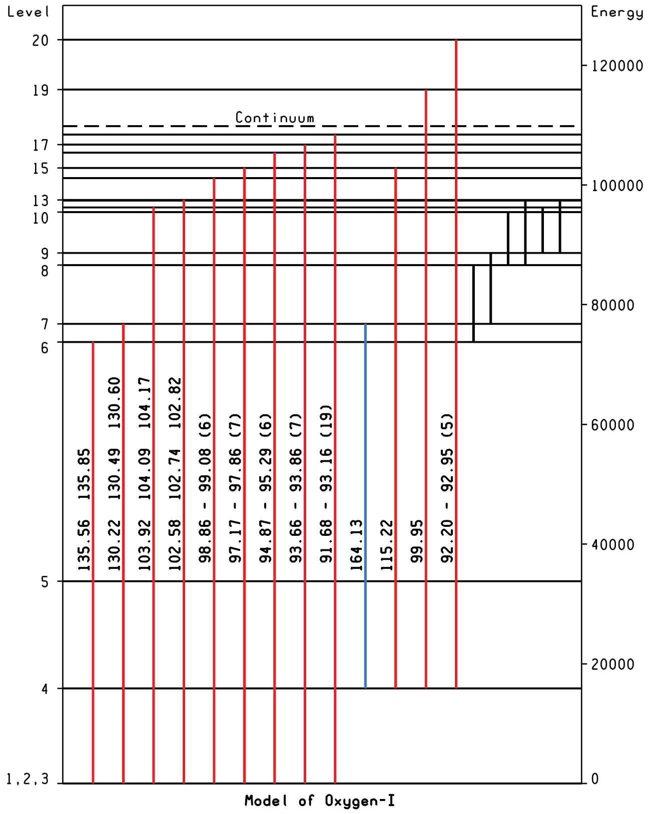

Fig. 5.—Energy levels and line transitions for O i. SUMER and HRTS transitions are in red and blue, respectively.

TABLE 12

O i Energy Levels

Level	Energy (cm^{-1})	Level	Energy (cm^{-1})
1	0	16	105165
2	158		105409
3	227	17	106628
4	15868		106751
5	33793		106766
6	73768	18	107497
7	76795		107583
8	86627		108056
9	88631		108114
10	95477		108436
11	96225		108477
12	97421		108736
13	97488		108927
14	101135		109073
	101148	O ii	109837
	101155	19	115918
15	102412	20	124219
	102662		124224
	102866		124253
	102908		124319
			124327

TABLE 13

O I LINE WAVELENGTHS

Transition	Wavelengths (nm)
18/1	91.68, 91.80, 91.97, 92.19, 92.22, 92.50, 92.54, 92.95, 93.03 (H Ly10 at 91.94, H Ly9 at 92.10)
18/2	91.94, 92.10, 92.32, 92.63, 92.68, 93.09, 93.16 (H Ly8 at 92.32, Ly7 at 92.62, Ly6 at 93.07)
20/4	92.20, 92.21, 92.26, 92.29
18/3	92.38, 92.69, 93.15
17/1	93.66, 93.68, 93.78 (H Ly5 at 93.78)
17/2	93.80, 93.81, 93.92
17/3	93.86
16/1	94.87, 95.09 (H Ly4 at 94.97)
16/2	95.01, 95.23
16/3	95.07, 95.29
15/1	97.17, 97.21, 97.64 (H Ly3 at 97.25)
15/2	97.32, 97.80
15/3	97.39, 97.86
14/1	98.86, 98.87, 98.88
14/2	99.01, 99.02
14/3	99.08
19/4	99.95
13/1	102.58 (H Ly2 at 102.57)
13/2	102.74
13/3	102.82
11/1............................	103.92
11/2............................	104.09
11/3............................	104.17
15/4	115.22
7/1	130.22
7/2	130.49+Si II
7/3	130.60
6/1	135.56+C I
6/2	135.85
7/4	164.13

4.21. O II *Collisional Excitation*

We use CHIANTI to obtain the collision rates for the 14 O II transitions 2/1–5/1, 9/1, 3/2–5/2, 9/2, 4/3, 5/3, 9/3, 5/3, and 9/4 and the van Regemorter formula for the remaining 41 transitions.

4.22. O II–VI *Collisional Ionization*

For O II–VI level-1 collisional ionization we use the rates of Arnaud & Rothenflug. Other values are given by Voronov, but we find that calculations based on the Voronov rates do not give substantialy different results. We use the cross sections of Clark et al. for all higher levels.

4.23. O II *Photoionization Cross Sections*

Aguilar et al. (2003) give measured absolute photoionization cross sections for O II levels 1, 2, and 3 (see Table 15). The level-1 cross section from the Verner et al. analytic fit is 8.56 Mbarn at the 35.3 nm threshold and rises to a maximum of 9.3 Mbarn at 33.0 nm, whereas the measured values are roughly 10.5 Mbarn near threshold, rising to 12 mB at 33.7 nm. Consequently, we

TABLE 14

O I COLLISIONAL EXCITATION RATES

	2	3	4	5	6	7	8	9	10	11	12	13	14	15	16	17	18	19	20
1	BK	BK	ZT	ZT	ZT	ZT	ZT	ZT	ZT	ZT	ZT	ZT	ZT	ZT	S	S	S	ZT	ZT
	2	BK	ZT	ZT	ZT	ZT	ZT	ZT	ZT	ZT	ZT	ZT	ZT	S	S	S	S	VR	VR
		3	ZT	ZT	ZT	ZT	ZT	ZT	ZT	ZT	ZT	ZT	ZT	ZT	S	S	S	VR	VR
			4	ZT	ZT	ZT	ZT	ZT	ZT	ZT	ZT	ZT	ZT	ZT	VR	VR	VR	ZT	ZT
				5	VR	VR	VR	ZT	VR	VR	VR	ZT	ZT	VR	VR	VR	VR	ZT	ZT
					6	BK	BK	BK	BK	BK	BK	BK	VR	VR	VR	VR	VR	VR	VR
						7	BK	BK	BK	BK	BK	BK	VR	VR	VR	VR	VR	VR	VR
							8	BK	BK	BK	BK	BK	VR	VR	VR	VR	VR	VR	VR
								9	BK	BK	BK	BK	VR	VR	VR	VR	VR	VR	VR
									10	BK	BK	BK	VR	VR	VR	VR	VR	VR	VR
										11	BK	BK	VR	VR	VR	VR	VR	VR	VR
											12	BK	VR	VR	VR	VR	VR	VR	VR
												13	VR	VR	VR	VR	VR	VR	VR

NOTE.—BK: Bhatia et al.; ZT: Zatsarinny & Tayal; S: Seaton; VR: van Regemorter.

TABLE 15

O II Energy Levels

Level	Energy (cm^{-1})	Level	Energy (cm^{-1})
1	0	7	188889
2	26811		189069
	26831	8	206972
3	40468		206973
	40470	9	212594
4	119837		212762
	120000	10	232463
	120083		232536
5	165988		232602
	165997	11	255105
6	185235		255142
	185341		255163
	185499	O III	283271

multiply the Verner et al. distribution for level 1 by the factor 1.3 to approximate the measured results. For levels 2 and 3 (with thresholds at 39.0 and 41.2 nm), the measured cross sections have average values of roughly 5.0 and 1.5 Mbarn, which we use as the threshold values, and assume the same relative variations for shorter wavelengths as given by Verner et al. for level 1.

4.24. O III *Energy Levels and Wavelengths*

We list in Table 17 the energy levels in our O III atomic model and in Table 18 the wavelengths of the lines in the SUMER range.

4.25. O III *Collisional Excitation*

We obtain O III collision rates from the calculated collision strengths given by Aggarwal & Keenan (1999). They provide data for all 91 transitions in our 14-level atom except the 7/3 transition, for which we use the van Regemorter formula.

The CHIANTI database gives collision strengths for 40 of the transitions (those with lower levels 1, 2, and 3, and transitions 5/4, 7/6, 8/6, and 8/7). Figure 25 of §18.3 shows the O III 4/1 profiles calculated using these CHIANTI collision strengths versus the profiles we obtain using the Aggarwal & Keenan values.

4.26. O IV *Energy Levels and Wavelenghts*

We list in Table 19 the energy levels in our O IV atomic model and in Table 20 the line wavelengths in the SUMER range.

4.27. O IV *Collisional Excitation*

The CHIANTI database give collision strengths for the 22 O IV transitions 2/1, 3/1–10/1, 13/1–16/1, 3/2, 4/2, 5/2, 8/2, 9/2, 10/2, 13/2, 14/2, and 16/2. We use these values along with the van Regemorter formula for the remaining transitions.

TABLE 16

O II Line Wavelengths

Transition	Wavelengths (nm)
7/3	67.29, 67.30, 67.38
5/2	71.85, 71.86
5/3	79.66, 79.67
4/1	83.28, 83.33, 83.45 (O III lines at 83.29, 83.37, 83.51, 83.53; C I lines at 83.42, 83.43, 83.45)

TABLE 17

O III Energy Levels

Level	Energy (cm^{-1})	Level	Energy (cm^{-1})
1	0	8	210462
	113	9	267259
	307		267377
2	20273		267634
3	43186	10	273081
4	120025	11	324736
	120053	12	327299
	120058		327278
5	142381		327352
	142382	13	329470
	142394		329584
6	187054		329645
7	197088	14	331821
		O IV	443085

4.28. O V *Energy Levels and Wavelengths*

We list in Table 21 the energy levels in our O V atomic model and in Table 22 the line wavelengths in the SUMER range.

4.29. O V *Collisional Excitation*

We use CHIANTI to obtain the collision rates for the 11 transitions with lower levels 1 and 2 and the van Regemorter formula for the remaining transitions.

4.30. O VI *Energy Levels and Wavelengths*

Table 23 lists the energy levels in our O VI atomic model. The lines in the SUMER range consist of the 103.19 and 103.76 components of the 2/1 transition.

4.31. O VI *Collisional Excitation*

We adopt the calculated O VI electron impact collision strengths given by Tayal (2003) for all the transitions among these 5 levels except for 5/4 (which is not given by Tayal), and we use the van Regemorter formula for this transition.

The CHIANTI website gives collision strengths for transitions 2/1, 3/1, 3/2, 4/1, 4/2, 5/1, and 5/2. We find that these rates (with those of van Regemorter for 4/3, 5/3, and 5/4) give intensities for the 103.19 and 103.76 nm lines about 20% higher than those calculated with the Tayal rates.

5. MOLECULAR OPACITIES

The molecules CH and OH can make a significant contribution to the continuous opacity at wavelengths near 160 nm where the emerging radiation is formed in the temperature-minimum region. We use the CH and OH absorption cross sections given by Kurucz et al. (1987). In the low-temperature range where molecules are important, we need to determine the number densities of

TABLE 18

O III Line Wavelengths

Transition	Wavelengths (nm)
5/1	70.23, 70.28, 70.29, 70.39
4/1	83.29, 83.37, 83.51, 83.53 (O II lines at 83.28, 83.33, 83.45 C I lines at 83.42, 83.43, 83.45)

TABLE 19

O IV ENERGY LEVELS

Level	Energy (cm^{-1})	Level	Energy (cm^{-1})
1	0	11	513187
	386		513198
2	71440	12	539368
	71570	13	547326
	71756		547355
3	126936	14	549792
	126950		549855
4	164366	15	552030
5	180481		552032
	180724	16	554464
6	357614	17	574369
7	419534	18	575202
	419551		575375
8	467229	19	584541
	467345		584761
9	482666	20	590069
	482922	O V	624382
10	492891		

TABLE 21

O V ENERGY LEVELS

Level	Energy (cm^{-1})
1	0
2	81943
	82079
	82385
3	158798
4	213463
	213618
	213887
5	231721
6	287910
7	580825
O VI	918657

carbon, oxygen, and hydrogen in molecular form as well as in atomic form. We take into account CO and H_2 as well as CH and OH and solve the seven equations listed below for the seven unknowns $n_{\rm CH}$, $n_{\rm OH}$, $n_{\rm CO}$, $n_{\rm H_2}$, $n_{\rm C1}$, $n_{\rm O1}$, and $n_{\rm H1}$, where the last three number densities are those corresponding to the ground states of atomic carbon, oxygen, and hydrogen, respectively. The temperature T, the total hydrogen density $n_{\rm H}$, and the abundances $A_{\rm C}$ and $A_{\rm O}$ of carbon and oxygen relative to hydrogen are assumed to be given. Also assumed given, from our ionization balance solutions, are the ratios $n_{\rm C^*}/n_{\rm C1}$, $n_{\rm O^*}/n_{\rm O1}$, and $n_{\rm H^*}/n_{\rm H1}$, where the numerators represent the number densities in higher atomic levels and higher ionization stages. The molecular equilibrium functions ϵ for CH, OH, CO, and H_2 as functions of temperature in the equations below are taken from http://kurucz.harvard.edu/programs/atlas12/molecules.dat:

$$n_{\rm CH} = n_{\rm C1} n_{\rm H1} \epsilon_{\rm CH}(T), \tag{1}$$

$$n_{\rm OH} = n_{\rm O1} n_{\rm H1} \epsilon_{\rm OH}(T), \tag{2}$$

$$n_{\rm CO} = n_{\rm C1} n_{\rm O1} \epsilon_{\rm CO}(T), \tag{3}$$

$$n_{\rm H_2} = (n_{\rm H1})^2 \epsilon_{\rm H}(T), \tag{4}$$

$$n_{\rm C1}(1 + n_{\rm C^*}/n_{\rm C1}) + n_{\rm CH} + n_{\rm CO} = A_{\rm C} n_{\rm H}, \tag{5}$$

$$n_{\rm O1}(1 + n_{\rm O^*}/n_{\rm O1}) + n_{\rm OH} + n_{\rm CO} = A_{\rm O} n_{\rm H}, \tag{6}$$

$$n_{\rm H1}(1 + n_{\rm H^*}/n_{\rm H1}) + 2n_{\rm H_2} = n_{\rm H}. \tag{7}$$

We include the H^- ion as a source of opacity, solving the non-LTE equations as described by VAL (see also Lites & Mihalas 1984), but the H^- number density is too small to affect the equations given above.

6. PHOTOIONIZATION CONTINUA

The continuum intensity distribution in the SUMER wavelength range is primarily determined by the non-LTE results for H, C I, Si I, and S I, with lesser contributions from Fe I, Al I, Mg I, CH, and OH. The threshold photoionization wavelengths, in nm, for the lowest energy levels (1 up to 8) of these neutral atoms, along with He I, Ca I, and Na I, are listed in Table 24, along with the threshold cross section values, in 10^{-18} cm^2, used in the present calculations.

7. GENERAL EFFECTS OF LINES IN PHOTOIONIZATION INTEGRALS

The photoionization rate out of a given atomic level, at a given height in the atmosphere, is given by the integral, over frequency ν, starting at threshold,

$$R = 4\pi \int \frac{1}{h\nu} a_\nu J_\nu d\nu, \tag{8}$$

where a_ν is the photoionization cross section for the given level and J_ν is the mean intensity of radiation at that height. The mean intensity depends on the absorption and emission of line and continuum radiation versus both wavelength and height. The correct approach is to carry out explicit non-LTE calculations for all of the lines that significantly affect the photoionization rates. This is a major task that is beyond the scope of the present paper, but one that has been partially carried out by Fuhrmeister et al. (2006). As stated earlier, we carry out non-LTE calculations for the continua and principal lines of H, H^-, He I–II, C I–IV, N I–IV, O I–VI, Ne I–VIII, Na I–II, Mg I–II, Al I–II, Si I–IV, S I–IV, Ca I–II, and Fe I and LTE calculations for CO, CH, OH, and H_2, but the spectrum contains a great many additional lines that have to be taken into account in

TABLE 20

O IV LINE WAVELENGTHS

Transition	Wavelengths (nm)
3/1	78.77, 79.01, 79.02
2/1	139.72, 139.98, 140.12, 140,48, 140.74

TABLE 22

O V LINE WAVELENGTHS

Transition	Wavelengths (nm)
4/2	75.87, 75.94, 76.02, 76.04, 76.11, 76.20
6/3	77.45
2/1	121.83+H(2/1)
5/3	137.13

TABLE 23

O VI ENERGY LEVELS

Level	Energy (cm^{-1})
1	0
2	96375
	96908
3	640040
4	666113
	666270
5	674626
	674677
O VII	1114010

TABLE 24

ATOMIC THRESHOLD WAVELENGTHS

Atom	Level	Threshold (nm)	Cross Section (10^{-18} cm^2)
He	1	50.4	7.39
O	1	91.04	1.23
H	1	91.18	7.91
O	2	91.18	1.23
O	3	91.23	1.23
O	4	106.42	4.64
C	1	110.04	17.2
S	1	120.50	1.6
C	2	123.94	10.5
S	2	134.55	20.99 (a)
C	3	144.32	14.3
Si	1	151.99	67
Fe	1	157.60	1
Mg	1	162.15	2.55
S	3	162.92	22.58 (b)
Si	2	168.08	34.6
C	4	174.81	13.1
Fe	2	176.90	5
Fe	3	194.20	3
Si	3	198.40	26.3
Ca	1	202.82	1
Al	1	207.50	60.9
Fe	4	217.80	3
Fe	5	221.80	0.44
Fe	6	226.70	1.7
Fe	7	226.90	1.61
Fe	8	233.50	1.02
Na	1	241.26	0.13
Mg	2	251.51	20.2
He	2	259.40	5.48

NOTE.—(a): The value at 112.11; apart from resonance structure the cross section is 0 between 134.55 and 112.11. (b): The value at 116.41; apart from resonance structure the cross section is 0 between 162.92 and 116.41.

order to properly determine J_ν and hence the photoionization rates.

Extensive line lists are available from the Kurucz and NIST Web sites. We use such lists to add lines that are not included in our explicit non-LTE calculations and to determine the absorption coefficient versus wavelength and height due to these additional lines. However, we cannot use LTE in the higher layers of the atmosphere to determine the line emissivities, since this would cause the strong lines to be in emission, contrary to observations. These lines are treated with a scattering approximation in the higher layers, as discussed below.

We show in Figure 6, courtesy of R. L. Kurucz, the calculated spectrum in the narrow wavelength interval 171.60–171.65 nm. The red curve shows the calculated intensity distribution relative to the continuum (the 1.0 level at the top). These intensities are much smaller than the values calculated with continuum opacities alone. Identifications are given for 44 lines that absorb at least 1% of the continuum: 4 lines of Cr II, 3 of Fe II, 2 of Fe I, 1 of Si I, 1 of Mn II, 19 of CO, 12 of SiO, and 2 of H_2. Many other weaker lines contribute to the calculated intensity distribution shown in the figure. The intensity distribution in this plot does not include Kurucz's further set of lines with predicted wavelengths that are only statistically reliable.

The spectrum in Figure 6 is largely determined by the Fe II line at 171.6321 nm and by 6 strong CO lines from the *A–X* electronic band. These CO lines are subject to non-LTE effects, unlike the LTE CO vibration–rotation lines seen in the infrared. In the quiet Sun the CO lines in Figure 6 are absorption lines, but they are seen in emission in sunspots, as discussed by Jordan et al. (1979). Ayres et al. (1981) found them to be fluorescent lines in the spectrum of Arcturus, excited by chromospheric emissions of O I, C I, and H.

As discussed below, we have introduced scattering at chromospheric heights to reduce the central intensities of strong lines that would be in emission if calculated in LTE. The spectrum in Figure 6 computed in LTE without scattering in the chromosphere shows the Fe II line at 171.6321 nm in emission (with the central intensity 1.26 times the continuum) contrary to observations. See Kurucz (1991, Fig. 7). This example indicates that errors in the photoionization rates would occur if (1) such lines were not included or (2) LTE were assumed, which would cause strong line emission that is not observed.

A line that is strong enough to have its line-center optical depth close to unity in the chromosphere where the temperature increases with height will appear in emission if the line source function S also increases with height. Typically, S is smaller than the Planck function B in the low-density chromosphere, thus producing a weaker emission line than would be the case in LTE with $S = B$ or producing an absorption line in some cases. (The central portions of the strong Ca II resonance lines are in emission with central absorption, since the line source function first increases and then decreases in the chromosphere.) In the chromosphere, the values of S are typically between B, which increases with temperature, and the mean intensity J, which is constant at small optical depths, with S increasingly decoupled from B as height increases.

This relationship can be expressed as $S = LB + (1 - L)J$, where L is a function of depth which approaches unity in the high-density LTE photosphere and becomes very small in the low-density chromosphere where photons are primarily scattered rather than absorbed. The function L is essentially the probability that, following the excitation of an atom by a photon, a collisional de-excitation will take place rather than the re-emission of a photon; L expresses the relationship between S, B, and J and is a different function for each line, as can be determined from a non-LTE solution, but L in most cases varies smoothly between essentially zero in the midchromosphere and unity in the upper photosphere.

As an expedient, to use in the absence of individual non-LTE solutions, we have adopted a wavelength-independent function L versus height to use for all lines for which we do not carry out non-LTE calculations. We interpolate from the table: $L = 1$, 0.9, 0.7, 0.5, 0.1, 0.01, 0.001, 0.0001, and 0 corresponding to the heights 400, 500, 600, 700, 800, 900, 1000, 1100, and 1200 km, respectively. We have determined these values empirically from

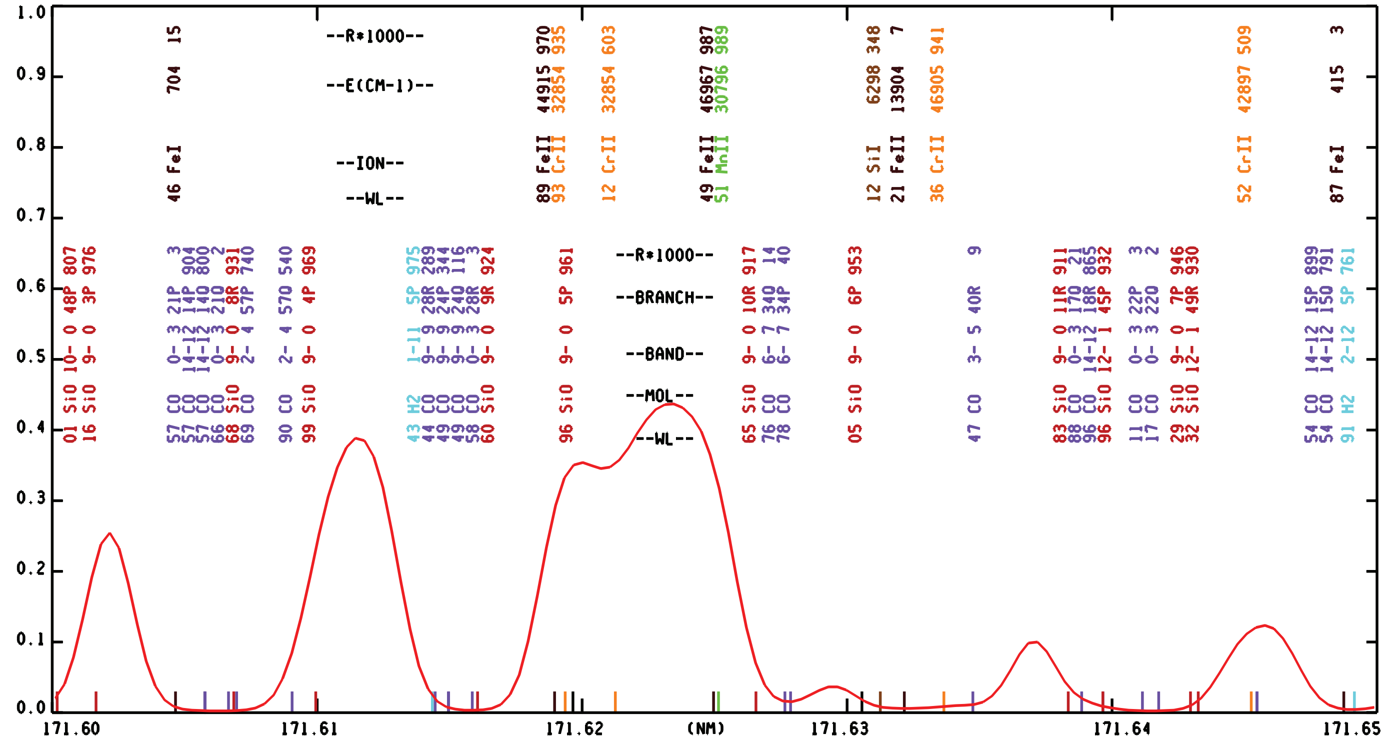

Fig. 6.—Calculated intensity distribution in the 171.60–171.65 nm range relative to the continuum (i.e., the 1.0 level at the top), as an illustration of the many lines in the spectrum that must be taken into account in calculating photoionization rates. The two digits marked -WL- are those added to the wavelengths given at the bottom of the figure. R*1000 indicates the individual central line intensities on the scale 0–1000. Courtesy of R. L. Kurucz.

an analysis of the detailed spectrum calculated from a complete set of line opacities from R. L. Kurucz (private communication) in the wavelength range 123.9–207.5 nm, with the opacity evaluated at 257,829 wavelengths. This complete set includes Kurucz's further set of lines, noted above, having known strengths but uncertain wavelengths. In successive trial calculations we have reduced L at a given height as needed to reduce the emission from any calculated line formed at that height in excess of observed emission or increased L at heights where calculated absorption lines were deeper than observed. While this simple function does not provide detailed agreement with observations, it succeeds in removing from the calculated spectrum excessive emission and excessive absorption that are inconsistent with observations and in allowing a reasonable J_ν to be calculated for use in photoionization integrals. This function of height is model dependent and applies only to the model C7 given in this paper.

Fuhrmeister et al. solved the non-LTE equations for a large number of lines that affect photoionization in solar models. They included many other lines as well, without solving detailed non-LTE equations, and for these used a source-function equation similar to ours, namely, $S = \epsilon B + (1 - \epsilon)J$, where B is the Planck function and J is the monochromatic mean intensity, but with $\epsilon = 10^{-4}$, constant with depth. See Short & Hauschildt (2005) for a more general study of non-LTE line blanketing in solar-type stars.

To simplify the evaluation of the photoionization integrals, we have reduced the 257,829 Kurucz wavelengths in the range 123.9–207.5 nm to 1290 values by choosing five representative wavelengths from each 1000. These five wavelengths and corresponding opacities are determined by (1) ordering each set of 1000 opacity/wavelength pairs in opacity sequence, (2) choosing the 100th, 300th, 500th, 700th, and 900th of the opacities in this sequence, and (3) assigning these pairs to a uniformly spaced wavelength scale, with the wavelengths put in the same order as the original values. This is done at every depth in the calculation for the approximate line opacities in the 123.9–207.5 nm range. Between 207.5 and 605 nm we use values determined from an earlier set of Kurucz line opacities discussed in the context of solar-flare modeling by Avrett et al. (1986).

Figure 7 shows (in green) the full-disk spectrum observed by Hall & Anderson (1991) between 210 and 310 nm at 0.01 nm

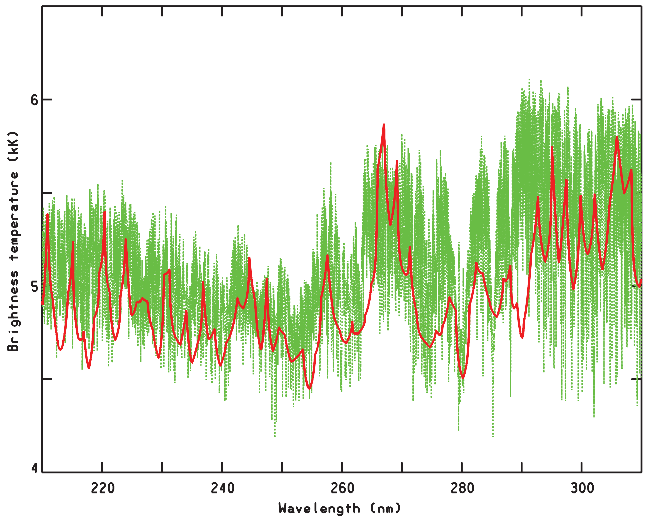

Fig. 7.—Approximate emergent flux spectrum calculated from model C7 at wavelengths between 210 and 310 nm (*shown in red*) compared with the flux spectrum observed by Hall & Anderson (1991) shown as dashed lines in green. While the observed spectrum is the surface distribution, we obtain the calculated distribution at every depth in the atmosphere for use in the photoionization rate integrations.

resolution and our corresponding computed approximate spectrum (in red) that is intended to give similar result when integrated over wavelength to obtain photoionization rates, but the computed results seem lower than observed.

8. EXPLICIT BACKGROUND LINES

The results in this paper are based on detailed non-LTE calculations for roughly a thousand lines, but for practical reasons only a fraction of these are currently included in the general background, i.e., along with the continuum sources and the approximate line distribution discussed above. Non-LTE computed lines need to be included in the general background for two reasons: (1) to take the place of the line approximations discussed above and (2) to include the effects of important line blends. For example, we need to account for the blending of the O I line at 102.576 nm with the hydrogen Lyβ line at 102.572 nm. This combined line is also affected by the He II line components around 102.43 nm. The Lyα line at 121.567 nm is slightly affected by the He II line components between 121.51 and 121.52 nm. In general, the hydrogen 2/1, 3/1, 4/1, . . . lines are blended with those of He II 4/2, 6/2, 8/2, . . ., while the He II 5/2, 7/2, 9/2, . . . lines are distinct. There are many O I lines blended with the hydrogen 4/1, 5/1, and 6/1 lines. The O III line components between 30.34 and 30.38 nm are strongly influenced by the He II resonance line at 30.379 nm.

Table 25, for example, shows the overlap in wavelength of the multiplet components of the C I 19/1, O II 4/1, and O III 4/1 transitions and the overlap between the O III 13/1 transition and the He II 2/1 resonance line, giving Bowen fluorescence. We show later, in panel 14 of Figure 23, our calculated blend of these multiplet lines near 83 nm compared with the SUMER observations. We account for the non-LTE interactions among these three transitions, but the C I line is much weaker than the O II and O III lines and is influenced by but does not influence these oxygen lines. Similarly, the 30.3 nm O III multiplet is dominated by the strong He II resonance line but has no reverse effect.

We include in the general background the significant lines of H, He I, He II, O I, O II, and O III. Thus, our calculation of the hydrogen Lyβ line includes the non-LTE results obtained for the O I lines at 102.576, 102.743, and 102.815 nm from a previous O I calculation and a calculation of these O I lines uses results from a previous hydrogen calculation. We treat the interactions between the O II and O III lines in Table 25, and their influence on the C I line, and the influence of He II on O III, in the same way. This iterative procedure gives good results without difficulty.

TABLE 25

C I, O II, O III, AND He II WAVELENGTHS

C I	O II	O III	He II
	83.28		
		83.29	
	83.33		
		83.37	
83.42			
83.43			
83.45	83.45		
		83.51	
		83.53	
		30.342	
		30.346	
		30.352	
		30.363	
		30.370	
			30.379
		30.380	

9. INCIDENT CORONAL RADIATION

Throughout the spectrum we use our individually calculated lines in place of approximate lines wherever possible. The approximate line spectrum discussed in § 7 does not extend to wavelengths below 123.9 nm. Figure 1 shows that there are many lines in the spectrum shortward of the Lyα line at 121.567 nm, most of which we have not included. Many of these are coronal lines that have little effect on the chromospheric spectrum. However, coronal lines shortward of 50.4 nm significantly affect He I, and those shortward of 22.8 nm affect He II. The helium lines, in turn, influence the hydrogen spectrum and lines of various ions, including O III as mentioned above. In our He I calculation we explictly include the He II lines at 30.38, 25.63, 24.30, 23.73, and 23.43 nm and the He II continuum shortward of 22.8 nm, and we include the He I lines at 58.43, 53.70, 52.23, and 51.56 nm and the He I continuum shortward of 50.4 nm. But the spectrum exhibits a large number of additional strong emission lines from highly ionized species that have to be taken into account in order to properly treat the ionization of helium and other elements. This problem has been addressed by VAL, Wahlstrom & Carlsson (1994), and Mauas et al. (2005). These three papers use coronal line data from different sources that need to be reconciled. The Mauas et al. paper includes a very useful examination of the wavelength ranges of incident coronal radiation that are most effective in leading to agreement between calculated and observed absorption in the He I line at 1083 nm. They find that the 1083 nm absorption is sensitive to the magnitude of the strong line emission shortward of 50.4 nm, but that the details of the spectral distribution are less important. A detailed study of He I and He II is beyond the scope of the present paper, but our non-LTE solutions for He I and He II need to be approximately correct since these lines and continua have some influence on hydrogen, oxygen, and other elements. Therefore we use the following very simple prescription for incident coronal radiation: in the wavelength range 15–38 nm we add to the calculated mean intensity of radiation the constant 7×10^{-12} ergs cm^{-2} s^{-1} Hz^{-1} multiplied by the depth attenuation $E_2(\tau_\nu)$, where τ_ν is the monochromatic continuum optical depth and E_2 is the second exponential integral. We find that this specification of the incident coronal radiation gives calculated results that are roughly consistent with the observed absorption in the He I 1083 nm line and the observed emission in the He I resonance lines. Clearly a better approach would be to include detailed calculations of all the strong lines in this wavelength range.

10. THE $V_{\rm tp}(h)$ DISTRIBUTION

As stated in § 1, the calculated spectrum depends on distributions with height of the temperature T and the velocity distributions $V_{\rm nt}$ for line broadening and $V_{\rm tp}$ as a turbulent pressure contribution, which we set equal to $V_{\rm nt}$. Given this common velocity distribution $V(h)$ (from Table 1 and the calculated $n_{\rm H}$ vs. h), and given the many rates and cross sections, we adjust $T(h)$ by trial and error to get optimum agreement between the calculated spectrum and the observed one.

It is reasonable to expect that the nonthermal velocities give rise to a turbulent pressure that should be added to the gas pressure. The effect of a turbulent pressure contribution was first discussed by McCrea (1929). Thus, we let $V_{\rm tp}(h) = V_{\rm nt}(h)$ and add the term $(1/2)\rho V_{\rm tp}^2$ to the gas pressure. The increased total pressure causes the atmosphere to be more distended and to move the transition region to a greater height. The lower chromosphere is hardly affected since $V_{\rm tp}$ is only of order 1 km s^{-1} in this region.

A good measure of the height of the top of the chromosphere, and the onset of the transition region, is the height observed at the solar limb of the local maximum in the He I line intensity at 1083.3 nm (and in the D_3 line at 587.5 nm), i.e., the height of the bright ring seen around the solar disk at 1083.3 nm (and to a lesser extent at 587.5 nm), except in coronal-hole regions. Back-radiation from coronal lines causes enhanced He I ionization at the top of the chromosphere. Recombination then populates the $2s\,^3S$, $2p\,^3P^o$ levels and higher ones, causing He I line absorption of the infrared continuum on the disk and emission above the limb. The coronal emission penetrates only a short distance into the chromosphere, so that the height of the local maximum just above the limb indicates the height of the top of the chromosphere. The $V_{\rm tp}(h)$ distribution we adopt for model C7 places the top of the chromosphere at about 2140 km. This height is roughly consistent with limb observations of the D_3 and 1083.3 nm lines (e.g., White 1963; Zirin 1975; Schmidt et al. 1994; see also Avrett et al. 1994b). At greater heights above the limb our calculated emission decreases abruptly compared with a gradual decrease in the observed emission, because portions of the transition region extend much higher. Our height scale is measured from a zero reference value in the photosphere where τ_{500}, the continuum optical depth at 500 nm, is unity. The position of the white-light limb of the Sun on this scale is about 350 km above $\tau_{500} = 1$ (see Foukal 2004, p. 150; Athay 1976; and articles by Athay in Sturrock et al. 1986).

Our choice of $V_{\rm tp}(h) = V_{\rm nt}(h)$ succeeds in extending the upper chromosphere to be consistent with limb observations. Setting $V_{\rm tp} = 0$ for the same T versus h causes the total pressure at $T =$ 7950 K, $h = 2142$ km to decrease from 0.107 to 0.060 dyn cm^{-2}, so that the transition region would have to be moved inward to obtain the higher pressure as before. The extension of the atmosphere mainly takes place in the upper chromosphere where $V_{\rm tp}$ is much larger than unity. We note that Fontenla et al. (2007) propose an alternative way to extend the atmosphere by means of forces that are effective lower in the chromosphere.

11. METHOD OF SOLUTION

Given $T(h)$ and $V(h)$, we solve the hydrostatic equilibrium equation to obtain $n_{\rm H}(h)$ and determine the electron number density $n_{\rm e}(h)$ from the sum of the electrons contributed by the single and multiple ionizations of all the atoms and ions we consider.

The statistical equilibrium and radiative transfer equations for the atoms and ions are solved in detail to obtain both (1) the mean intensity of radiation J_ν at all depths in the atmosphere and all line and continuum wavelengths and (2) the level populations of all atoms and ions. Many of these equations are strongly coupled together (particularly the statistical equilibrium and transfer equations for a strong line transition) and usually must be solved simultaneously. Most others are not strongly coupled and can be solved iteratively. We use simultaneous solutions for strong transitions, as described in the Appendix, and not “accelerated lambda iteration” or ALI methods (see Hubeny 2003). As shown by Avrett (2007b), there are cases in which the ALI method essentially does not converge.

Most line transitions can be treated with the simple approximation of complete frequency redistribution (CRD) in which the line frequencies of absorbed and subsequently reemitted photons are uncorrelated. This assumes some perturbations of the atom in its excited state between photon absorption and reemission. The line source function, or ratio of emission and absorption coeffients, is then frequency-independent throughout the line.

On the other hand, strong lines such as the hydrogen Lyα and Lyβ resonance transition do not have such simple properties. A photon absorbed in the wing of the line is reemitted at a nearby frequency rather than from line center or from an uncorrelated frequency. In the Appendix we summarize (1) the procedure we use in the general case of partial frequency redistribution (PRD), with CRD as a special case, and (2) the procedure we use to solve the coupled equations of statistical equilibrium and radiative transfer.

12. THE HYDROGEN LYMAN CONTINUUM AND ITS SLOPE

As indicated in Figure 1, the observed brightness temperature at 70 nm exceeds that at 91.17 nm, i.e., the Lyman continuum brightness temperature increases with decreasing wavelength. This is seen in the *SkyLab* observations plotted in Figure 1 as well as in the SUMER observations. This result is counterintuitive in that the Lyman continuum opacity decreases with decreasing wavelength (roughly as λ^3) so that unit optical depth at 70 nm occurs deeper in the atmosphere than that at 91.17 nm. If the Lyman continuum source function increases monotonically with height, corresponding to an outward increase in temperature, then the brightness temperature at 70 nm would be expected to be smaller than at 91.17 nm, not larger. An analysis of the depth dependence of the contribution functions at various wavelengths indicates that for the smaller wavelengths, there are not only contributions from the deeper chromospheric layers but also contributions from the high-temperature layers of the transition region, which have less influence on the intensity at the head of the Lyman continuum. The Lyman continuum source function S_ν is approximately the Planck function B_ν divided by the wavelength-independent departure coefficient b_1, which measures the hydrogen level-1 departures from LTE. The increase of B_ν and hence S_ν between temperatures 8000 and 30,000 K is 80 times larger at 70 nm than at 91.17 nm. In order to match the observations, the temperature must increase abruptly to high values just above region where the head of the Lyman continuum is formed. We have shown the contribution functions for 91.17, 80, and 70 nm in Figure 2.

There is a second reason for this abrupt increase in the model temperature distribution. The Lyman continuum opacity is proportional to the neutral hydrogen number density, and this opacity increases with decreasing temperature in this region where hydrogen is partially ionized. A temperature decrease at a given height can thus shift unit optical depth out to a greater height where the temperature is higher. As a result, a decrease in temperature in this region may decrease the calculated intensity very little, if at all. If the calculated intensity at the head of the Lyman continuum is larger than observed as a result of being formed in the low transition region, the most effective way to obtain a smaller intensity is to move the transition region to a greater height, thus decreasing the transition-region pressure and decreasing the Lyman continuum optical depths at the top of the chromosphere.

The slowly varying temperature in the upper chromosphere and the abrupt temperature rise in the transition region can be generally understood as a consequence of the cooling due to hydrogen (mainly Lyα and Hα) and other lines (mainly Fe II, Mg II, and Ca II; see Anderson & Athay 1989a) in the temperature range where hydrogen is partially ionized. This net radiative cooling inhibits a more rapid rise in temperature in the middle and upper chromosphere in response to chromospheric heating, the nature of which is still not understood. But this cooling has little effect at much higher temperatures where hydrogen is almost fully ionized. The jump in temperature will occur at a density just low enough that the cooling due to Lyα and other sources ceases to dominate over the combination of local heating and energy transport from above (see Athay 1976). Thus, we regard the transition region and the chromosphere to be related phenomena that generally occur between neutral- and ionized-hydrogen domains, provided that there is sufficient heating to cause hydrogen to become ionized. We have no basis here to distinguish between acoustic and magnetic heating, as discussed, e.g., by Judge & Carpenter (1998).

The proper way to model the upper chromosphere and lower transition region, in our idealized one-dimensional, time-independent treatment, is to determine the temperature distribution from an energy-balance solution. From our non-LTE solutions we can determine the net outward radiative flow of energy from the hydrogen lines and continua and from other atoms and ions. We also calculate the downward flow of energy through the transition region by thermal conduction and particle diffusion from the work of Fontenla et al. (but in these studies, mechanical heating was not included). We could postulate some distribution of nonradiative (mechanical) heating in this region and determine the temperature variation with height for which the net radiative cooling balances the nonradiative heating and energy flow through the transition region. Such calculations are feasible but are beyond the scope of the present paper. Calculations of the chromospheric cooling rates have been reported by VAL, Avrett (1985), Anderson (1989), and Anderson & Athay (1989a, 1989b).

For simplicity we have empirically adjusted the temperature distribution up to the temperature value $T = 7950$ K at $h = 2142$ km to obtain reasonable agreement between the calculated and observed chromospheric spectrum. For higher temperatures we have calculated an energy-balance solution using the boundary conditions corresponding to the above T and V, thus balancing the radiative losses with the energy flow from above (but without including local mechanical heating in the transition region). It is not difficult to match the intensity at the head of the Lyman continuum in this way, since this intensity increases as this value of h decreases. However, given our attempt to match the overall SUMER spectrum, we have not been able to obtain a good fit the observed slope of the Lyman continuum, as shown in Figure 1. The Fontenla et al. models, which used VAL chromospheres, did not show this disagreement with the slope of the Lyman continuum, but we have not determined why the problem occurs in some cases but not others.

We note that Fuhrmeister et al. found that hydrogen ionization and hence the intensity in the Lyman continuum is sensitive to the treatment of non-LTE lines in the Lyman, Balmer, and Paschen continua, but they were also unable to match the observed slope of the Lyman continuum (see their Fig. 2).

13. MODEL C7

In Figure 2 we showed the temperature distribution for model C7, extending from the photosphere into the transition region, and the contribution functions dI/dh for the continuum wavelengths 70–160 nm and 0.2 mm to 5 cm. We show later (in Figs. 13, 18, and 22) the contributions to the central intensities of various hydrogen, carbon, and oxygen lines. These contribution functions indicate the heights at which various line centers are formed. We adjust the temperature at these heights to bring the calculated line intensities into agreement with observed values. Generally, if the computed intensity at one of these wavelengths is lower or higher than the observed intensity, then the temperature at the height of the maximum contribution is raised or lowered accordingly. An exception to this procedure occurs in attempts to match the intensities in the Lyman continuum since, as noted above, the optical depth in the Lyman continuum is very sensitive to temperature. Model C7 was constructed primarily from a match to the continuum intensities from 70–160 nm and to the hydrogen Lyα and Lyβ line intensities, and to maintain general agreement with the observed carbon and oxygen line intensities shown in Figures 19 and 23.

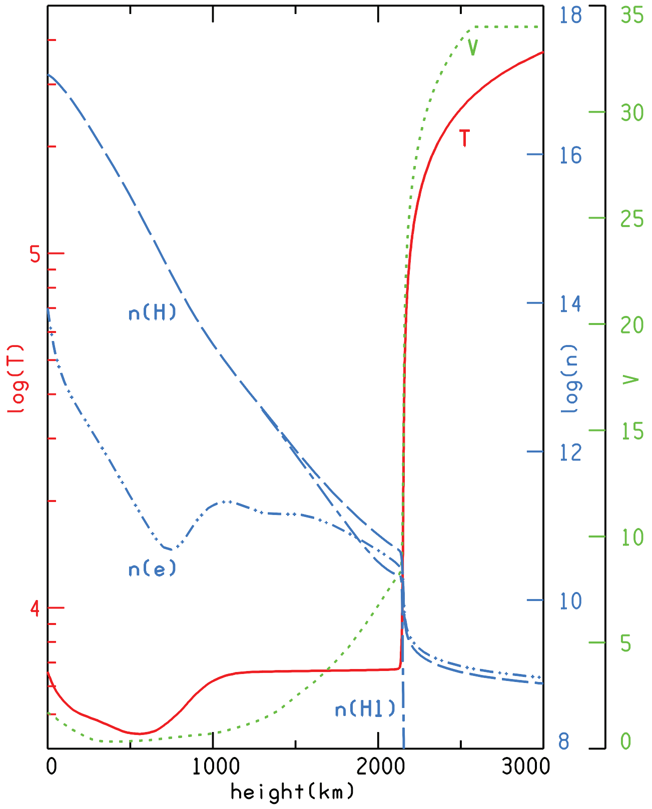

FIG. 8.—Model C7 variations with height of the temperature (in K), turbulent velocity (in km s^{-1}), total hydrogen density, neutral hydrogen density, and electron density (in cm^{-3}).

Figure 8 shows the model C7 temperature distribution $T(h)$, the broadening (and turbulent-pressure) velocity $V(h)$, and the calculated distributions of the total hydrogen density $n_{\rm H}$, the neutral hydrogen density $n_{\rm H\,I}$, and the electron density $n_{\rm e}$. These and other functions are shown in Table 26.

14. CONVOLUTION OF THE CALCULATED PROFILES

As indicated earlier, the Curdt et al. and Brekke quiet-Sun observations used in this paper correspond to averages over network and internetwork regions. Ideally, we should model such regions separately and compare with observations from the separate regions. However, an average model based on the average spectrum is of interest given the extensive spectral data available for the average quiet Sun, from 67 to 173 nm, whereas only fragmentary data have been published for separate network and internetwork regions.

Even though we have included nonthermal broadening, the lines calculated from our one-dimensional model are generally narrower than the observed lines in the SUMER and HRTS atlases. Also, some of the calculated multiplet lines have separate components while the corresponding observed ones are blended together, and many calculated lines have narrow central reversals that the observed lines do not exhibit, not because the observations lack good spectral resolution, but because they represent (1) a blend of intensities from different spatial regions, (2) various motions in these regions, and (3) instrumental broadening. In order to compare the calculated and observed profiles, we apply to our

TABLE 26

Atmospheric Parameters for Model C7

	h (km)	m (g cm^{-2})	T (K)	V (km s^{-1})	$p_{\rm g}$ (dyn cm^{-2})	$p_{\rm tot}$ (dyn cm^{-2})	$n_{\rm H}$ (cm^{-3})	$n_{\rm H1}$ (cm^{-3})	$n_{\rm e}$ (cm^{-3})
1	6.80844E+04	1.178E−06	1.586E+06	3.400E+01	3.142E−02	3.227E−02	6.233E+07	8.860E+00	7.491E+07
2	4.70093E+04	1.553E−06	1.410E+06	3.400E+01	4.131E−02	4.256E−02	9.217E+07	1.522E+01	1.108E+08
3	3.60795E+04	1.820E−06	1.294E+06	3.400E+01	4.827E−02	4.986E−02	1.174E+08	2.164E+01	1.411E+08
4	2.66766E+04	2.112E−06	1.170E+06	3.400E+01	5.583E−02	5.787E−02	1.502E+08	3.152E+01	1.805E+08
5	2.11331E+04	2.325E−06	1.080E+06	3.400E+01	6.127E−02	6.369E−02	1.786E+08	4.163E+01	2.147E+08
6	1.53920E+04	2.592E−06	9.637E+05	3.400E+01	6.801E−02	7.102E−02	2.221E+08	6.013E+01	2.669E+08
7	1.15962E+04	2.808E−06	8.650E+05	3.400E+01	7.333E−02	7.694E−02	2.667E+08	8.348E+01	3.206E+08
8	8.97424E+03	2.986E−06	7.783E+05	3.400E+01	7.756E−02	8.180E−02	3.135E+08	1.133E+02	3.768E+08
9	7.36082E+03	3.112E−06	7.117E+05	3.400E+01	8.044E−02	8.526E−02	3.556E+08	1.455E+02	4.274E+08
10	5.76283E+03	3.256E−06	6.293E+05	3.400E+01	8.355E−02	8.920E−02	4.177E+08	2.034E+02	5.021E+08
11	4.96864E+03	3.338E−06	5.774E+05	3.400E+01	8.516E−02	9.145E−02	4.641E+08	2.560E+02	5.578E+08
12	4.29586E+03	3.415E−06	5.243E+05	3.400E+01	8.653E−02	9.356E−02	5.193E+08	3.303E+02	6.242E+08
13	3.75271E+03	3.485E−06	4.716E+05	3.400E+01	8.757E−02	9.548E−02	5.842E+08	4.361E+02	7.022E+08
14	3.42499E+03	3.532E−06	4.329E+05	3.400E+01	8.810E−02	9.677E−02	6.403E+08	5.457E+02	7.695E+08
15	3.13379E+03	3.578E−06	3.920E+05	3.400E+01	8.842E−02	9.803E−02	7.096E+08	7.082E+02	8.529E+08
16	2.97076E+03	3.606E−06	3.650E+05	3.400E+01	8.847E−02	9.879E−02	7.625E+08	8.549E+02	9.165E+08
17	2.84440E+03	3.629E−06	3.413E+05	3.400E+01	8.840E−02	9.943E−02	8.149E+08	1.022E+03	9.794E+08
18	2.76149E+03	3.645E−06	3.240E+05	3.400E+01	8.827E−02	9.988E−02	8.571E+08	1.174E+03	1.030E+09
19	2.68810E+03	3.661E−06	3.073E+05	3.400E+01	8.808E−02	1.003E−01	9.018E+08	1.353E+03	1.084E+09
20	2.62832E+03	3.674E−06	2.925E+05	3.400E+01	8.785E−02	1.006E−01	9.451E+08	1.546E+03	1.136E+09
21	2.57823E+03	3.685E−06	2.790E+05	3.400E+01	8.758E−02	1.010E−01	9.876E+08	1.757E+03	1.187E+09
22	2.53547E+03	3.695E−06	2.667E+05	3.372E+01	8.748E−02	1.012E−01	1.032E+09	1.993E+03	1.240E+09
23	2.49556E+03	3.705E−06	2.544E+05	3.332E+01	8.744E−02	1.015E−01	1.082E+09	2.279E+03	1.300E+09
24	2.45790E+03	3.715E−06	2.419E+05	3.289E+01	8.737E−02	1.018E−01	1.137E+09	2.632E+03	1.366E+09
25	2.41866E+03	3.725E−06	2.278E+05	3.238E+01	8.726E−02	1.021E−01	1.205E+09	3.132E+03	1.448E+09
26	2.37819E+03	3.737E−06	2.120E+05	3.177E+01	8.710E−02	1.024E−01	1.293E+09	3.873E+03	1.554E+09
27	2.34610E+03	3.747E−06	1.981E+05	3.121E+01	8.692E−02	1.027E−01	1.380E+09	4.740E+03	1.659E+09
28	2.32578E+03	3.754E−06	1.886E+05	3.080E+01	8.677E−02	1.029E−01	1.447E+09	5.502E+03	1.739E+09
29	2.30855E+03	3.760E−06	1.801E+05	3.041E+01	8.662E−02	1.030E−01	1.513E+09	6.347E+03	1.819E+09
30	2.29437E+03	3.765E−06	1.726E+05	3.006E+01	8.647E−02	1.032E−01	1.576E+09	7.241E+03	1.894E+09
31	2.28238E+03	3.770E−06	1.660E+05	2.973E+01	8.633E−02	1.033E−01	1.637E+09	8.195E+03	1.966E+09
32	2.26969E+03	3.775E−06	1.586E+05	2.936E+01	8.615E−02	1.034E−01	1.710E+09	9.482E+03	2.054E+09
33	2.25943E+03	3.779E−06	1.523E+05	2.902E+01	8.599E−02	1.035E−01	1.778E+09	1.082E+04	2.135E+09
34	2.25164E+03	3.782E−06	1.472E+05	2.874E+01	8.586E−02	1.036E−01	1.836E+09	1.209E+04	2.205E+09
35	2.24332E+03	3.786E−06	1.416E+05	2.842E+01	8.569E−02	1.037E−01	1.905E+09	1.377E+04	2.288E+09
36	2.23529E+03	3.789E−06	1.358E+05	2.808E+01	8.552E−02	1.038E−01	1.982E+09	1.582E+04	2.379E+09
37	2.22774E+03	3.793E−06	1.302E+05	2.774E+01	8.531E−02	1.039E−01	2.064E+09	1.831E+04	2.477E+09
38	2.22004E+03	3.797E−06	1.240E+05	2.738E+01	8.506E−02	1.040E−01	2.160E+09	2.165E+04	2.592E+09
39	2.21374E+03	3.800E−06	1.187E+05	2.704E+01	8.483E−02	1.041E−01	2.251E+09	2.531E+04	2.700E+09
40	2.20766E+03	3.803E−06	1.132E+05	2.669E+01	8.457E−02	1.042E−01	2.353E+09	2.996E+04	2.821E+09
41	2.20192E+03	3.806E−06	1.078E+05	2.631E+01	8.430E−02	1.043E−01	2.465E+09	3.595E+04	2.953E+09
42	2.19652E+03	3.810E−06	1.023E+05	2.591E+01	8.401E−02	1.044E−01	2.589E+09	4.375E+04	3.099E+09
43	2.19146E+03	3.813E−06	9.686E+04	2.549E+01	8.370E−02	1.045E−01	2.727E+09	5.404E+04	3.259E+09
44	2.18608E+03	3.816E−06	9.064E+04	2.498E+01	8.332E−02	1.046E−01	2.904E+09	7.053E+04	3.463E+09
45	2.18244E+03	3.819E−06	8.612E+04	2.459E+01	8.303E−02	1.046E−01	3.049E+09	8.766E+04	3.628E+09
46	2.17874E+03	3.822E−06	8.122E+04	2.414E+01	8.269E−02	1.047E−01	3.225E+09	1.141E+05	3.827E+09
47	2.17528E+03	3.824E−06	7.633E+04	2.366E+01	8.234E−02	1.048E−01	3.422E+09	1.611E+05	4.049E+09
48	2.17232E+03	3.827E−06	7.181E+04	2.319E+01	8.200E−02	1.048E−01	3.628E+09	2.501E+05	4.280E+09
49	2.16999E+03	3.829E−06	6.800E+04	2.277E+01	8.170E−02	1.049E−01	3.822E+09	4.054E+05	4.497E+09
50	2.16769E+03	3.831E−06	6.395E+04	2.229E+01	8.137E−02	1.050E−01	4.054E+09	7.644E+05	4.757E+09
51	2.16603E+03	3.833E−06	6.079E+04	2.189E+01	8.112E−02	1.050E−01	4.255E+09	1.319E+06	4.984E+09
52	2.16456E+03	3.834E−06	5.779E+04	2.149E+01	8.088E−02	1.050E−01	4.468E+09	2.253E+06	5.222E+09
53	2.16329E+03	3.835E−06	5.502E+04	2.110E+01	8.065E−02	1.051E−01	4.684E+09	3.680E+06	5.464E+09
54	2.16229E+03	3.837E−06	5.269E+04	2.075E+01	8.046E−02	1.051E−01	4.885E+09	5.494E+06	5.687E+09
55	2.16126E+03	3.838E−06	5.014E+04	2.036E+01	8.025E−02	1.051E−01	5.127E+09	8.397E+06	5.955E+09
56	2.16063E+03	3.838E−06	4.849E+04	2.009E+01	8.012E−02	1.052E−01	5.297E+09	1.095E+07	6.142E+09
57	2.16001E+03	3.839E−06	4.680E+04	1.980E+01	7.999E−02	1.052E−01	5.484E+09	1.428E+07	6.348E+09
58	2.15942E+03	3.840E−06	4.514E+04	1.951E+01	7.986E−02	1.052E−01	5.683E+09	1.832E+07	6.565E+09
59	2.15884E+03	3.841E−06	4.340E+04	1.919E+01	7.974E−02	1.052E−01	5.908E+09	2.352E+07	6.809E+09
60	2.15821E+03	3.842E−06	4.145E+04	1.882E+01	7.960E−02	1.053E−01	6.185E+09	3.092E+07	7.107E+09
61	2.15757E+03	3.843E−06	3.940E+04	1.840E+01	7.948E−02	1.053E−01	6.508E+09	4.068E+07	7.454E+09
62	2.15682E+03	3.844E−06	3.687E+04	1.785E+01	7.935E−02	1.053E−01	6.958E+09	5.605E+07	7.933E+09
63	2.15616E+03	3.845E−06	3.458E+04	1.729E+01	7.931E−02	1.053E−01	7.433E+09	7.423E+07	8.434E+09
64	2.15550E+03	3.846E−06	3.226E+04	1.670E+01	7.927E−02	1.054E−01	7.985E+09	9.798E+07	9.013E+09
65	2.15473E+03	3.848E−06	2.950E+04	1.598E+01	7.922E−02	1.054E−01	8.757E+09	1.349E+08	9.815E+09

TABLE 26—*Continued*

	h (km)	m (g cm^{-2})	T (K)	V (km s^{-1})	p_g (dyn cm^{-2})	p_{tot} (dyn cm^{-2})	n_H (cm^{-3})	n_{H1} (cm^{-3})	n_e (cm^{-3})
66	2.15407E+03	3.849E−06	2.713E+04	1.533E+01	7.916E−02	1.055E−01	9.547E+09	1.763E+08	1.063E+10
67	2.15348E+03	3.850E−06	2.512E+04	1.478E+01	7.907E−02	1.055E−01	1.033E+10	2.210E+08	1.144E+10
68	2.15287E+03	3.852E−06	2.310E+04	1.422E+01	7.891E−02	1.055E−01	1.125E+10	2.769E+08	1.237E+10
69	2.15203E+03	3.854E−06	2.051E+04	1.346E+01	7.869E−02	1.056E−01	1.269E+10	3.809E+08	1.383E+10
70	2.15116E+03	3.857E−06	1.814E+04	1.272E+01	7.844E−02	1.057E−01	1.437E+10	5.412E+08	1.550E+10
71	2.15012E+03	3.861E−06	1.576E+04	1.192E+01	7.811E−02	1.058E−01	1.663E+10	8.787E+08	1.761E+10
72	2.14865E+03	3.867E−06	1.320E+04	1.098E+01	7.756E−02	1.060E−01	2.009E+10	1.749E+09	2.046E+10
73	2.14705E+03	3.876E−06	1.098E+04	1.027E+01	7.565E−02	1.062E−01	2.469E+10	4.413E+09	2.274E+10
74	2.14516E+03	3.888E−06	9.115E+03	9.422E+00	7.338E−02	1.065E−01	3.187E+10	1.165E+10	2.325E+10
75	2.14193E+03	3.915E−06	7.950E+03	8.868E+00	7.239E−02	1.073E−01	3.784E+10	1.693E+10	2.432E+10
76	2.13800E+03	3.951E−06	7.248E+03	8.535E+00	7.238E−02	1.083E−01	4.204E+10	1.954E+10	2.608E+10
77	2.13600E+03	3.971E−06	6.992E+03	8.401E+00	7.253E−02	1.088E−01	4.388E+10	2.066E+10	2.686E+10
78	2.13400E+03	3.992E−06	6.870E+03	8.328E+00	7.288E−02	1.094E−01	4.493E+10	2.118E+10	2.741E+10
79	2.13200E+03	4.014E−06	6.800E+03	8.279E+00	7.331E−02	1.100E−01	4.565E+10	2.147E+10	2.787E+10
80	2.13000E+03	4.035E−06	6.768E+03	8.247E+00	7.381E−02	1.106E−01	4.612E+10	2.157E+10	2.826E+10
81	2.12600E+03	4.079E−06	6.740E+03	8.199E+00	7.486E−02	1.117E−01	4.685E+10	2.167E+10	2.891E+10
82	2.12000E+03	4.145E−06	6.718E+03	8.134E+00	7.649E−02	1.136E−01	4.783E+10	2.176E+10	2.985E+10
83	2.11000E+03	4.259E−06	6.706E+03	8.033E+00	7.932E−02	1.167E−01	4.944E+10	2.204E+10	3.128E+10
84	2.09800E+03	4.401E−06	6.700E+03	7.901E+00	8.289E−02	1.206E−01	5.153E+10	2.258E+10	3.293E+10
85	2.08300E+03	4.587E−06	6.694E+03	7.729E+00	8.761E−02	1.257E−01	5.438E+10	2.351E+10	3.498E+10
86	2.05500E+03	4.963E−06	6.686E+03	7.403E+00	9.719E−02	1.360E−01	6.042E+10	2.583E+10	3.883E+10
87	2.02400E+03	5.430E−06	6.680E+03	7.031E+00	1.091E−01	1.488E−01	6.843E+10	2.916E+10	4.307E+10
88	1.98900E+03	6.034E−06	6.674E+03	6.617E+00	1.247E−01	1.653E−01	7.917E+10	3.447E+10	4.826E+10
89	1.94600E+03	6.910E−06	6.667E+03	6.118E+00	1.475E−01	1.893E−01	9.543E+10	4.371E+10	5.526E+10
90	1.89400E+03	8.221E−06	6.660E+03	5.542E+00	1.817E−01	2.253E−01	1.210E+11	6.005E+10	6.450E+10
91	1.82000E+03	1.074E−05	6.652E+03	4.776E+00	2.480E−01	2.942E−01	1.730E+11	9.843E+10	7.969E+10
92	1.72200E+03	1.589E−05	6.643E+03	3.939E+00	3.832E−01	4.353E−01	2.864E+11	1.916E+11	1.027E+11
93	1.61700E+03	2.546E−05	6.633E+03	3.165E+00	6.368E−01	6.975E−01	5.170E+11	4.012E+11	1.267E+11
94	1.52000E+03	4.136E−05	6.623E+03	2.576E+00	1.061E+00	1.133E+00	9.256E+11	7.956E+11	1.423E+11
95	1.39800E+03	8.131E−05	6.610E+03	1.804E+00	2.151E+00	2.228E+00	2.012E+12	1.880E+12	1.438E+11
96	1.29900E+03	1.463E−04	6.598E+03	1.390E+00	3.923E+00	4.009E+00	3.780E+12	3.641E+12	1.489E+11
97	1.21400E+03	2.461E−04	6.576E+03	1.159E+00	6.640E+00	6.742E+00	6.488E+12	6.322E+12	1.760E+11
98	1.14300E+03	3.830E−04	6.531E+03	9.900E−01	1.038E+01	1.049E+01	1.028E+13	1.009E+13	1.995E+11
99	1.10100E+03	4.997E−04	6.474E+03	8.959E−01	1.356E+01	1.369E+01	1.360E+13	1.340E+13	2.104E+11
100	1.06500E+03	6.299E−04	6.400E+03	8.235E−01	1.712E+01	1.726E+01	1.742E+13	1.722E+13	2.091E+11
101	1.03200E+03	7.814E−04	6.315E+03	7.647E−01	2.126E+01	2.141E+01	2.198E+13	2.179E+13	2.021E+11
102	1.00300E+03	9.476E−04	6.225E+03	7.193E−01	2.580E+01	2.596E+01	2.711E+13	2.693E+13	1.903E+11
103	9.71000E+02	1.177E−03	6.100E+03	6.885E−01	3.206E+01	3.225E+01	3.445E+13	3.428E+13	1.727E+11
104	9.46000E+02	1.400E−03	5.969E+03	6.722E−01	3.813E+01	3.835E+01	4.193E+13	4.178E+13	1.513E+11
105	9.00000E+02	1.947E−03	5.720E+03	6.411E−01	5.306E+01	5.335E+01	6.097E+13	6.086E+13	1.162E+11
106	8.54000E+02	2.753E−03	5.430E+03	6.079E−01	7.504E+01	7.543E+01	9.092E+13	9.085E+13	8.055E+10
107	8.00000E+02	4.240E−03	5.090E+03	5.634E−01	1.156E+02	1.162E+02	1.495E+14	1.495E+14	5.458E+10
108	7.50000E+02	6.480E−03	4.840E+03	5.201E−01	1.768E+02	1.775E+02	2.405E+14	2.404E+14	4.762E+10
109	7.00000E+02	1.011E−02	4.640E+03	4.738E−01	2.759E+02	2.769E+02	3.914E+14	3.914E+14	5.159E+10
110	6.60000E+02	1.461E−02	4.510E+03	4.390E−01	3.990E+02	4.004E+02	5.825E+14	5.825E+14	6.424E+10
111	6.15000E+02	2.234E−02	4.435E+03	4.064E−01	6.102E+02	6.120E+02	9.059E+14	9.058E+14	9.163E+10
112	5.60000E+02	3.778E−02	4.400E+03	3.755E−01	1.032E+03	1.035E+03	1.545E+15	1.545E+15	1.467E+11
113	5.25000E+02	5.282E−02	4.410E+03	3.609E−01	1.444E+03	1.447E+03	2.156E+15	2.155E+15	1.996E+11
114	4.90000E+02	7.376E−02	4.435E+03	3.501E−01	2.017E+03	2.021E+03	2.994E+15	2.993E+15	2.718E+11
115	4.50000E+02	1.077E−01	4.485E+03	3.420E−01	2.945E+03	2.951E+03	4.324E+15	4.322E+15	3.871E+11
116	4.00000E+02	1.715E−01	4.590E+03	3.381E−01	4.690E+03	4.699E+03	6.729E+15	6.726E+15	6.034E+11
117	3.50000E+02	2.701E−01	4.700E+03	3.412E−01	7.387E+03	7.401E+03	1.035E+16	1.034E+16	9.337E+11
118	3.00000E+02	4.211E−01	4.805E+03	3.667E−01	1.151E+04	1.154E+04	1.578E+16	1.577E+16	1.433E+12
119	2.50000E+02	6.500E−01	4.907E+03	4.919E−01	1.774E+04	1.781E+04	2.381E+16	2.379E+16	2.182E+12
120	2.00000E+02	9.933E−01	5.010E+03	6.882E−01	2.702E+04	2.721E+04	3.552E+16	3.549E+16	3.308E+12
121	1.75000E+02	1.223E+00	5.080E+03	7.918E−01	3.319E+04	3.350E+04	4.303E+16	4.299E+16	4.102E+12
122	1.50000E+02	1.500E+00	5.165E+03	9.003E−01	4.060E+04	4.109E+04	5.178E+16	5.173E+16	5.132E+12
123	1.25000E+02	1.831E+00	5.288E+03	1.023E+00	4.942E+04	5.017E+04	6.156E+16	6.150E+16	6.596E+12
124	1.00000E+02	2.223E+00	5.431E+03	1.153E+00	5.979E+04	6.092E+04	7.251E+16	7.244E+16	8.748E+12
125	7.50000E+01	2.683E+00	5.607E+03	1.286E+00	7.186E+04	7.350E+04	8.441E+16	8.434E+16	1.233E+13
126	5.00000E+01	3.213E+00	5.826E+03	1.434E+00	8.570E+04	8.804E+04	9.687E+16	9.680E+16	1.909E+13
127	3.50000E+01	3.567E+00	6.006E+03	1.522E+00	9.489E+04	9.772E+04	1.040E+17	1.040E+17	2.729E+13
128	2.00000E+01	3.944E+00	6.231E+03	1.601E+00	1.047E+05	1.081E+05	1.107E+17	1.106E+17	4.258E+13
129	1.00000E+01	4.208E+00	6.397E+03	1.651E+00	1.116E+05	1.153E+05	1.149E+17	1.148E+17	5.893E+13
130	0.00000E+00	4.482E+00	6.583E+03	1.696E+00	1.188E+05	1.228E+05	1.188E+17	1.187E+17	8.397E+13
131	−1.00000E+01	4.765E+00	6.780E+03	1.763E+00	1.261E+05	1.305E+05	1.223E+17	1.222E+17	1.206E+14

TABLE 26—*Continued*

	h (km)	m (g cm^{-2})	T (K)	V (km s^{-1})	p_g (dyn cm^{-2})	p_{tot} (dyn cm^{-2})	n_H (cm^{-3})	n_{H1} (cm^{-3})	n_e (cm^{-3})
132..................	−2.00000E+01	5.055E+00	7.020E+03	1.835E+00	1.336E+05	1.385E+05	1.251E+17	1.249E+17	1.828E+14
133..................	−3.00000E+01	5.351E+00	7.280E+03	1.912E+00	1.411E+05	1.466E+05	1.274E+17	1.271E+17	2.794E+14
134..................	−4.00000E+01	5.651E+00	7.590E+03	1.986E+00	1.489E+05	1.548E+05	1.287E+17	1.283E+17	4.465E+14
135..................	−5.00000E+01	5.954E+00	7.900E+03	2.000E+00	1.570E+05	1.631E+05	1.303E+17	1.296E+17	6.910E+14
136..................	−6.00000E+01	6.261E+00	8.220E+03	2.000E+00	1.654E+05	1.715E+05	1.315E+17	1.305E+17	1.050E+15
137..................	−7.00000E+01	6.570E+00	8.540E+03	2.000E+00	1.738E+05	1.800E+05	1.326E+17	1.311E+17	1.547E+15
138..................	−8.00000E+01	6.882E+00	8.850E+03	2.000E+00	1.823E+05	1.886E+05	1.336E+17	1.315E+17	2.196E+15
139..................	−9.00000E+01	7.197E+00	9.120E+03	2.000E+00	1.909E+05	1.972E+05	1.351E+17	1.322E+17	2.929E+15
140..................	−1.00000E+02	7.515E+00	9.380E+03	2.000E+00	1.995E+05	2.059E+05	1.366E+17	1.328E+17	3.808E+15

calculated lines the Gaussian convolution in wavelength described below. We determine the width of this convolution from a comparison of the calculated and observed spectra.

Figure 9 shows the prominent multiplet of C III that has six line components between 117.49 and 117.64 nm. This is the 4/2 line in Table 10. The SUMER observed profile is plotted in green. The dashed curve in red is the result of convolving the calculated profile with a Gaussian profile function having a FWHM of 0.015 nm. Lesser convolution applied to the calculated profile would give a separate emission peak just longward of the bright central peak that would not agree with the observed partial blending of these two line components. The dashed curve in blue is the calculated profile with zero convolution. This convolution was applied to all of the calculated line profiles compared here with the SUMER atlas lines.

These calculated profiles are determined using the broadening velocity distribution shown in Figure 8 (derived from Table 1) and listed in Table 26. The peak intensity at 117.571 nm is formed in the transition region where the temperature and broadening velocity are roughly 52,690 K and 20.75 km s^{-1}, respectively. Figure 10 shows the corresponding unconvolved and convolved profiles calculated with zero broadening velocity, but with the same C7 model atmosphere that uses the turbulent pressure velocity listed in Table 26.

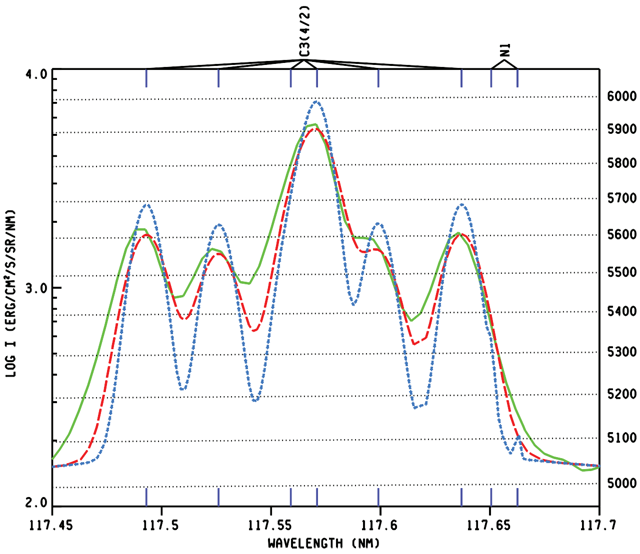

FIG. 9.—Observed 117.49–117.64 nm C III multiplet (*green solid line*) compared with the convolved calculated profile (*red long-dashed line*), and with the unconvolved calculated profile (*blue short-dashed line*). These results use $V(h)$ both for nonthermal broadening and as a turbulent pressure contribution. The scale on the right shows the brightness temperatures in K corresponding to the intensities on the left. The 0.015 nm FWHM convolution shown here was applied to all of the calculated lines that we show in comparison with the SUMER atlas data.

While the intrinsic broadening is masked to a large extent by the convolution, the 20.75 km s^{-1} broadening velocity gives a better result in this case than zero broadening. It would clearly be better to determine the broadening velocity distribution by comparing models of separate internetwork and network regions with observations of these regions with high spatial and spectral resolution. Since systematic data for these separate regions is not yet available, only the quiet-Sun averages are considered here.

Figure 11 shows the 9/1 multiplet of C I with six line components between 132.88 and 132.96 nm. As before, the SUMER profile is plotted in green, and the broken red and blue curves are the calculated convolved and unconvolved profiles, respectively. The unconvolved calculated profiles have central reversals as a result of the initial outward increase of the line source function followed by a decrease in the optically thin region. The central intensity of the 132.88 nm component is formed in the midchromosphere where $T = 6660$ K and $V = 5.54$ km s^{-1}.

Figure 12 shows the corresponding unconvolved and convolved profiles with zero broadening velocity, based on the same model atmosphere.

Differences can be seen between the unconvolved profiles in Figures 11 and 12, but the convolved profiles are almost the

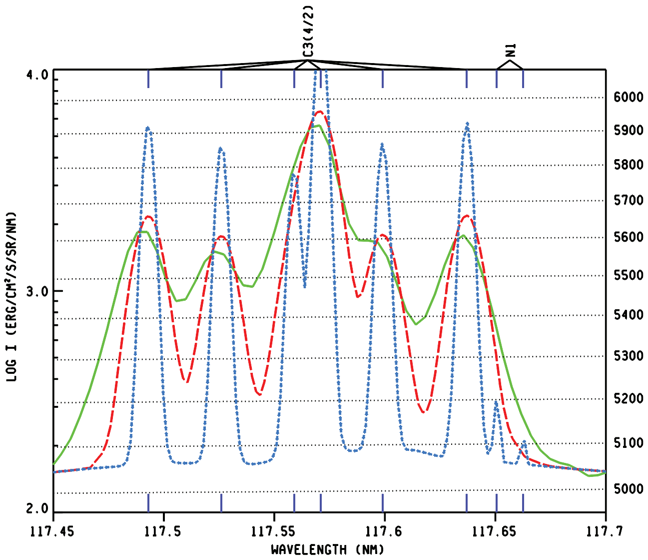

FIG. 10.—Profiles as in Fig. 9, using the same model atmosphere, but with zero broadening velocity.

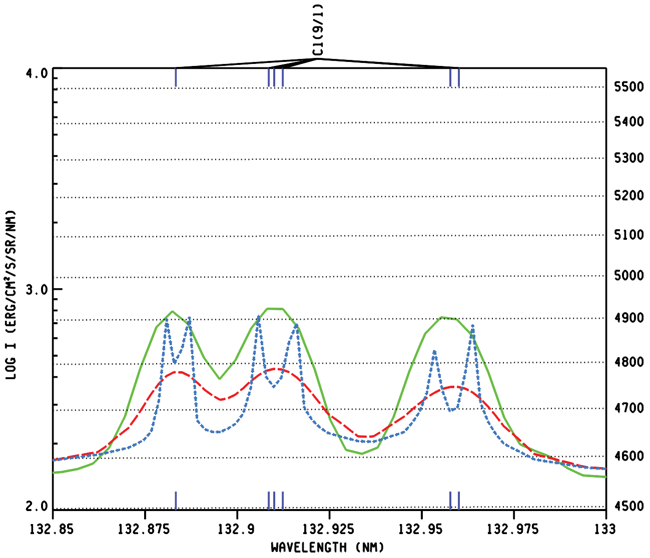

Fig. 11.—Observed 132.88–132.96 nm C i multiplet (*green solid line*) compared with the convolved calculated profile (*red long-dashed line*), and with the unconvolved calculated profile (*blue short-dashed line*). These results use $V(h)$ both for nonthermal broadening and as a turbulent pressure contribution. The scale on the right shows the brightness temperatures in K corresponding to the intensities on the left.

same. Thus, we cannot distinguish between zero broadening and 5.54 km s^{-1} broadening from these SUMER atlas profiles. Observations of separate internetwork and network regions with high spatial resolution are needed to determine $V(h)$ in the mid-chromosphere.

15. HYDROGEN LINES

Figure 13 shows the contribution functions for the line centers of the hydrogen Lyman lines 2/1, 3/1, 4/1, 6/1, 9/1, 12/1, and 15/1, the Balmer lines 3/2, 4/2, and 5/2, and the Paschen line 4/3, defined in the same way as for the continuum contributions shown in Figure 2. The central intensity of the Hα (3/2) line is formed in the chromosphere, but the central intensities of the Hβ, Hγ, and Pα lines have substantial contributions from the photosphere. For these subordinate lines the photospheric contributions become much greater at wavelengths displaced from line center. The central intensities of the resonance lines are formed mainly in the transition region, but Figure 13 shows that there are upper-chromospheric contributions to the central intensities of the highest Lyman lines. For wavelengths displaced from line center, chromospheric contributions become substantial.

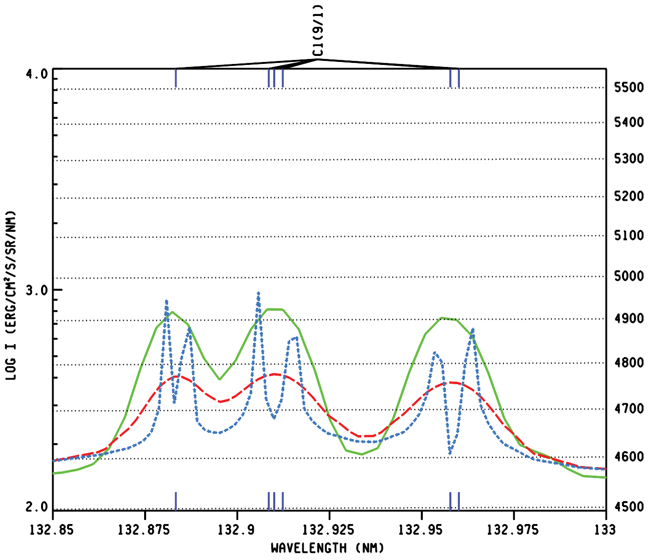

Fig. 12.—Profiles as in Fig. 11, using the same model atmosphere, but with zero broadening velocity. (A detailed plot of the blue curve with finer wavelength spacing shows that the three line components are each almost symmetric.)

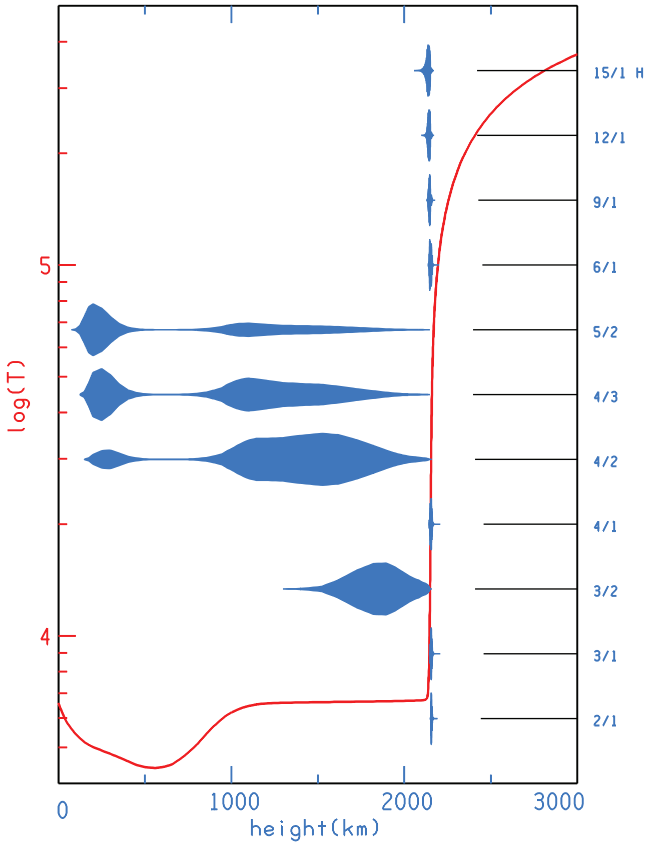

Fig. 13.—Line-center contribution functions for hydrogen Lyman, Balmer, and Paschen lines.

In this paper we do not discuss the Balmer and Paschen lines other than show their line-center contribution functions in Figure 13. For a non-LTE study of these lines in the visible spectrum, see Przybilla & Butler (2004b). For non-LTE studies of the infrared hydrogen lines, see Rutten & Carlsson (1994), Carlsson & Rutten (1994), and Avrett et al. (1994a).

In Figure 14 we show the contribution functions for Lyα wavelengths displaced from line center. Lyα is a strong centrally reversed emission line, centered at 121.567 nm, with blue and red peak intensities near 121.55 and 121.59 nm, respectively. The emission from these peak wavelengths contributes as much or more to the Lyα net radiative losses than does the contribution from the line center. As indicated in this figure the blue-peak intensity at 121.55 nm is formed in the upper chromosphere. The dI/dh distributions, normalized to unity at maximum, are plotted in the bottom panel of this figure. The contributions from two other wavelengths in the blue wing and three wavelengths in the red wing are also shown. The chromospheric origin of a large part of the Lyα emission is consistent with the interpretation discussed earlier that Lyman-line cooling is significant in the upper chromosphere.

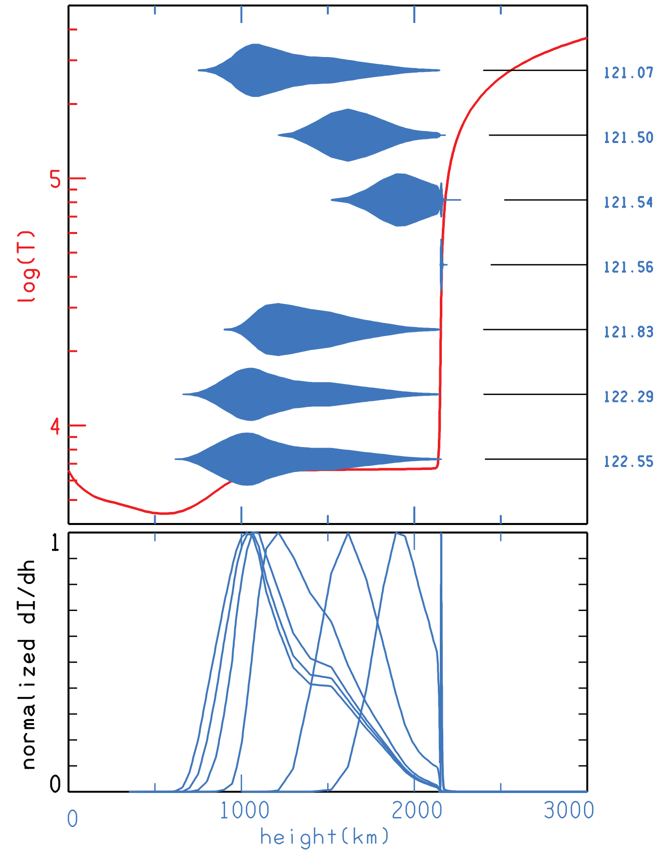

Fig. 14.—Contribution functions for wavelengths in the center and wings of the Lyα line. The blue peak intensity is at 121.55 nm. Each dI/dh distribution relative to the maximum value is plotted in the bottom panel.

Figure 15 shows the frequency-independent Lyα line source function $S(2/1)$ and the Planck function at 121.567 nm plotted against height. The values of the line-center optical depth $\tau(2/1)$ are shown at the top. The source function has a maximum in the upper chromosphere because of an overpopulation of the $n = 2$ level of hydrogen relative to LTE. The reason for this overpopulation is that in the Balmer ($n = 2$) continuum the Planck function B at chromospheric heights is much larger than the mean intensity J, which is formed in the photosphere. Since B enters the recombination rate and J enters the photoionization rate, the $n = 2$ number density is larger than it would be for $J = B$.

The frequency-independent source function S in Figure 15 is given by

$$S = \frac{2h\nu^3/c^2}{(g_2 n_1/g_1 n_2) - 1}, \tag{9}$$

where n_1 and n_2 are the number densities for levels 1 and 2, and g_1 and g_2 are the corresponding statistical weights. In LTE the first term in the denominator of this equation is exp $(h\nu/kT)$, so that S becomes the Planck function. The frequency-dependent source function for the Lyα line is equal to S in the Doppler core of the line but for strong lines approaches the monochromatic mean intensity in the far wings, according to the equations of partial frequency redistribution (PRD).

Figure 16 shows the extended wings of the Lyα line over the wavelength range 118–125 nm. Our treatment of Stark broadening is approximate, which may account for some of the differences between the observed spectrum (in green) and the calculated one (in red).

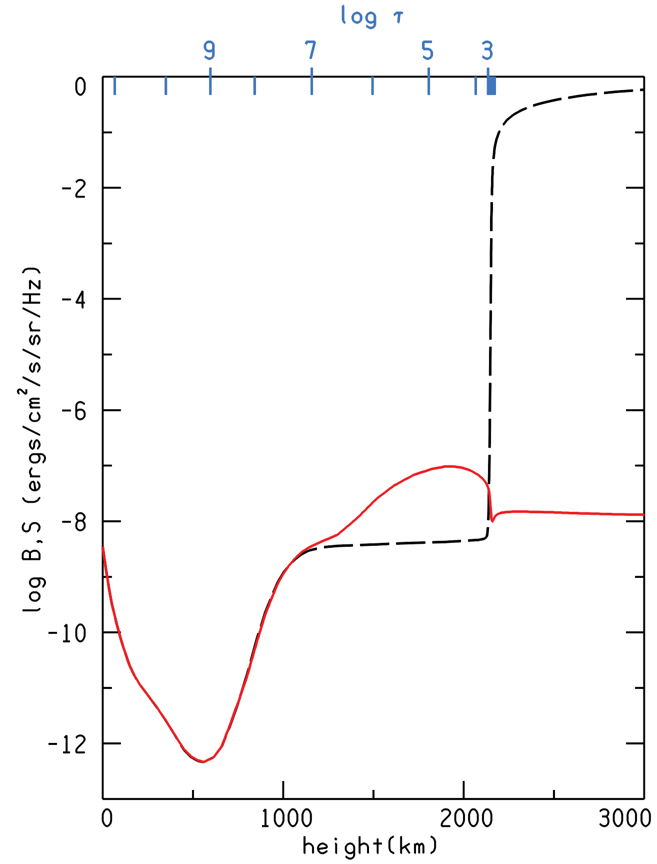

Fig. 15.—Lyα frequency-independent source function S (*red solid line*) and line-center Planck function B (*black dashed line*) vs. height (*bottom*) and line-center optical depth (*top*).

Figure 17 shows the central part of the Lyα line, from 121.48 to 121.65 nm at disk center. The green curve, from the SUMER atlas data file, has reduced spectral resolution at these peak intensity values due to instrumental modulation. The circular data points represent a typical quiet-Sun profile from the *Solar Maximum Mission* (*SMM*) observations of Fontenla et al. (1988; J. M. Fontenla, private commumication). These intensities in the line wings are affected by scattered light from the brighter

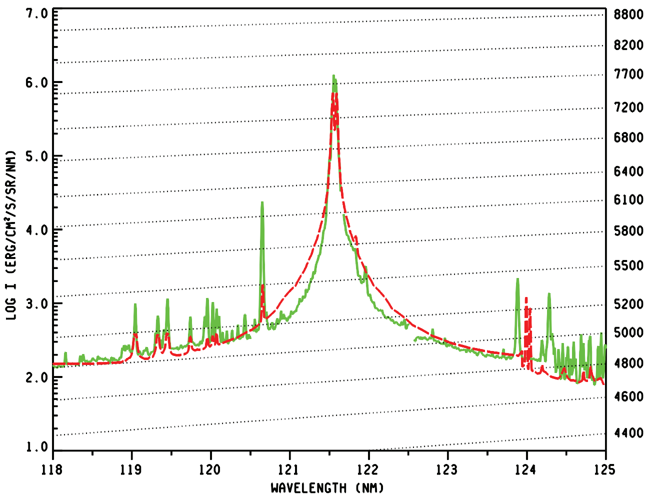

Fig. 16.—Observed (*green solid line*) and calculated (*red dashed line*) Lyα line in the wavelength range 118–125 nm.

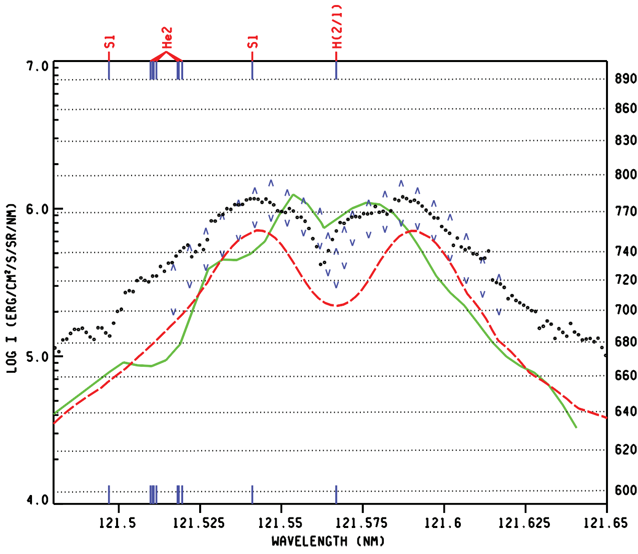

FIG. 17.—Calculated intensity near the center of the Lyα line (*red dashed line*) compared with SUMER, SMM, and *OSO 8* observations.

line core. The ∧ and ∨ symbols indicate typical network and cell profiles observed by Bocchialini & Vial (1994, their Fig. 38b) with the LPSP instrument on *OSO 8* (Artzner et al. 1997). We show in this figure the published intensities without attempting to assess the instrumental uncertainties.

The profile that we compute from model C7 is shown in red. We find that the computed profile is generally insensitive to the detailed temperature distribution but that the intensities in the core of the line generally increase and decrease as the total pressure in the transition region is increased and decreased (see Fontenla et al. 1991), which occurs as the height of the transition region is shifted inward or outward, respectively. As indicated in Table 26, the total pressure at the base of the transition region ($T = 7950$ K, $h = 2142$ km) is 0.107 dyn cm^{-2} for model C7. We could obtain better agreement in Figure 17 by moving the transition region inward, and this should also improve the agreement with the millimeter observation in Figure 3, but because of practical time constraints we have not continued further modeling adjustments for this paper.

The other Lyman lines depend on the height of the transition region and the transition region pressure in the same way. The Lyβ line is shown in panel 10 of Figure 23 in § 17, and other panels of Figure 23 show higher Lyman lines. The observed Lyβ line has a small but noticeable central reversal, as shown by Warren et al. (1998) and Meier (1995), but we have not been able to reproduce this feature in model C7 (for the calculated profile before convolution) while satisfying other constraints.

We calculate explict Lyman lines up to $n = 15$ and then approximate the series of higher lines as they merge into the Lyman continuum. We have done this in a simple way and hope to improve it in the future on the basis of the careful analysis of non-LTE line merging by Hubeny et al. (1994).

For detailed studies of the temporal variations of the hydrogen Lyman lines and Lyman continuum, see Curdt & Heinzel (1998), Curdt et al. (1999), Kariyappa et al. (2001), and Wilhelm & Kalkofen (2003).

Griffiths et al. (1999) carried out a study of line and continuum emission observed with the SUMER spectrograph covering a wide range of temperatures in the transition region. Their results indicate the presence of structures that extend from the chromosphere, through the entire transition region, and up into the corona. They suggest that much of the emission at transition region temperatures is coming from an intermediate layer in a continuous, stratified solar atmosphere and not from so-called unresolved fine structures. They show spatial intensity distributions from the C I continuum (near 124 nm), and the Lyman continuum (near 78.8 nm) and from lines of O II–V, N II–V, and Fe XII. Their analysis indicates that the electron number density in the transition region lies between 1.1×10^9 and 7.4×10^9, which is consistent with the range of values listed in Table 26.

TABLE 27

C I–IV LINE FORMATION DEPTHS AND TEMPERATURES

Index	T (K)	Ion	Line	λ (nm)	Panel
49	68000	C IV	2/1	154.8	41
51	60790	C III	8/3	69.1	40
53	55020	C III	6/3	124.7	39
54	52690	C III	4/2	117.6	38
57	46800	C III	3/1	97.7	37
61	39400	C II	9/1	68.7	36
63	34580	C II	5/1	90.4	35
64	32260	C II	4/1	103.6	34
65	29500	C II	3/1	133.5	33
73	10980	C II	15/3	80.0	32
73	10980	C II	12/2	80.7	31
73	10980	C II	14/3	81.0	30
76	7248	C II	6/1	85.8	29
94	6623	C II	15/4	94.6	28
94	6623	C II	10/3	132.4	27
94	6623	C II	13/3	106.6	26
94	6623	C II	8/2	101.0	25
95	6610	C II	15/5	109.3	24
71	15760	C I	11/1	119.3	23
81	6740	C I	5/1	165.7	22
86	6686	C I	18/1	94.6	21
87	6680	C I	7/1	156.1	20
89	6667	C I	10/1	127.7	19
90	6660	C I	9/1	133.0	18
92	6643	C I	15/1	112.2	17
92	6643	C I	10/2	146.3	16
93	6633	C I	12/1	115.8	15
93	6633	C I	13/1	114.0	14[a]
93	6633	C I	11/2	135.9	13
94	6623	C I	12/2	131.1	12
95	6610	C I	14/1	112.9	11
95	6610	C I	13/2	128.8	10
98	6531	C I	14/2	127.5	9
98	6531	C I	11/3	160.3	8
100	6400	C I	17/4	143.2	7
102	6225	C I	12/3	154.2	6
104	5969	C I	15/2	126.6	5
104	5969	C I	13/3	151.1	4
106	5430	C I	6/1	161.4	3
109	4640	C I	14/3	149.3	2
110	4510	C I	15/3	148.1	1

NOTES.—Depth index and temperature at the height of the maximum line-center contribution to the strongest line component (or to the strongest component not obscured by blending), and the wavelength of this component, and the panel number in Fig. 19, where the calculated and observed profiles are compared. The contribution plots in Fig. 18 are in the same order.

[a] Includes C I 16/2 and C II 11/3 and 14/5.

16. CARBON LINES

In Table 27 we list 41 transitions of C I–IV (and three additional ones in the footnote). This list includes all of the transitions given in Tables 4, 8, and 10. In each case we give the depth index, from

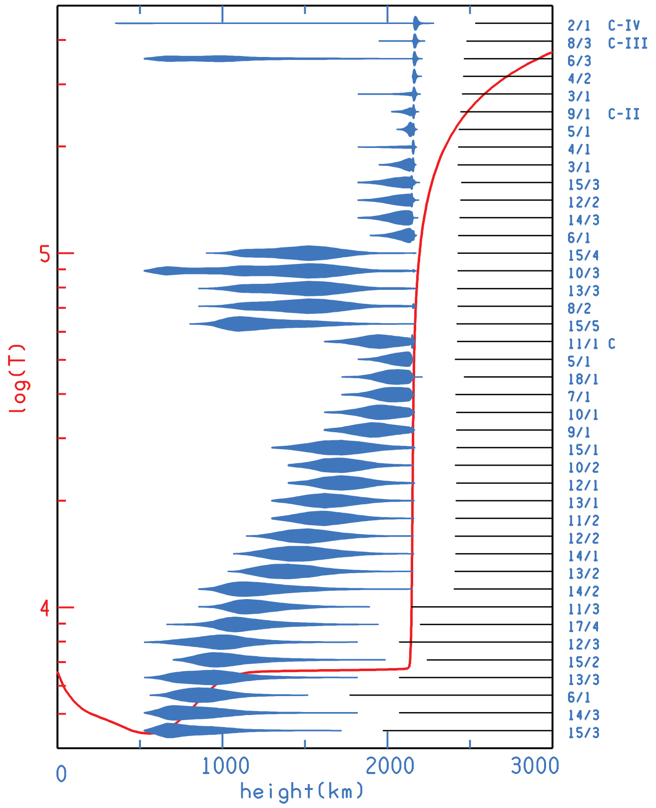

Fig. 18.—Line-center contribution functions dI/dh for the C i–iv lines listed in Table 27. Intensities at wavelengths displaced from line center originate deeper in the atmosphere, as discussed in § 16.1. These functions include continuum as well as line contributions, thus, e.g., accounting for the contributiions to the weak 6/3 line of C iii from the low chromosphere.

Table 26, and the temperature corresponding to the maximum contribution to the line-center intensity. Plots of these contribution functions are shown in Figure 18. The wavelength for each transition in Table 27 is the wavelength of the strongest line component (or the strongest component not obscured by blending), and both the depth index and temperature of the maximum of the contribution function are for that component.

The 41 panels of Figure 19 compare the calculated spectrum (in red) with SUMER observations (in green) or with HRTS observations (in brown). We compare with SUMER profiles for wavelengths below 148 nm and with HRTS profiles for longer wavelengths.

For $\lambda < 148$ nm our calculated profiles are convolved with a Gaussian profile function having a FWHM of 0.015 nm, as discussed in § 14. For longer wavelengths we use 0.008 instead, since the HRTS data in the Brekke atlas have less spatial averaging by roughly a factor of 2.

It should be noted that in Figure 19 the largest differences between computed and observed intensities (panels 36 and 40) occur at short wavelengths in the Lyman continuum where our computed continuum intensitites are smaller than observed.

16.1. *The* C ii 133.5 nm *Multiplet*

The C ii 3/1 transition in panel 33 of Figure 19 consists of the multiplet lines at 133.45 and 133.57 (=133.566+133.571) nm. This well-studied UV multiplet is discussed at length by Judge et al. (2003). They consider the full range of SUMER observations of these lines, and they compare with radiation hydrodynamic simulations, and with a one-dimensional, time-independent simulation. Neither of these show good agreement with the observations, but our calculated emission in panel 33 of Figure 19 is well below the observations and not in good agreement either.

The Judge et al. radiation hydrodynamic calculations require further development to apply fully to the upper chromosphere and transition region where these lines are formed. Their one-dimensional, time-independent calculation required the specification of a semiempirical atmospheric model, and the VAL model A was chosen. The VAL models introduced an ad hoc plateau in the lower transition to account for the observed hydrogen Lyman lines, assuming local statistical equilibrium. The earlier study by Lites et al. (1978) using *OSO 8* observations also used a VAL model and found the results to be extremely sensitive to the temperature and extent of the plateau near 20,000 K. As discussed in § 3, the introduction by Fontenla et al. of energy transport in the transition region by particle diffusion in addition to thermal conduction removes the need for this plateau. Judge et al. did consider this modification but concluded that this multiplet "should be formed under conditions of higher optical depth than is likely to occur in models in which the line can be formed by diffusion of energy down from the corona (e.g., Fontenla et al. 1990 and references therein)." The calculations reported here include such an energy-balance transition region. We show in detail where these lines are formed, based on model C7, but our results are provisional, given the limited agreement shown in panel 33 of Figure 19.

It should be understood that while the Fontenla et al. papers determined the effects of H, He i, and He ii diffusion, the possible effects of carbon and carbon-ion diffusion have not been investigated in any detail. Thus, our calculations using model C7 assume local statistical equilibrium for all atoms and ions except H, He i, and He ii.

The profiles calculated from a one-dimensional model can have detailed features that do not appear in observed profiles, due to spatial averaging, temporal averaging, and instrumental resolution. The 133.45 and 133.57 lines that we calculate are centrally reversed emission lines. The 133.45 line is almost symmetric, but the combined 133.566+133.571 line is asymmetric with a higher blue peak. In panel 33 of Figure 19 the convolved profiles are compared with the observed ones.

We avoid the complexity of the stronger 133.566+133.571 blend and consider the 133.45 nm component. Contribution functions are determined at three wavelengths: line center, the blue peak 0.005 nm from line center, and the blue wing 0.01 nm from line center. We plot in Figure 20 the dI/dh contributions for these three wavelengths, showing that while the line center is formed in the transition region, there is an upper-chromospheric contribution to the peak intensity. In the line wing, 0.01 nm from line center, the chromospheric contribution from the deeper layers becomes roughly as important as the transition-region contribution.

Figure 20 also shows the Planck function versus height at 133.45 nm and the calculated frequency-independent source function for the C ii 3/1 line transition. We assume CRD (see § 11) and assume that the fine-structure levels are collisionally coupled so that the three lines have a common source function. Values of the line-center optical depth are indicated at the top of the graph. While line-center optical depth unity occurs in the upper chromosphere, the line center intensity is formed in the transition region.

We also plot in Figure 20 the net radiative cooling rate for the line transition (see eq. [21] of VAL). This function represents the net emission for the line as a whole and is consistent with the indicated contribution functions for different parts of the line. Thus, the C ii 133.5 nm multiplet has contributions from both the chromosphere and the transition region.

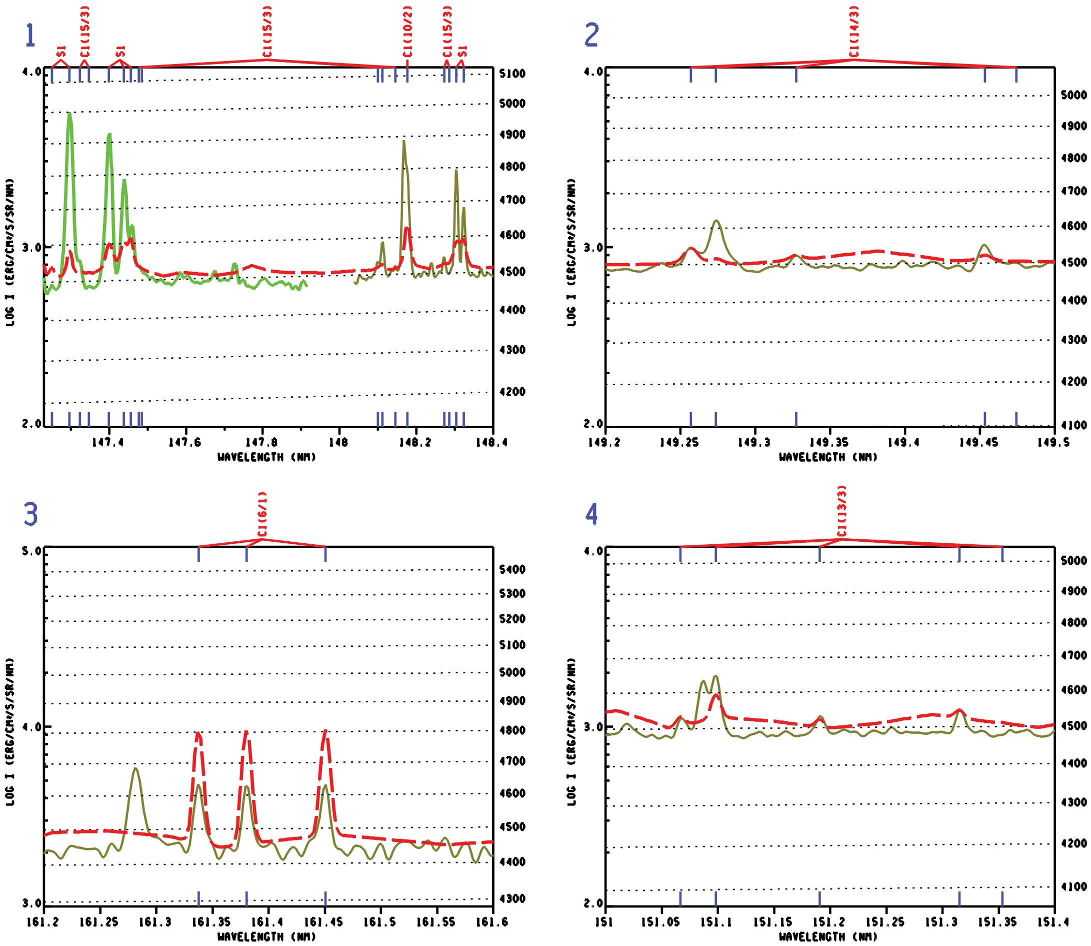

FIG. 19.—Calculated and observed profiles for the C i–iv lines in the SUMER and HRTS wavelength ranges, ordered by the panel indices in Table 27.

Judge et al. point out that the center-to-limb behavior of these lines indicates that they are formed in the chromosphere rather than in the transition region, since the observed integrated intensity does not increase abruptly at the limb in the manner of an optically thin transition-region line. The results in their Figure 9 show increases at the limb that conflict with observations. They give the results of two calculations, a radiation-hydrodynamic simulation and a semiempirical determination based on a VAL model that includes a transition-region plateau.

The center-to-limb behavior that we obtain with model C7 is displayed in Figure 21 and indicates that the integrated intensity has only a moderate increase at the limb. This figure shows the 133.45 nm profile at disk center (fractional radius $f = 0$), and at fractional radii 0.95, 0.97, and 0.99. Lites et al. found from *OSO 8* observations that the wavelength-integrated line intensities are limb-brightened primarily because the lines become broader near the limb rather than because of the outward temperature increase. Figure 21 shows this property along with the increase in central intensity from center to limb.

The calculated ratio of the 133.45 to 133.57 components in panel 33 of Figure 19 is closer to the observed value of about 1:1.4 than to the 1:2 ratio corresponding to the optically thin limit.

The Judge et al. paper is a study of the origin of basal emission from stellar atmospheres and is based on a comparison between simulations and observations of the C ii 133.5 nm multiplet. They discuss the issue of magnetic versus acoustic heating in relation to earlier work reviewed by Schrijver (1995) and based on the prevailing assumption that these multiplet lines are formed in the transition region. It is beyond the scope of the present paper to comment on the issue of acoustic versus magnetic heating of the chromosphere. We only point out here that only the centers of these lines are formed in the transition region while the intensities in the line wings originate in the upper chromosphere. For a general discussion of "where is my line formed?" see the review by Rutten (2007).

We note again, as shown in panel 33 of Figure 19, that our calculated C ii line intensities are much smaller than observed. Many of the C ii lines in other panels of this figure show similar disagreements. We have not attempted a study of various alternative rates and cross sections that might lead to better agreement.

16.2. C iii

Feldman et al. (1999) present high spatial resolution solar images in the C iii 97.70 nm line that show a wealth of small-scale, looplike structures. They find that looplike structures seen in transition region lines with length scales of 10″–20″ straddle the chromospheric network and have no chromospheric counterpart near their apparent footpoints. See also Feldman et al. (2001) for solar images in the C ii line at 103.70 nm, C iii at 124.74, C iv at 154.82, O i at 130.22, O iii at 70.3, O iv at 140.1, and O vi at 103.76.

17. OXYGEN LINES

In Table 28 we list the 43 transitions of O i–vi in the SUMER and HRTS wavelengths ranges, including all the transitions given in Tables 13, 16, 18, 20, and 22. In each case we give the line wavelength and the depth index and temperature for the maximum of

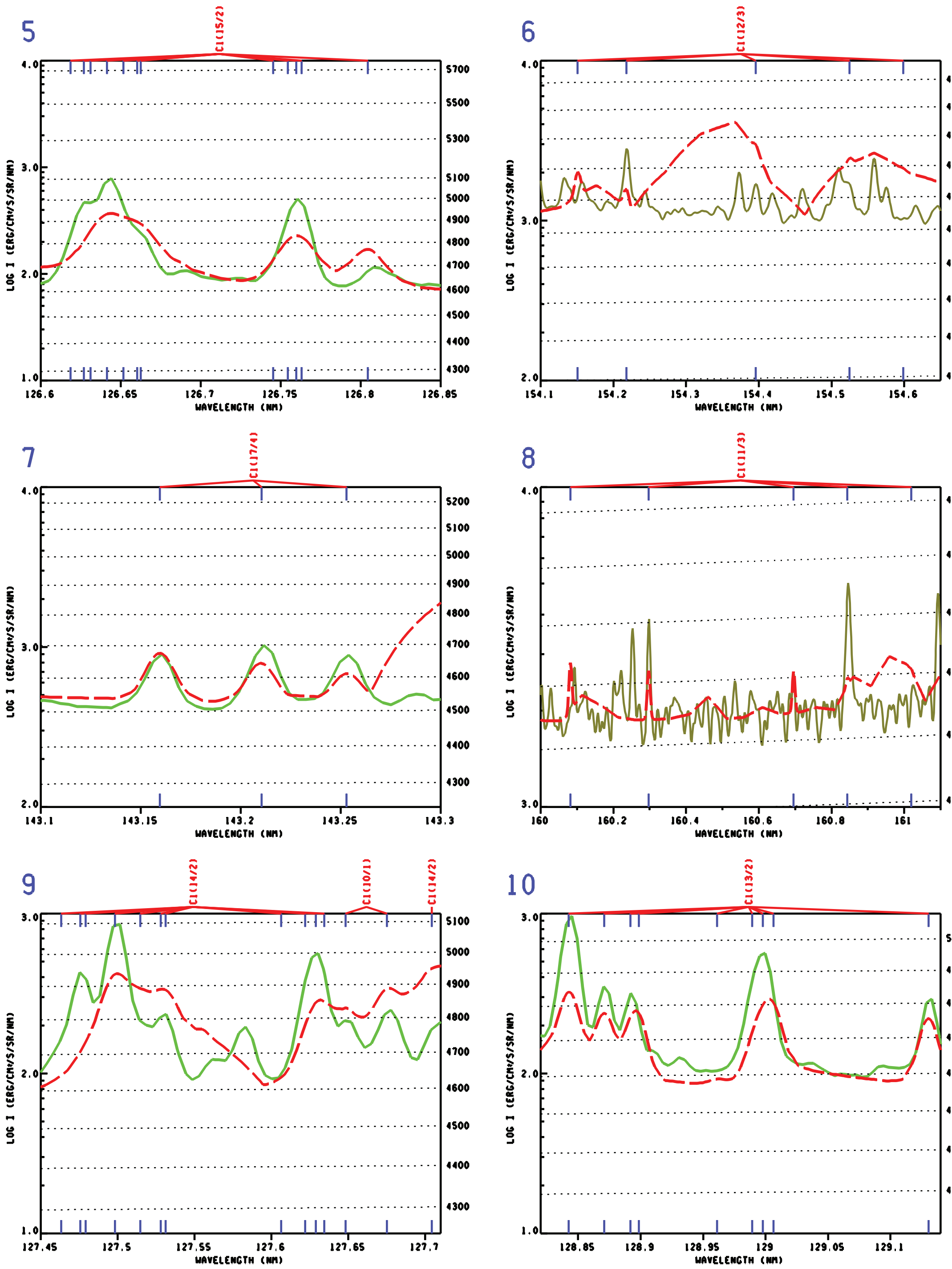

FIG. 19—*Continued*

the line-center contribution function as in Table 27 for C I–IV. The 43 contributions functions are plotted in Figure 22. Note that the O V 2/1 contribution function at line center shows a chromospheric continuum-opacity contribution that is larger than the contribution due to line opacity in the transition region.

The 25 panels of Figure 23 show the calculated and observed profiles of the O I–VI lines, and those of other lines at nearby wavelengths, compared with the SUMER observations.

As in Figure 19 for the carbon lines, the largest differences between the calculations and observations occur at short wavelengths in the Lyman continuum where the calculated continuum is below observed values.

18. COMMENTS ON THE OXYGEN LINE COMPARISONS

18.1. O I

Panel 4 of Figure 23 shows 20 individual lines of O I (corresponding to transitions 18/1, 18/2, 18/3, and 20/4), four hydrogen Lyman lines (7/1, 8/1, 9/1, and 10/1), and two He II lines (14/2 and 15/2). The wavelengths are listed in Table 29 for reference. These Lyman lines are included as explicit background lines as described in § 8 and are therefore taken into account in the O I and He II calculations. These particular O I and He II lines have not been included as explicit background lines. Thus, they do not affect the hydrogen calculations, but this is a minor inconsistency.

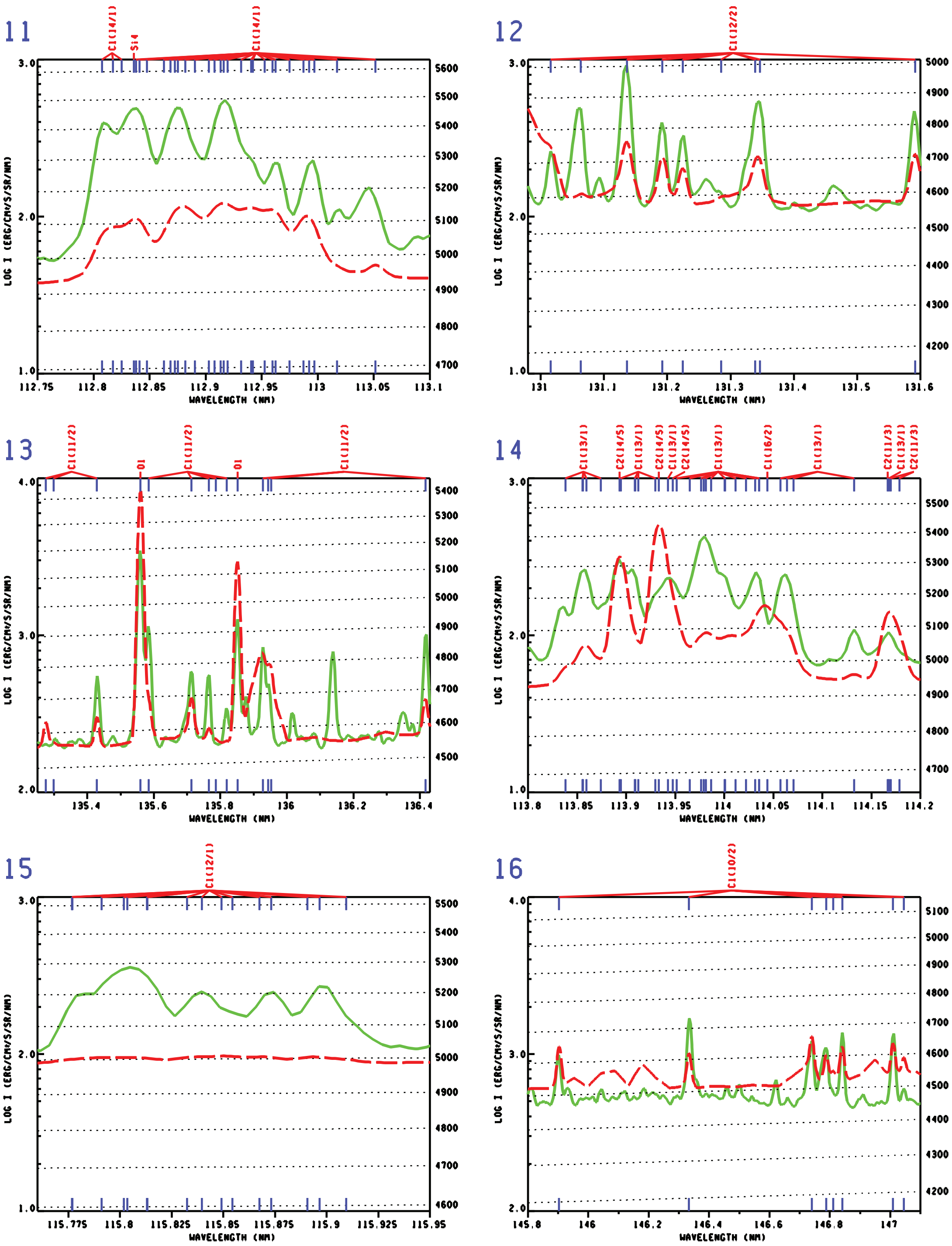

FIG. 19—*Continued*

Hydrogen Lyman lines also appear in panels 5, 6, 7, and 10 of Figure 23.

The resonance lines of O I in the Sun and stars have been studied in detail by Carlsson & Judge (1993), who provide references to earlier work. They discuss the Bowen fluorescence mechanism in which the Lyβ line excites the coincident O I 13/1 line (see panel 10 of Fig. 23), leading to subsequent emission in the 7/1, 7/2, and 7/3 triplet lines (panel 11) and in the 6/1 and 6/2 doublet lines (panels 3 and 2). At solar chromospheric densities collisional excitation is also a major contributor to the emission in these and other lines.

It is important to include PRD (see § 11 and the Appendix) in the calculation of the Lyβ line at 102.57 nm because of its strong interation with the O I line at 102.58 nm. Carlsson & Judge treated the Lyman lines in CRD with only Doppler broadening and zero damping wings as an approximation to PRD. Improved non-LTE calculations have been carried out by Koncewicz & Jordan (2007) that include PRD for Lyβ and other lines. They present model calculations for five cool stars: α Tau, β Gem, Procyon, ϵ Eri, and the Sun. Using the radiative transfer code developed by Uitenbroek (2001) they extended the earlier work of Miller-Ricci & Uitenbroek (2002) to study the effects of PRD,

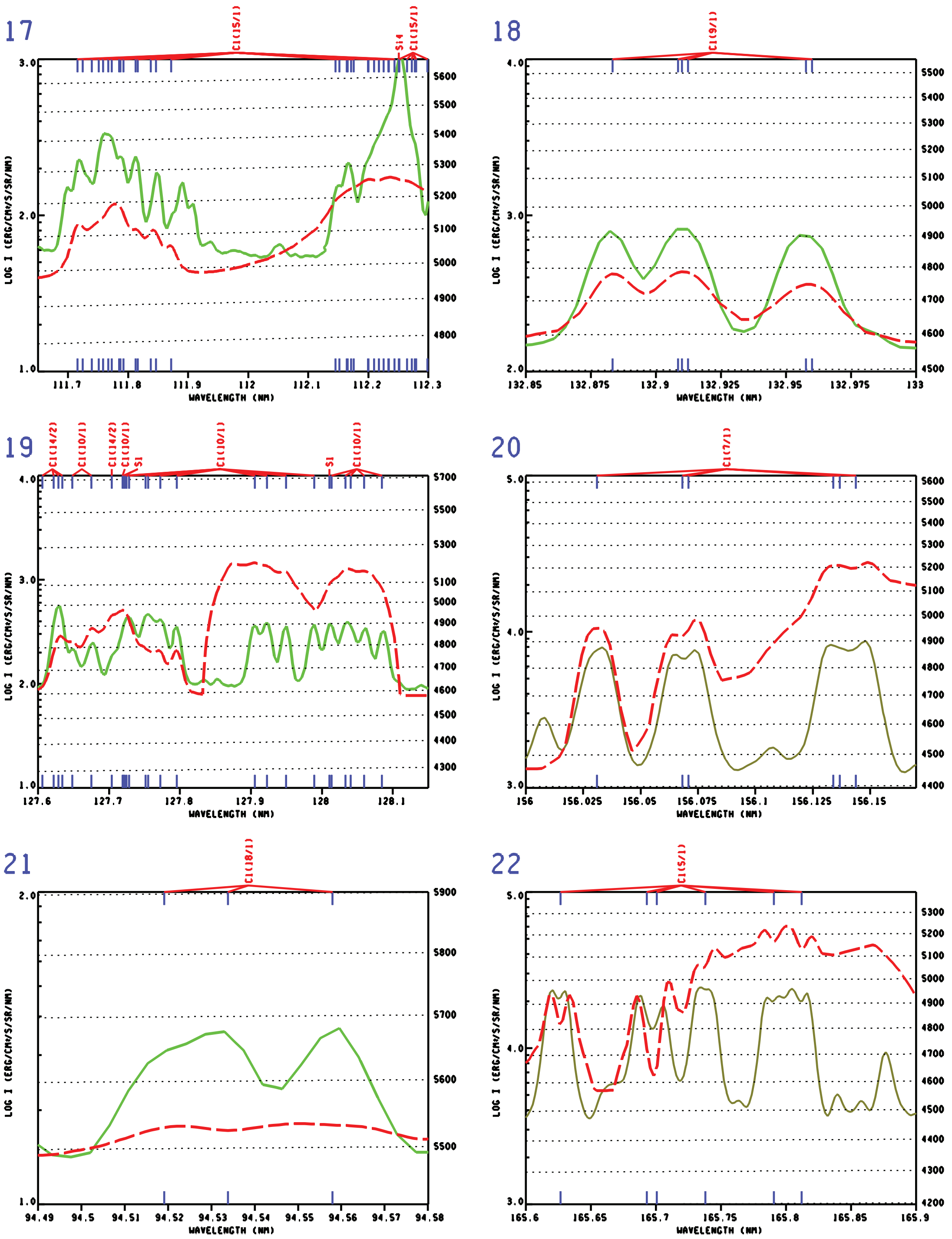

FIG. 19—*Continued*

and the effects of cross-redistribution (XRD), on the profiles of the O I resonance triplet (130.2, 130.5, 130.5 nm; panel 11). XRD refers to generalized PRD in multiplets with a common upper level in which there is coherent photon conversion: excitation in one of the multiplet lines followed by coherent de-excitation (in the atom's rest frame) in one of the other lines. Miller-Ricci & Uitenbroek found that XRD causes the calculated O I triplet lines to have narrower wings than ordinary PRD. Many previous calculations have shown PRD profiles to have narrower wings than those calculated using CRD.

We have not included XRD but show in Figure 24 the triplet profiles computed with PRD, which we use for the model C7 results, compared with the broader CRD profiles, and with the SUMER spectrum. The computed PRD profiles have narrower wings than the CRD profiles, as expected, and are in better agreement with the observed profiles. It is not apparent that yet narrower profiles would be in better agreement with the observations.

Both the Koncewicz & Jordan calculations and ours include (1) PRD for Lyβ, (2) its radiative excitation of the coincident O I line, and (3) the effect of this excitation on the other O I emission lines. Their calculations and ours differ in their use of the VAL model C and our use of model C7. The two calculations also undoubtedly differ in some of the adopted rates and cross sections. But our Figure 24 shows calculated profiles that are generally

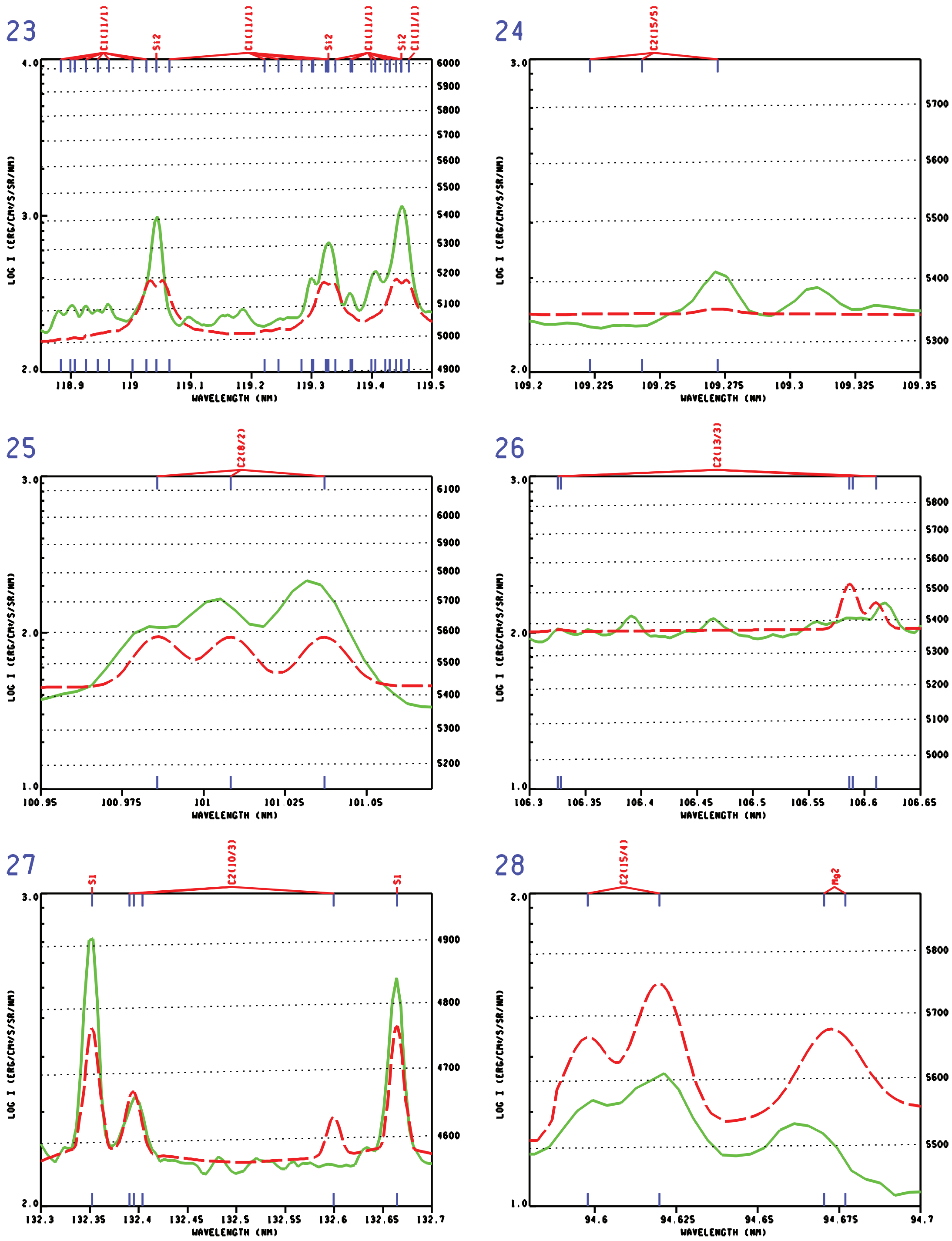

FIG. 19—*Continued*

consistent with the observations, while they find disagreements that they believe support the idea of a two-component atmosphere. While further study of the O I lines is clearly needed, our purpose here is an overview of the H, C I–IV, and O I–VI model calculations, and we defer a more detailed study to a future paper.

18.2. O III

We have shown in Table 25 the close wavelength correspondence between the 13/1 transition of O III having components between 30.342 and 30.380 nm and the He II resonance line at 30.379 nm. We include this photoexcitation of O III by He II. Bhatia et al. (1982) and Kastner et al. (1983) provide a detailed analysis of this Bowen (1935) fluorescence mechanism that substantially affects the solar oxygen line spectrum. See also Keenan & Aggarwal (1989).

Table 25 also shows the components of the O III 4/1 transition along with the O II 4/1 line components. Panel 14 of Figure 23 shows the computed and observed profiles. As noted in § 4.25 the O III results in panel 14 are based on the collision strengths of Aggarwal & Keenan (1999). In Figure 25 we add to the results shown in panel 14 the O III profiles calculated with the CHIANTI results instead (using the van Regemorter collision rates for those

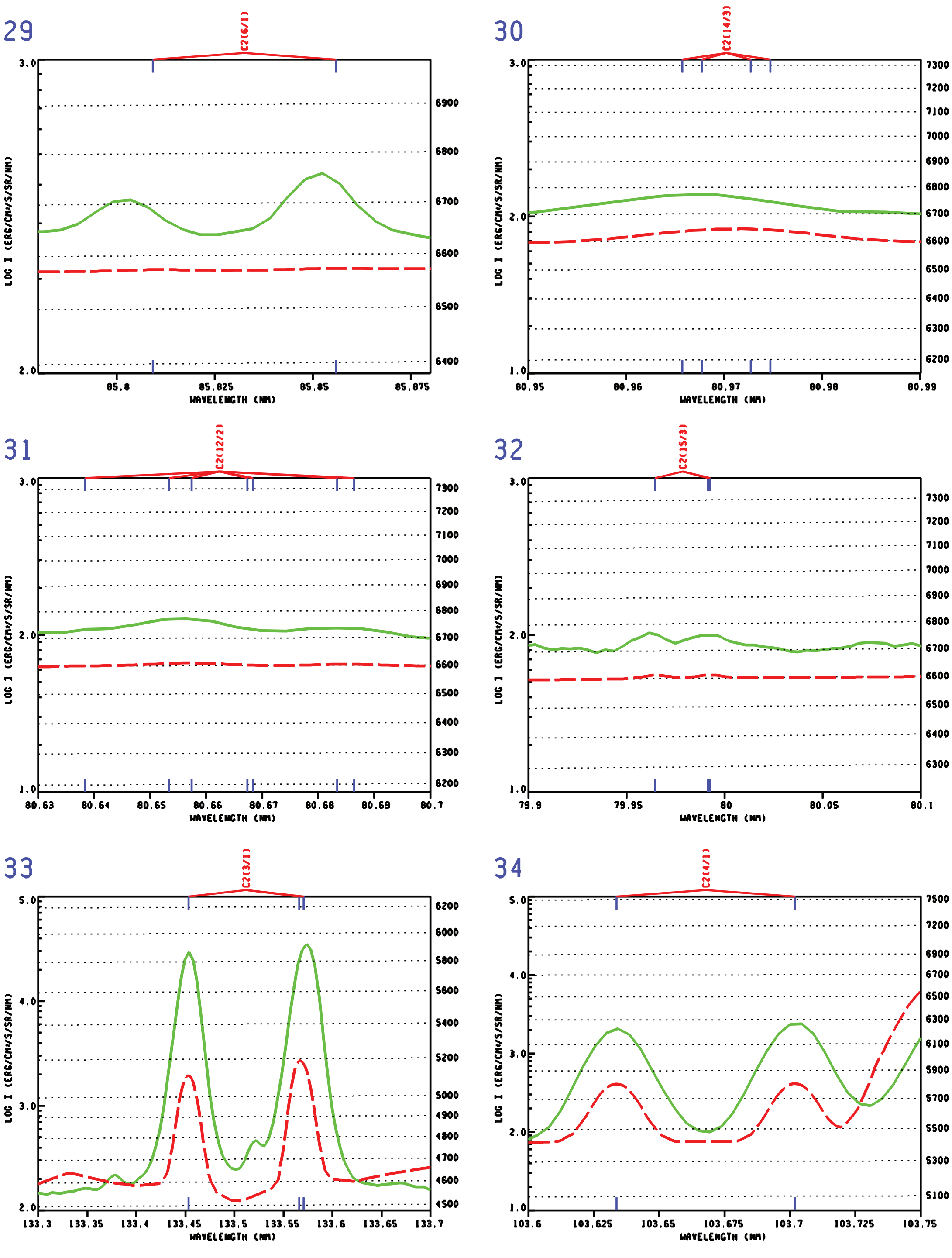

FIG. 19—*Continued*

not in the CHIANTI list). The O II results in Figure 25 are the same as before and have not been recalculated from the CHIANTI-determined O III profiles. The Aggarrwal & Keenan collision strengths appear to give better agreement with the observed profiles.

18.3. O IV

For the O IV line at 140.1 nm (panel 19 of Fig. 23), we give 76,330 K in Table 28 for the temperature where the maximum contribution to the line center occurs. This is half the value used by Doschek & Mariska (2001) based on the ionization equilibrium calculations of Arnaud & Rothenflug, but given the different ways of determining the peak temperature this factor of 2 may not be significant.

18.4. O V

The O V lines at 121.83 and 137.13 nm in panels 22 and 23 have been studied by Brekke (1993b) in a determination of redshifts, and downflows in the transition region, and by Keenan et al. (1995) with careful attention to relevant atomic data, in order to

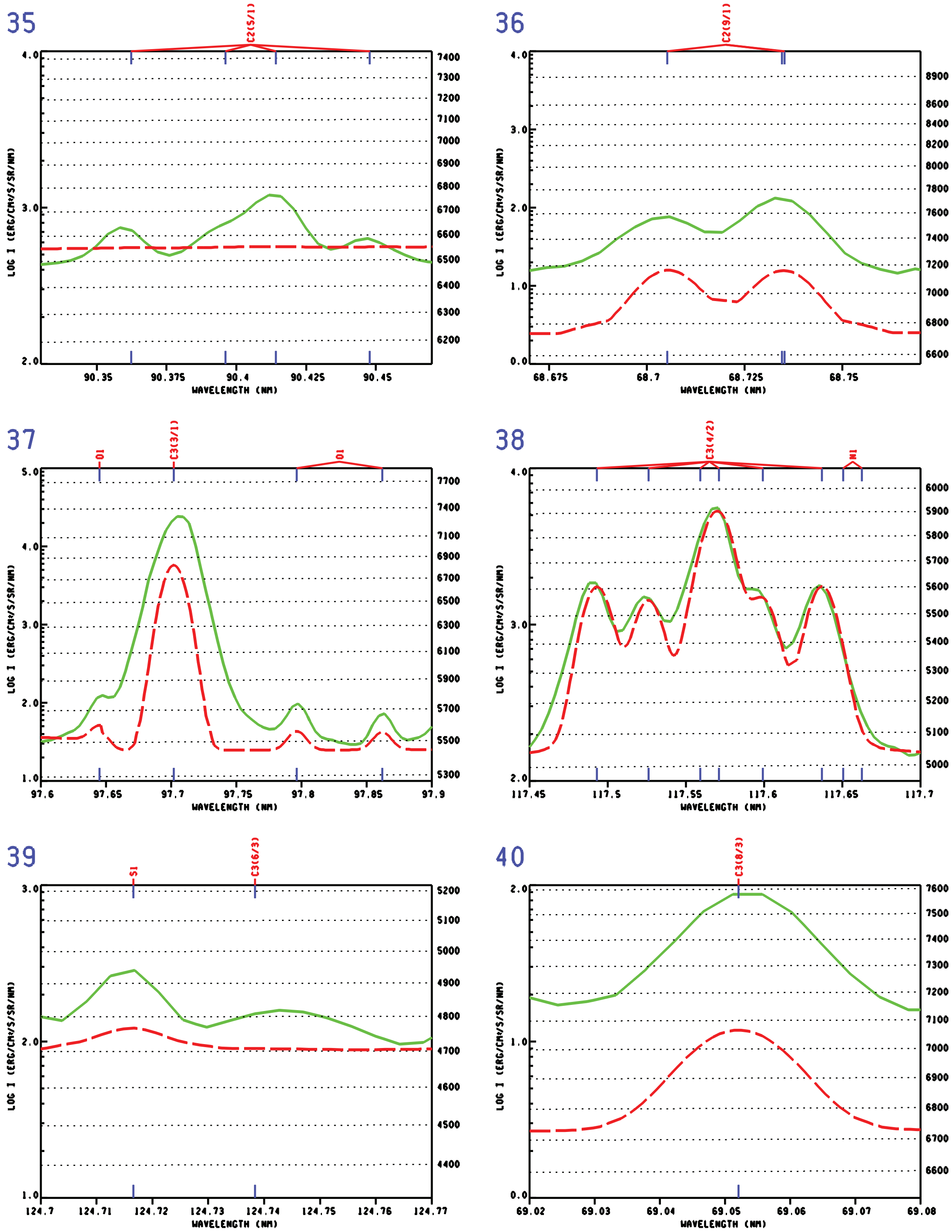

FIG. 19—*Continued*

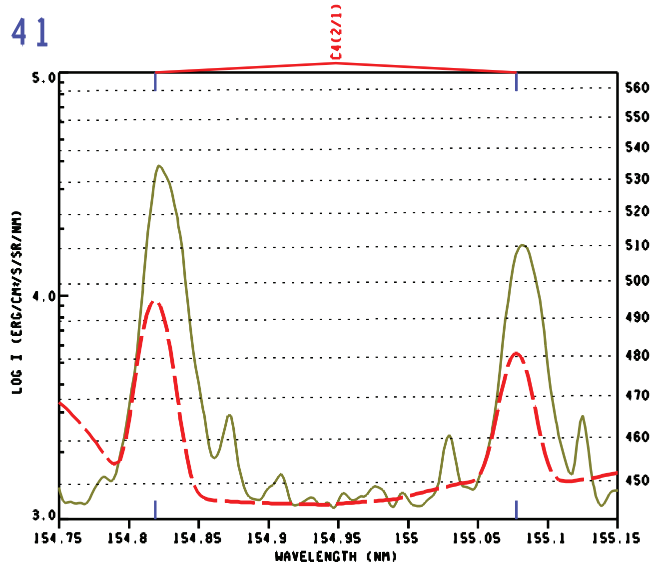

FIG. 19—*Continued*

determine electron densities from the ratios of these lines observed in solar and stellar spectra.

The 121.83 nm line is part of a multiplet that includes the much weaker forbidden line at 121.39 nm. (The upper levels of these two lines have the energies 82,079 and 82,385 cm^{-1} in Table 22.) We have not included this forbidden line since it does not appear in the SUMER spectrum of the average quiet Sun, but Pinfield et al. (1998) detected this line using SUMER observations taken with high spatial resolution. From the ratio of the two line intensities they determined an electron density of $\log n_e = 8.5 \pm 0.15$. Figure 22 indicates that there are two local maxima for the peak contribution to the central intensity of the O v 2/1 line. The one at depth 98 ($h = 1143$ km, $T = 6531$ K) appears in Table 28 and is due to the influence of the background continuum. The other local maximum (smaller than the first by the factor 0.634) occurs at depth index 28 where $T = 188{,}600$ K, and $\log n_e = 9.2$. This higher value seems inconsistent with the measurement, and we hope to resolve this problem in the future.

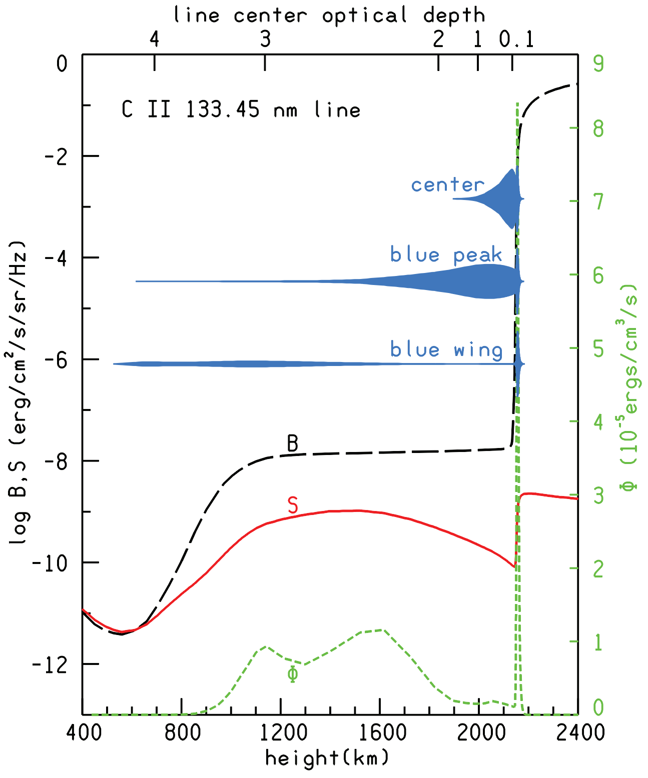

FIG. 20.—Planck function, line source function, and net radiative cooling rate for the C II 133.45 nm line vs. height, and the contribution functions dI/dh for line center, the blue peak, and the blue wing of the line.

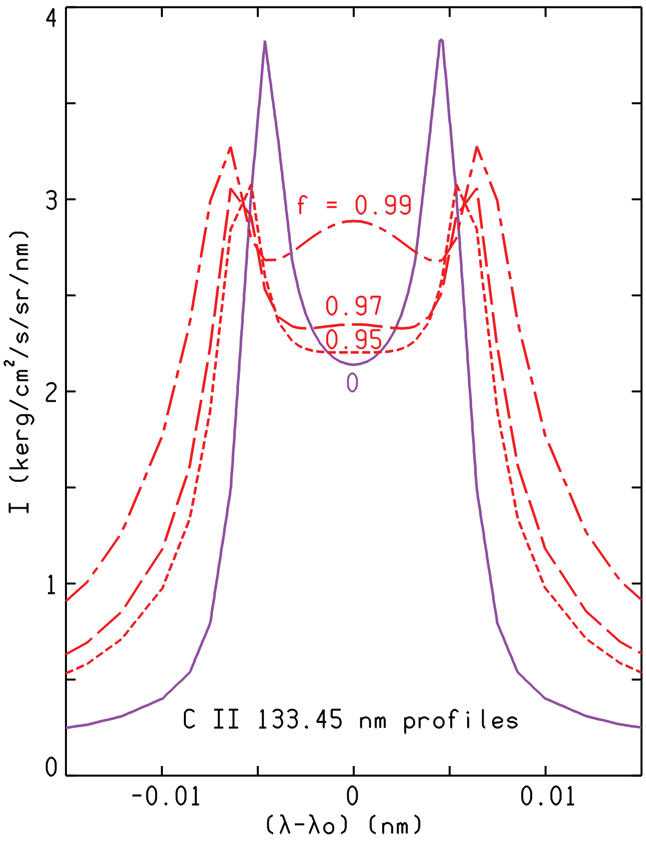

FIG. 21.—Calculated profiles of the C II 133.45 nm line at four disk positions: fractional radii $f = 0$ (*disk center*), and $f = 0.95$, 0.97, and 0.99 approaching the limb.

18.5. O VI

Vial et al. (1980) used the LPSP instrument on *OSO 8* to measure the O VI 103.19 nm resonance line at the quiet-Sun center and quiet-Sun limb and in and above an active-region prominence at the limb. Warren et al. (1997) used SUMER observations to measure Doppler wavelength shifts and nonthermal broadening in the O VI 103.19 and 103.76 nm lines and the C II lines at 103.63 and 103.70 nm. The upper limit of the broadening velocity in our Table 1 is based on their value of 34 ± 3 km s^{-1} for O VI. Warren & Winebarger (2000) present a SUMER spectroheliogram in the 103.19 line taken with high spatial resolution ($\approx 1.5''$) showing small-scale looplike structure in a quiet region near Sun center.

19. LIMITATIONS AND FURTHER NEEDED WORK

Even though this paper presents improvements over earlier chromospheric modeling, the C7 model should be viewed as an interim version rather than a definitive one. In this section we discuss various deficiencies that need further attention.

TABLE 28

O I–VI Line Formation Depths and Temperatures

Index	T (K)	Ion	Line	λ (nm)	Panel
18	324000	O VI	2/1	103.2	25
25	227800	O V	6/3	77.5	24
26	212000	O V	5/3	137.1	23
72	13200	O V	4/2	76.0	21
98	6531	O V	2/1	121.8	22
44	90640	O IV	3/1	79.0	20
47	76330	O IV	2/1	140.1	19
53	55020	O III	5/1	70.2	18
54	52690	O III	4/1	83.5	14
62	36870	O II	7/3	67.3	17
62	36870	O II	5/2	71.9	16
62	36870	O II	5/3	79.7	15
65	29500	O II	4/1	83.4	14
61	39400	O I	18/2	93.2	4
65	29500	O I	13/1	102.6	10
68	23100	O I	14/1	98.9	12
68	23100	O I	14/2	99.0	12
79	6800	O I	7/1	130.2	11
83	6706	O I	7/2	130.5	11
89	6667	O I	7/3	130.6	11
90	6660	O I	13/2	102.7	10
90	6660	O I	15/1	97.6	5
91	6652	O I	14/3	99.1	12
91	6652	O I	11/1	103.9	8
91	6652	O I	15/2	97.3	5
91	6652	O I	16/1	95.1	7
92	6643	O I	11/2	104.1	8
92	6643	O I	13/3	102.8	10
92	6643	O I	17/1	93.7	6
92	6643	O I	17/2	93.9	6
92	6643	O I	15/3	97.4	5
92	6643	O I	15/4	115.2	9
93	6633	O I	19/4	99.9	13
93	6633	O I	18/1	93.0	4
93	6633	O I	11/3	104.2	8
93	6633	O I	20/4	92.2	4
93	6633	O I	16/2	95.2	7
93	6633	O I	16/3	95.3	7
94	6623	O I	18/3	93.1	4
94	6623	O I	17/3	93.9	6
100	6400	O I	6/1	135.6	3
100	6400	O I	6/2	135.9	2
115	4485	O I	7/4	164.0	1

Note—Depth index and temperature at the height of the maximum line-center contribution to the strongest line component (or to the strongest component not obscured by blending), and the wavelength of this component, and the panel number in Fig. 23, where the calculated and observed profiles are compared. The contribution plots in Fig. 22 are in the order listed above.

19.1. *Modeling Limitations*

The modeling carried out here consists of two relatively distinct parts. The first involves the lower chromosphere up to the heights where the 110 nm C I continuum is formed. The second involves the top of the chromosphere and the onset of the transition region. The overall temperature distribution that we derive from a fit to the observations depends on the chosen turbulent pressure distribution, which we attempt to determine by comparing calculated and observed Doppler line widths, but these calculated widths depend in turn on the model temperature distribution. The iterations that this determination requires converge without difficulty, but the velocity distribution is very approximate because we are not comparing with high spatial resolution observations. These exist, and their use should improve the results reported here.

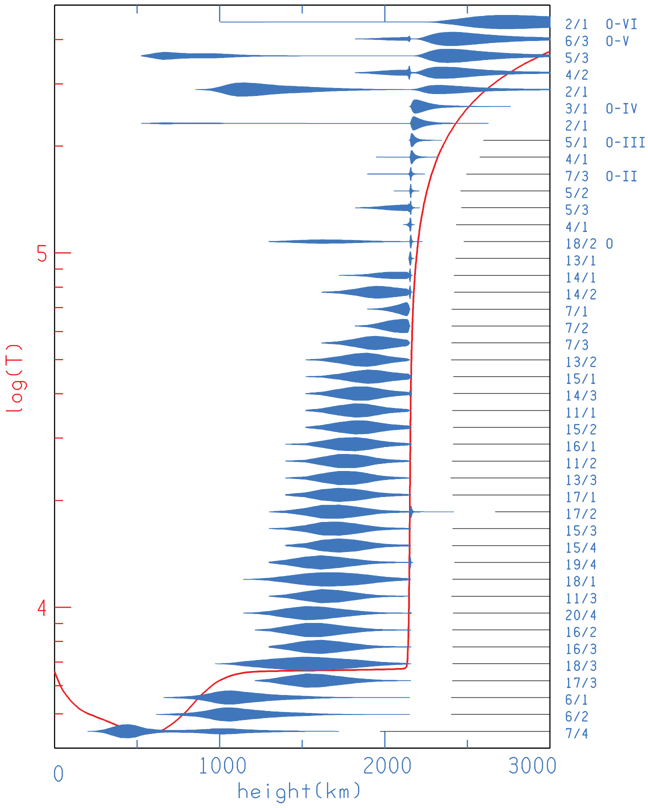

Fig. 22.—Line-center contribution functions dI/dh for the lines of O I–VI listed in Table 28. As noted for C I–IV in Fig. 18 these functions include continuum as well as line contributions.

The lower-chromosphere temperature distribution normally can be determined by increases or decreases at particular depths needed to cause the calculated intensities formed at those depths to match observations as well as possible. The temperature distribution at the top of the chromosphere and onset of the transition region is more complicated to obtain since the hydrogen Lyman line and continuum optical depths are temperature sensitive. We have chosen to work with height as the independent variable, which, in this second case, presents some difficulties since changing the turbulent pressure velocity or the temperature in the low chromosphere causes a change in the gradient of the total density, requiring the transition region to be repositioned in height in order to keep the transition-region emission the same. Increases in either the temperature or the turbulent pressure velocity in the low chromosphere can cause excessive emission from the transition region (directed inward as well as outward), leading to overionization of hydrogen in the upper chromosphere. A better choice in the modeling is to use column mass or optical depth at the head of the Lyman continuum as the independent variable in place of height.

A larger issue in semiempirical modeling is whether a turbulent pressure velocity distribution, derived from nonthermal velocities, is the most appropriate function to use in the pressure-balance equation or whether other forces need to be included (as well, or instead), as suggested by Fontenla et al. (2007).

As discussed in § 12 and shown in Figure 1, our model C7 calculations do not adequately match the observed slope of the hydrogen Lyman continuum. Further work is needed to solve this problem.

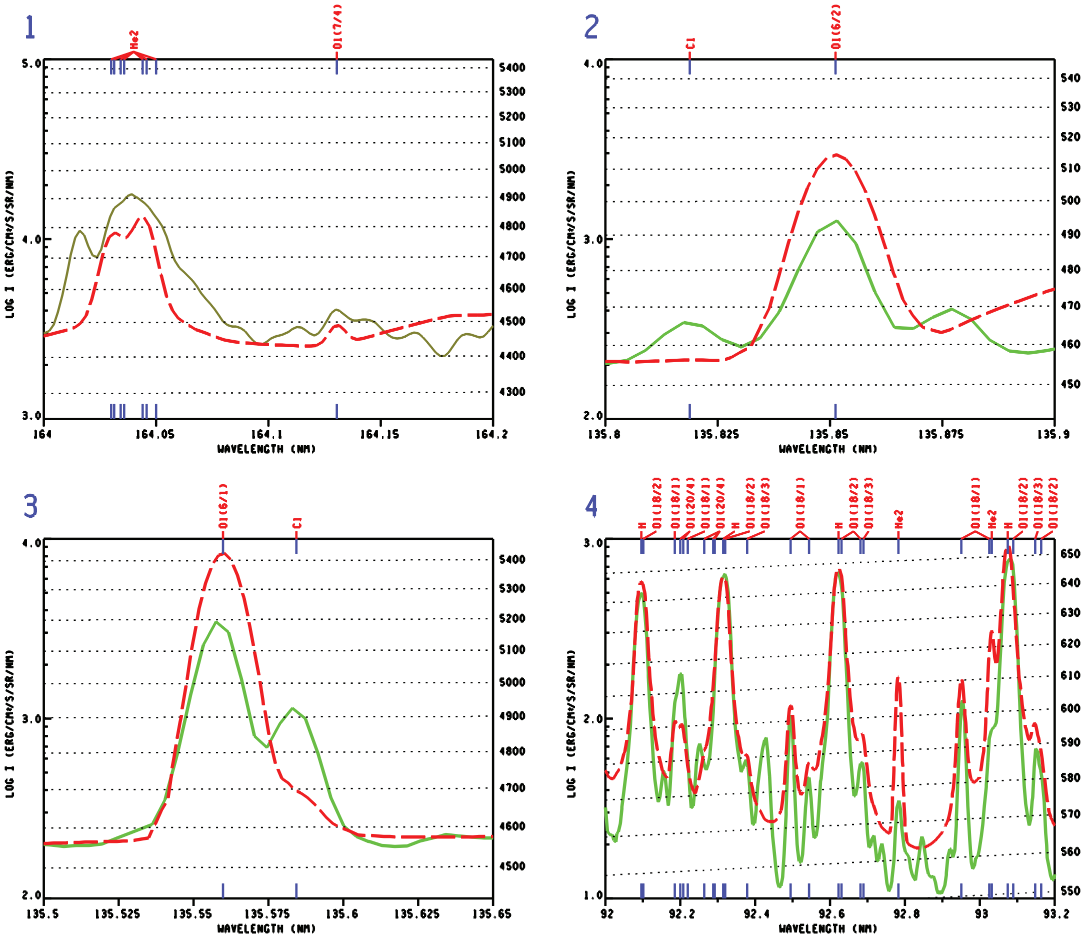

FIG. 23.—Calculated and observed profiles of the lines of O I–VI in the SUMER wavelength range, ordered by panel numbers *b* in Table 28.

We have attempted in this paper to see how well a single model can account for the average quiet-Sun spectrum, despite the differences between internetwork and network regions that could be modeled separately, particularly for a better understanding of nonthermal velocities.

We have ignored time-dependent effects (and magnetic fields) despite the extensive recent published research on dynamical models.

19.2. *General Non-LTE Line Calculations*

As discussed in § 7, we have adopted the view that for the purpose of computing photoionization rates, all lines in the spectrum should be taken into account, using rough non-LTE approximations when necessary, rather than ignoring lines that cannot be properly calculated. This applies (1) to the large numbers of UV absorption lines whose central intensities are formed at chromospheric heights and would show central emission in LTE, contrary to observations, and (2) to the large number of coronal emission lines at short wavelengths (e.g., <50.4 nm) that influence the ionization of helium and other elements, which in turn affect the spectrum in the SUMER wavelength range (e.g., the influence of He II on O III discussed in §§ 8 and 18.3). The uncertain non-LTE effects in the UV lines lead to uncertainties in the departures from LTE in the lowest levels of Si I. Thus, the 4400 K observed minimum brightness temperatuere near 160 nm may or may not represent the average minimum kinetic temperature. As noted earlier, temperature fluctuations should cause the observed 160 nm minimum temperature to be higher than the submillimeter value, due to the nonlinear dependence of the intensity on temperature at 160 nm versus the linear dependence at submillimeter wavelengths. These problems have not been adequately resolved.

19.3. *Rates and Cross Sections*

In attempting to construct a model based on the EUV continuum and lines of H, C I–IV, and O I–VI, we have used many simplifying approximations instead of undertaking a detailed study of all available data affecting the calculation of each of these 11 atoms and ions. Hence, our results should be regarded as an overview that needs to be followed by detailed studies. Figures 19 and 23 show cases in which our calculate lines have essentially no emission, contrary to observations. We have made only a few attempts (e.g., Fig. 25) to study the effects of using the alternative rates and cross sections that have been published. Further work is clearly needed.

The SUMER atlas includes emission lines of H, He I–II, C I–IV, N I–V, O I–VI, Ne I, IV–VIII, Na V, VII–IX, Mg II, V–X, Al IV, VII–X, Si I–V, VII–IX, XI, P V, S I–VI, IX–XI, Cl I, VI, VII, Ar I, V–VIII, K XII, XIII, Ca II, V–X, Mn VII, Fe II, III, VII–XII, and Ni II. From this list, we have calculated line profiles for He I–II, N I–IV, Ne I–VIII, Mg II, Si I–IV, S I–IV, and Ca II in addition to H, C I–IV, and O I–VI (see Avrett et al. 2006 for our S I results). We hope to refine the model C7 calculation by including further atoms and ions and comparing these additional results with observations.

20. CONCLUSIONS

It should be noted that our results have been discussed throughout this paper, particularly in §§ 2, 15, 16, and 18. Here we add only some concluding remarks.

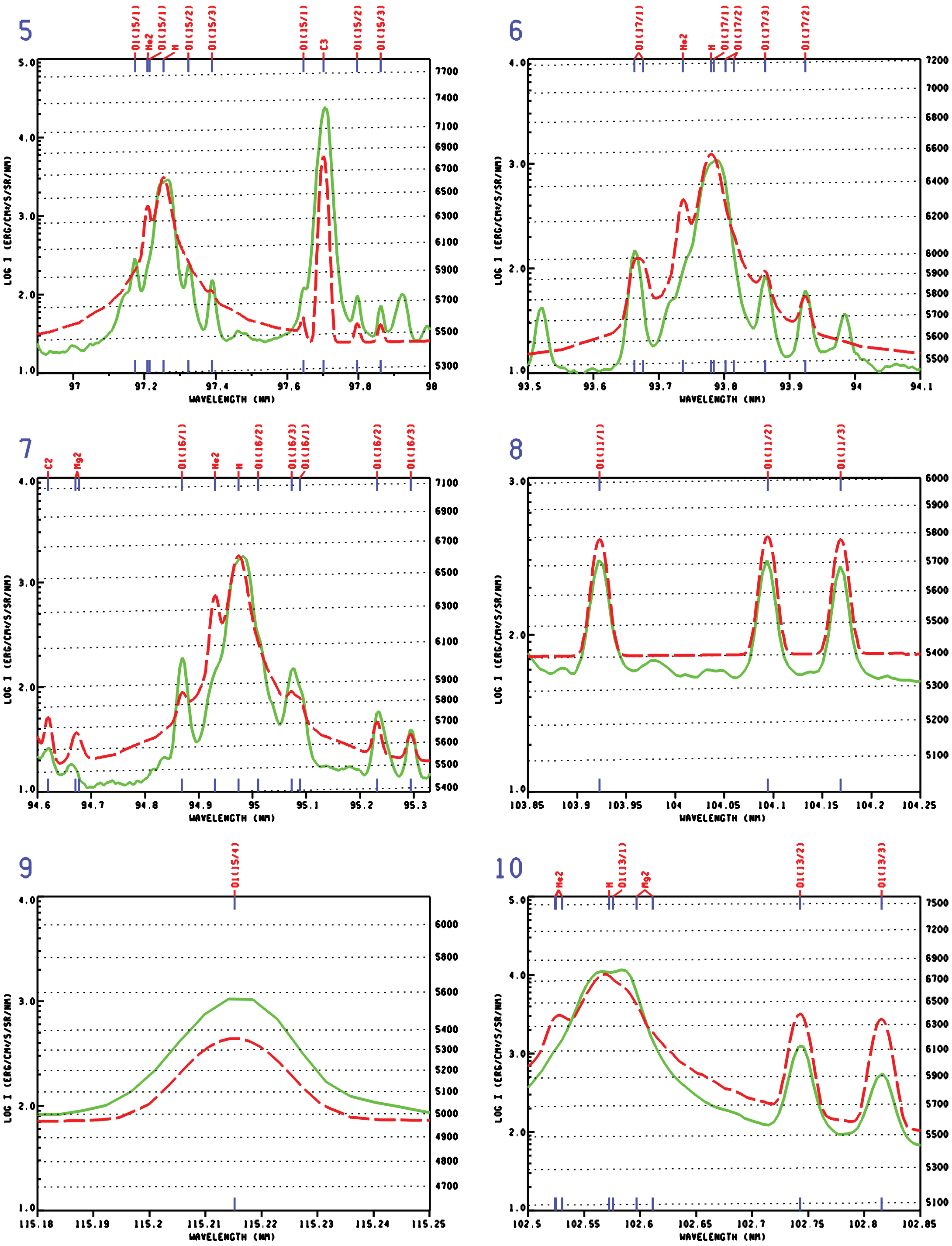

FIG. 23—*Continued*

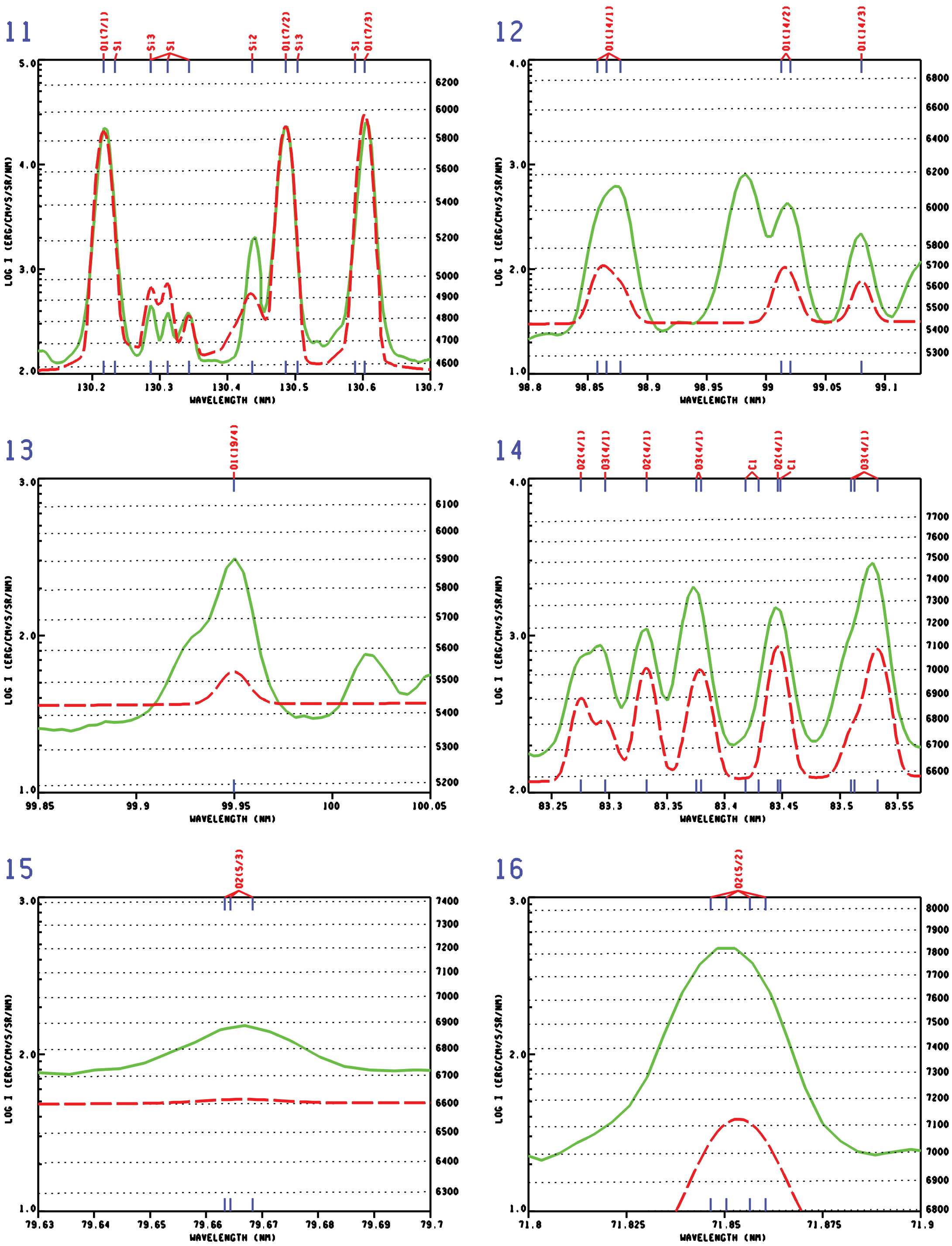

FIG. 23—*Continued*

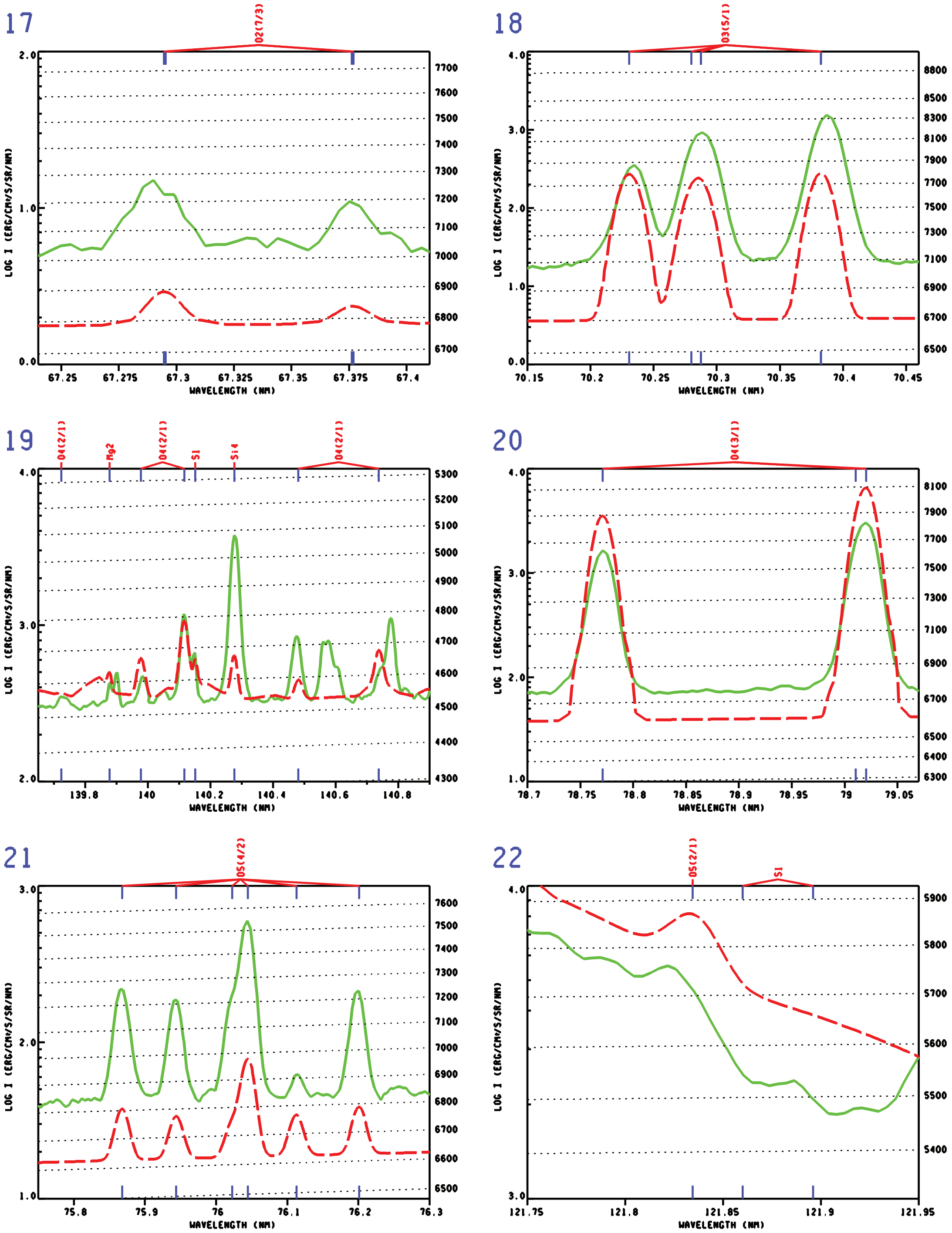

FIG. 23—*Continued*

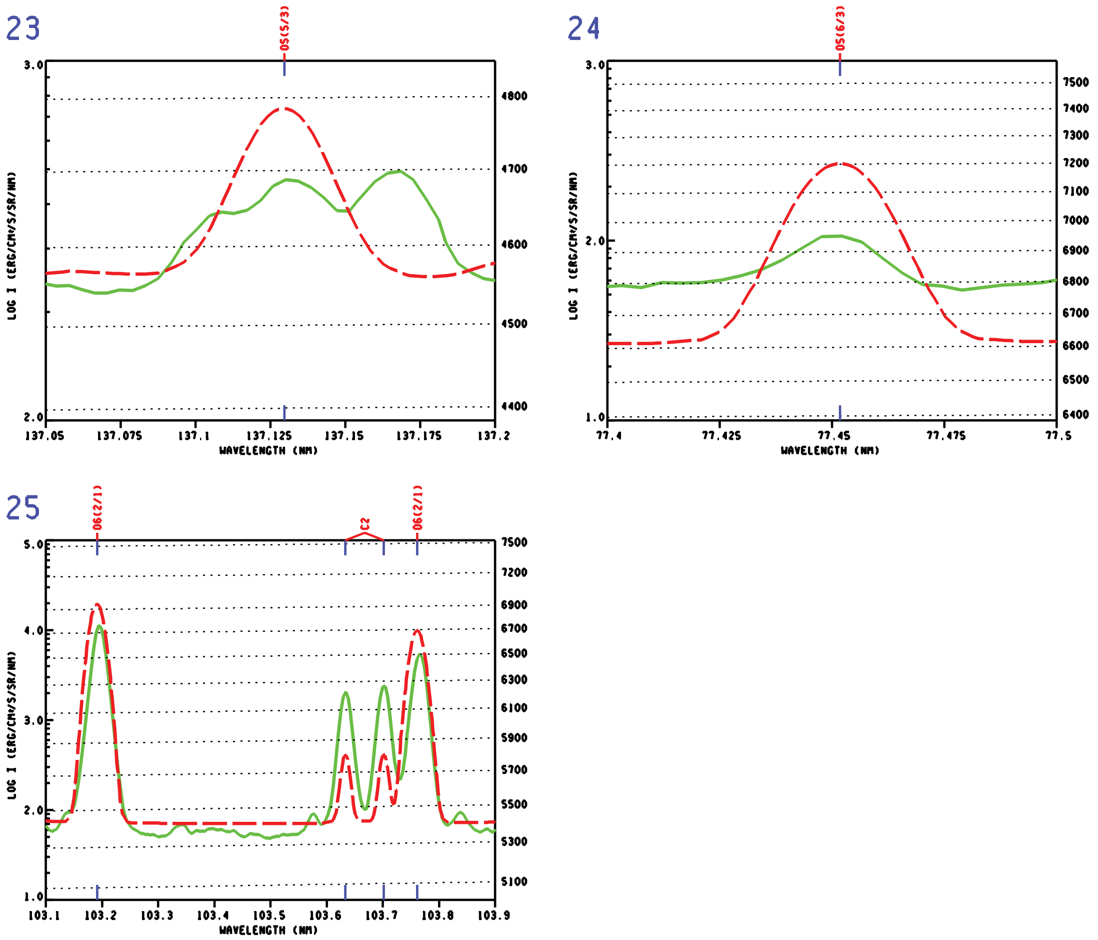

FIG. 23—*Continued*

TABLE 29

LINE TRANSITIONS BETWEEN 92.0 AND 93.2 nm

λ (nm)	O I	H	He II
92.096..................		10/1	
92.102..................	18/2		
92.186..................	18/1		
92.201..................	20/4		
92.208..................	20/4		
92.220..................	18/1		
92.264..................	20/4		
92.289..................	20/4		
92.293..................	20/4		
92.315..................		9/1	
92.321..................	18/2		
92.379..................	18/3		
92.495..................	18/1		
92.544..................	18/1		
92.623..................		8/1	
92.631..................	18/2		
92.682..................	18/2		
92.690..................	18/3		
92.782..................			15/2
92.951..................	18/1		
93.025..................	18/1		
93.031..................			14/2
93.075..................		7/1	
93.090..................	18/2		
93.148..................	18/3		
93.164..................	18/2		

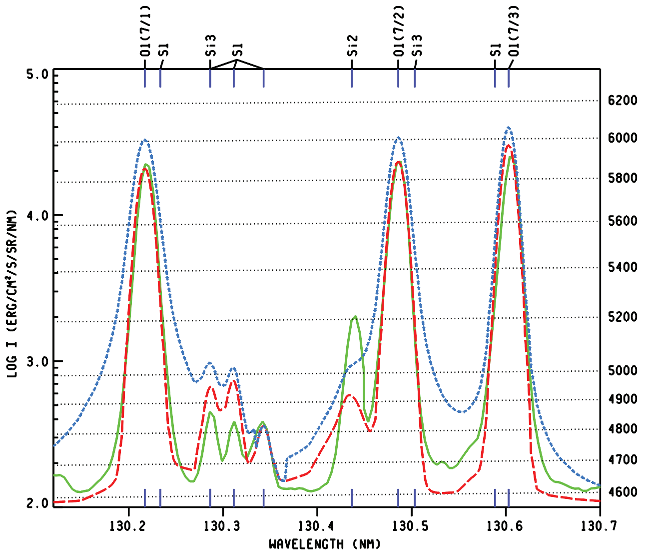

FIG. 24.—Convolved oxygen triplet lines computed with CRD (*short-dashed blue line*) and with PRD (*red long-dashed line*), compared with the SUMER profiles (*green solid line*).

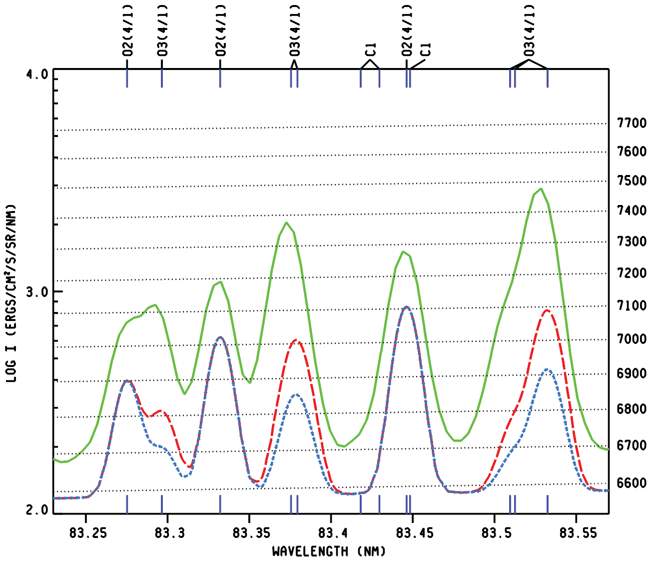

FIG. 25.—Same as panel 14 of Fig. 23 but with the additional profiles (*blue short-dashed line*) showing the results based on the CHIANTI collision strengths for O III vs. those based on the Aggarwal & Keenan (1999) values.

Computing a detailed spectrum from a specified set of atmospheric parameters, including realistic treatments of physical processes, is a difficult task, but one of general importance in astrophysics. Only limited information can be obtained from observed spectra without carrying out spectrum synthesis calculations for comparison with the observations. This paper gives the results of calculations that are compared with the observed solar extreme-ultraviolet spectrum. The calculations are more extensive than in previous papers, but only generally match the observations. The atmospheric specifications consist principally of the temperature as a function of height, and the calculations produce highly detailed spectra that can be compared with the observations. Many physical processes, and many uncertain rates and cross sections, are involved in the calculations. In the present application we find a temperature distribution from our attempt to obtain a best fit to the observations, thus determining a semiempirical model. Other physical constraints can be added to determine a theoretical model, but similar computational procedures would be involved in calculating the spectrum from given atmospheric parameters. The calculations here are one-dimensional and time-independent, as well as semiempirical, but spectrum calculations at least as detailed as those shown here are required in dynamical and multidimensional applications as well.

We derive in this paper an atmospheric model for the solar chromosphere and transition region broadly consistent with the spatially and temporally averaged spectrum of the quiet Sun in the extreme ultraviolet. We have made many approximations, and there are many uncertainties in the rates and cross sections used in the calculations, but the differences between the calculated and observed results seem within the bounds of these approximations and uncertainties, so that we seem to have determined a reasonable atmospheric model for the average quiet Sun. Given the inhomogeneous structures observed in various lines at the solar limb, it is perhaps surprising that a one-dimensional model can give rough agreement with disk-center profiles of lines formed throughout the chromosphere and up to temperatures of order 300,000 K in the transition region. Perhaps this result indicates that the spectrum along the vertical line of sight gives information about the basic stratification of the atmosphere and is relatively independent of small-scale filamentary and loop structures.

We have used observations of the quiet Sun at disk center, but we could have obtained a similar model from observations of the full disk at the same spectral resolution at times of minimum activity (since limb structures have little influence on the flux from the full disk). Thus, we have essentially modeled the solar spectrum as if it were the spectrum from a star or other unresolved astronomical source. See Mauas (2007) for a review of semiempirical modeling of stellar chromospheres.

The solar atmosphere has both spatial structure and temporal variations. The intensity differences between network and internetwork regions of the quiet Sun are equivalent to brightness temperature differences of a few hundred K. Similar variations of brightness temperature with time are observed at high spatial resolution in these two regions. While time-dependent modeling is of great interest in understanding the basic physics of the atmosphere, time-independent modeling may adequately describe many general properties of the atmosphere.

The methods described here can be used to obtain separate models for typical network and internetwork regions, based on detailed SUMER spectra of these regions. Such observations have recently been obtained (W. Curdt 2007, private communication). Detailed modeling of active regions should be carried out as well. The spectra from specific regions of the internetwork and network will not have the line broadening produced by spatial averaging and will provide better turbulent velocity data, perhaps helping to discriminate between different atmospheric heating mechanisms.

Having reliable models of the different quiet and active components of the solar atmosphere would allow us to calculate the solar flux at any wavelength, line or continuum, at high spectral resolution, based on the pattern of activity on the solar disk observed at any time. Such calculated spectral irradiances would be highly useful in studies of how solar radiation affects the Earth's upper atmosphere, particularly at short wavelengths.

With improved rates and cross sections, and a better treatment of lines in the photoionization integrals, we should be able to use the solar EUV spectrum for detailed abundance determinations. Przybilla et al. (2003) give an overview of CNO atomic model data for quantitative spectroscopy and abundance determinations.

How important are the temporal variations at given locations? The average quiet-Sun model presented here is based on observations that represent averages of internetwork and network regions, but the observed temporal variations are rather small: in general, the brightness temperature variations observed at high spatial resolution, away from active regions, do not exceed a few hundred degrees. They do not have the thousand-degree variations of the shock-wave models published to date. Some physical effects such as recombination times longer than dynamical fluctuation times may cause the observed brightness temperatures to vary less than the kinetic temperatures. Such effects have been studied for hydrogen by Carlsson & Stein (2002) and by Leenaarts & Wedemeyer-Böhm (2006). See Judge (2005) for a study of the time dependence of atomic level populations in evolving plasmas, and Gnat & Sternberg (2007) for a general study of time-dependent ionization in radiatively cooling gas.

The simplest view is that the kinetic temperature variations in the atmosphere are not much greater than the brightness temperature variations determined from observations. This is contrary to the view expressed, e.g., by Wedemeyer et al. (2004) that chromospheric emission lines do not necessarily imply an outward increase in average temperature, but can be explained by the presence of substantial spatial and temporal temperature inhomogenities. But Occam's razor might be applicable: simple explanations are more likely to be correct than complicated ones.

Carlsson (2007) asks the relevant question: "Is the internetwork chromosphere wholly dynamic in nature or are the dynamic variations only minor perturbations on a semi-static state similar to the state in semi-empirical models (e.g., Kalkofen et al. 1999)?"

There is considerable interest in dynamical modeling as a way to understand how the chromosphere is heated, but it is reasonable to require of such modeling that (1) the predicted intensity fluctuations should not greatly exceed observed values and (2) the spectrum calculated from the model should generally agree with observed spectrum, not just from limited regions, but from the solar atmosphere as a whole.

Final note.—The computer input and output files that produced the results reported here may be obtained from the first author. The Pandora computer program is available from the website http://www.cfa.harvard.edu/~avrett. The second author has retired and is no longer available for assistance.

We thank Philip Judge (the referee), Juan Fontenla, Petr Heinzel, and Werner Curdt for many helpful comments on this paper.

APPENDIX

Here we summarize the equations we use to include partial frequency redistribution (PRD) in our calculations of the hydrogen Lyα and Lyβ lines and other strong resonance lines. Also, we summarize the basic method we use to construct linear equations to solve the coupled equations of radiative transfer and statistical equilibrium.

When complete frequency redistribution (CRD) can be assumed, the radiative transfer equation for the $j > i$ line transition, in terms of the Einstein *A*- and *B*-coefficients, is

$$\frac{dI_\nu}{ds} = \frac{h\nu}{4\pi}\phi_\nu[-(n_iB_{ij} - n_jB_{ji})I_\nu + n_jA_{ji}]. \tag{A1}$$

Other sources of absorption and emission are ignored here for simplicity but are included later. In this equation s represents length in the direction of the intensity I_ν and ϕ_ν is the line absorption profile function, normalized so that

$$\int \phi_{\nu'}d\nu' = 1. \tag{A2}$$

To include PRD we adopt the corresponding equation from Hubeny (1985):

$$\frac{dI_\nu}{ds} = \frac{h\nu}{4\pi}\phi_\nu[-(n_iB_{ij} - \rho_\nu n_jB_{ji})I_\nu + n_jA_{ji} + n_iB_{ij}(\overline{R}_\nu - \overline{J})]. \tag{A3}$$

According to Oxenius (1965) and Hubeny & Lites (1995) the stimulated emission term n_jB_{ji} (which is often negligible) is multiplied by $\rho_\nu = \psi_\nu/\phi_\nu$, the ratio of the emission and absorption profile functions. We will specify ρ_ν later in this derivation.

The final part of equation (A3) includes the integrated mean intensity,

$$\overline{J} = \int \phi_{\nu'}J_{\nu'}d\nu', \tag{A4}$$

and the redistributed mean intensity,

$$\overline{R}_\nu = \frac{1}{\phi_\nu}\int R_{\nu',\nu}J_{\nu'}d\nu', \tag{A5}$$

where J_ν is the mean intensity, or the angular-average of the intensity I_ν.

In equation (A3) we do not include the cross-redistribution term discussed in detail by Hubeny & Lites. See also Uitenbroek (2001). Hubeny & Lites show that cross redistribution involving the hydrogen Hα line has an effect on the Lyβ profile, but only in the wings where the Lyβ intensity is a factor of 10 smaller than the central values and where there are comparable uncertainties in line-broadening parameters and other opacities. Our main concern is to account for the width of the Lyβ line core as well as the overall intensity and for simplicity we ignore cross redistribution.

The redistribution function $R_{\nu',\nu}$ in equation (A5) is approximated as

$$R_{\nu',\nu} = \Gamma R^{\rm II}_{\nu',\nu} + (1 - \Gamma)\phi_{\nu'}\phi_\nu, \tag{A6}$$

where $R^{\rm II}_{\nu',\nu}$ is the redistribution function describing coherent scattering in the atom's rest frame (Hummer 1962) and Γ is the coherence fraction (see Yelnik et al. 1981; Heinzel & Hubeny 1985; Cooper et al. 1989) given by

$$\Gamma_{ji} = \frac{\delta'_R}{\delta_R + \delta_{\rm Stark} + \delta_{\rm vdW} + \delta_{\rm res}}, \tag{A7}$$

where the denominator is the total damping parameter for the line, and where $\delta_R = \sum_{l<j} A_{jl}/4\pi$ is the radiative damping parameter and $\delta_R' = A_{ji}/4\pi$ (i.e., δ_R' includes only A_{ji}). Thus, equation (A7) becomes

$$\Gamma_{ji} = \frac{A_{ji}}{\sum_{l<j} A_{jl} + d_{ji}}. \tag{A8}$$

where d_{ji} is 4π times the sum of the Stark, van der Waals, and resonance damping parameters.

Sublevels and explicit radiative transitions need to be taken into account, so that for the hydrogen Lyα line,

$$\Gamma(\mathrm{Ly}\alpha) = \frac{A_{2p1s}}{A_{2p1s} + d_{21}}, \tag{A9}$$

where $A_{2p1s}(= 6.265 \times 10^8\ \mathrm{s}^{-1})$ is used for the $2p$ to $1s$ transition, rather than $A_{21}(= 4.699 \times 10^8\ \mathrm{s}^{-1})$ for the combined sublevels. For the Lyβ line, the corresponding equation is

$$\Gamma(\mathrm{Ly}\beta) = \frac{A_{3p1s}}{A_{3p1s} + A_{3p2s} + d_{31}}. \tag{A10}$$

It should be noted that, due to Stark broadening, d_{21} and d_{31} have a slight dependence on frequency, which we neglect here for simplicity.

Substituting $R_{\nu',\nu}$ from equation (A6) into equation (A5) gives the following equation for the term $\overline{R}_\nu - \overline{J}$ in equation (A3):

$$\overline{R}_\nu - \overline{J} = \Gamma(R_\nu^{\mathrm{II}} - \overline{J}), \tag{A11}$$

where

$$R_\nu^{\mathrm{II}} = \frac{1}{\phi_\nu} \int R_{\nu',\nu}^{\mathrm{II}} J_{\nu'} d\nu'. \tag{A12}$$

The $R_{\nu',\nu}^{\mathrm{II}}$ function has the normalization $\int R_{\nu',\nu}^{\mathrm{II}} d\nu' = \phi_\nu$. In the line wings, $R_\nu^{\mathrm{II}} \approx J_\nu$, since $R_{\nu',\nu}^{\mathrm{II}}$ has a maximum at $\nu' = \nu$ and $J_{\nu'}$ varies gradually with ν'. We evaluate the function $R_{\nu',\nu}^{\mathrm{II}}$ using the approximate method of Gouttebroze (1986). See also Uitenbroek (2001). We have compared these results with the more accurate numerical evaluation of Adams et al. (1971) and have found that the Gouttebroze approximation is generally adequate for the purposes of the calculations presented here.

We then write the radiative transfer equation (A3) as

$$\frac{dI_\nu}{ds} = -\kappa_\nu^L (I_\nu - S_\nu^L), \tag{A13}$$

where the line absorption coefficient is given by

$$\kappa_\nu^L = \frac{h\nu}{4\pi} \phi_\nu (n_i B_{ij} - \rho_\nu n_j B_{ji}) \tag{A14}$$

and the line source function is

$$S_\nu^L = \frac{(n_j A_{ji}/n_i B_{ij}) + \Gamma(R_\nu^{\mathrm{II}} - \overline{J})}{1 - \rho_\nu (n_j B_{ji}/n_i B_{ij})}. \tag{A15}$$

In the case of CRD for which $\rho_\nu = 1$ and $\Gamma = 0$, this expression reduces to

$$S_\nu^L = \frac{2h\nu^3/c^2}{(n_i g_j/n_j g_i) - 1}, \tag{A16}$$

where g_j and g_i are the statistical weights of the two levels.

We now use the statistical equilibrium equations to express n_j/n_i in equation (A15) in terms of $\overline{J}$ for this line transition. The statistical equilibrium equation for level j can be expressed in the form

$$n_j(A_{ji} + B_{ji}\overline{J} + X) = n_i(B_{ij}\overline{J} + Y), \tag{A17}$$

where the X and Y terms include the effects of all collisional and other radiative transitions from level j to level i (directly or through other levels or continua). In the simplest case of a two-level atom with no continuum, $X = C_{ji}$ and $Y = C_{ij}$, where C_{ij} and C_{ji} are the collisional excitation and de-excitation rates. In general, $X = \sum_l R_{jl}$ and $Y = \sum_l (n_l/n_i) R_{lj}$ where R_{nm} represents each transition rate from n to m except for the radiative rates from j to i and from i to j that appear in equation (A17).

From equation (A17) we can write

$$\frac{n_j}{n_i}\frac{A_{ji}}{B_{ij}} = \frac{\overline{J} + \epsilon_2 B'}{1 + \epsilon_1 + \mathcal{J}}, \tag{A18}$$

where $\mathcal{J} = \overline{J}/\alpha$, $B' = \alpha\beta$, $\alpha = 2h\nu^3/c^2$, $\beta = \exp(-h\nu/kT)$, $\epsilon_1 = X/A_{ji}$, and $\epsilon_2 = (Y/A_{ji})(g_i/\beta g_j)$. Note that $g_i/\beta g_j = C_{ji}/C_{ij}$ and that B' is the Planck function when stimulated emission is negligible. Substituting this result into equation (A15) gives

$$S_\nu^L = \frac{\overline{J} + \epsilon_2 B' + \Gamma(R_\nu^{\rm II} - \overline{J})(1 + \epsilon_1 + \mathcal{J})}{1 + \epsilon_1 - \beta\epsilon_2 + (1 - \rho_\nu)(\mathcal{J} + \beta\epsilon_2)}, \tag{A19}$$

which expresses S_ν^L in terms of $\overline{J}$ and of other quantities that are either known or which can be treated iteratively.

For $\rho_\nu = 1$ and $\Gamma = 0$ in the case of CRD, this equation reduces to

$$S^L = \frac{\overline{J} + \epsilon_2 B'}{1 + \epsilon_1 - \beta\epsilon_2} \tag{A20}$$

or to

$$S^L = \frac{\overline{J} + \epsilon B^S}{1 + \epsilon}, \tag{A21}$$

where

$$\epsilon = \epsilon_1 - \beta\epsilon_2 \tag{A22}$$

and

$$B^S = (\epsilon_2/\epsilon)B'. \tag{A23}$$

In the two-level case, $\epsilon_1 = \epsilon_2 = C_{21}/A_{21}$, $\epsilon = (1 - \beta)C_{21}/A_{21}$, and $B^S = B_\nu$, the Planck function at the line frequency ν.

Equations (A21)–(A23) define the functions S^L, ϵ, and B^S in general. We call S_ν^L the frequency-dependent line source function and S^L the frequency-independent component line source function. In general,

$$S^L = \frac{2h\nu^3/c^2}{(n_i g_j/n_j g_i) - 1}, \tag{A24}$$

whereas, from equation (A16), $S_\nu^L = S^L$ only for CRD.

Equation (A19) may be written as

$$S_\nu^L = \frac{\overline{J} + \epsilon B^S + f_\nu}{1 + \epsilon_\nu}, \tag{A25}$$

where

$$f_\nu = \Gamma(R_\nu^{\rm II} - \overline{J})(1 + \epsilon_1 + \mathcal{J}) \tag{A26}$$

and

$$\epsilon_\nu = \epsilon + (1 - \rho_\nu)(\mathcal{J} + \beta\epsilon_2). \tag{A27}$$

We now obtain an expression for ρ_ν in this equation (and earlier in eq. [A3]). The emission profile ψ_ν that appears in $\rho_\nu = \psi_\nu/\phi_\nu$ is determined by the equation

$$n_j A_{ji}\psi_\nu = \phi_\nu[n_j A_{ji} + n_i B_{ij}(\overline{R}_\nu - \overline{J})]. \tag{A28}$$

See Hubeny et al. (1983). Thus,

$$\rho_\nu = 1 + \frac{n_i}{n_j}\frac{B_{ij}}{A_{ji}}\Gamma(R_\nu^{\rm II} - \overline{J}), \tag{A29}$$

so that we replace equation (A27) by

$$\epsilon_\nu = \epsilon + g_\nu, \tag{A30}$$

where

$$g_\nu = -\frac{n_i}{n_j}\frac{B_{ij}}{A_{ji}}\Gamma(R_\nu^{\rm II} - \overline{J})(\mathcal{J} + \beta\epsilon_2). \tag{A31}$$

For the purpose of solving equation (A25) for $\overline{J}$ and S_ν^L, we consider g_ν and f_ν to be given. Their dependence on $\overline{J}$, $R_\nu^{\rm II}$, and n_j/n_i is treated iteratively.

The radiative transfer equation (A13) can be used to express J_ν in terms of S_ν^L, using lambda-operator notation, as

$$J_\nu = \Lambda_\nu\{S_\nu^L\}. \tag{A32}$$

which can be written in discrete form as

$$J_{ik} = \sum_j W_{ijk}^\Lambda S_{jk}^L, \tag{A33}$$

where the i and j subscripts refer to depths and k to frequency. At any given frequency, J at each depth i depends on S^L at all depths j. The weighting coefficients W_{ijk}^Λ depend on the optical depths determined from integrals (over geometrical depths) of the sum of κ_ν^L in equation (A14) and any other absorption and scattering coefficients at line frequencies ν. Then we can write

$$\overline{J} = \int \phi_\nu \Lambda_\nu\{S_\nu^L\} d\nu. \tag{A34}$$

This formal solution of the transfer equation, expressing $\overline{J}$ in terms of S_ν^L, can be combined with equation (A25), which was derived from the statistical equilibrium equation, giving an integral equation for S_ν^L which depends on frequency as well as depth. However, it is much easier to solve an integral equation (as a set of simultaneous equations) for the frequency-independent component line source function S^L, given by equation (A21), which depends only on depth. For this purpose we write equation (A25) as

$$S_\nu^L = a_\nu S^L + b_\nu, \tag{A35}$$

where

$$a_\nu = \frac{1+\epsilon}{1+\epsilon_\nu} \tag{A36}$$

and

$$b_\nu = \frac{f_\nu}{1+\epsilon_\nu}. \tag{A37}$$

Then from equations (A21) and (A34),

$$S^L = \frac{\int \phi_\nu \Lambda_\nu\{a_\nu S^L + b_\nu\} d\nu + \epsilon B^S}{1+\epsilon}, \tag{A38}$$

providing a set of simultaneous linear equations for the values of S^L at each depth, given the functions a_ν and b_ν. From S^L, we can obtain S_ν^L from equation (A35), and then J_ν, $R_\nu^{\rm II}$, and $\overline{J}$ from equations (A32), (A12), and (A4).

We note that b_ν and to a lesser extent a_ν depend on $R_\nu^{\rm II}$ and on $\overline{J}$ and these in turn depend on J_ν. Hence we need to alternate between calculating S^L from equation (A38) at each depth, and calculating J_ν from equation (A32) at each frequency and depth, in order to obtain the functions a_ν and b_ν in equation (A35).

In this way we reduce a highly nonlinear problem to the solution of a set of linear simultaneous equations for S^L together with iterative determinations of J_ν.

Now we return to the radiative transfer equations (A3) and (A13) which included only the absorption and emission due to the given line transition. The general form of equation (A13) is

$$\frac{dI_\nu}{ds} = -\kappa_\nu^L(I_\nu - S_\nu^L) - \kappa_\nu^*(I_\nu - S_\nu^*), \tag{A39}$$

where κ_ν^* and S_ν^* represent the absorption coefficient and source function due to other lines and to various continua, including the effects of scattering. Both κ_ν^* and S_ν^* are treated as given functions in the calculation of S_ν^L. Then

$$\frac{dI_\nu}{ds} = -\kappa_\nu(I_\nu - S_\nu), \tag{A40}$$

where the total absorption coefficient is

$$\kappa_\nu = \kappa_\nu^L + \kappa_\nu^* \tag{A41}$$

and the total source function is

$$S_\nu = \frac{\kappa_\nu^L S_\nu^L + \kappa_\nu^* S_\nu^*}{\kappa_\nu^L + \kappa_\nu^*}. \tag{A42}$$

Equation (A19) for S_ν^L and equations (A20)–(A31) are unchanged, but now J_ν and $\bar{J}$ in equations (A32) and (A34) depend on S_ν rather than S_ν^L, i.e., they depend on

$$S_\nu = \frac{\kappa_\nu^L (a_\nu S^L + b_\nu) + \kappa_\nu^* S_\nu^*}{\kappa_\nu^L + \kappa_\nu^*}. \tag{A43}$$

Now we let

$$a'_\nu = \frac{\kappa_\nu^L a_\nu}{\kappa_\nu^L + \kappa_\nu^*} \tag{A44}$$

and

$$b'_\nu = \frac{\kappa_\nu^L b_\nu + \kappa_\nu^* S_\nu^*}{\kappa_\nu^L + \kappa_\nu^*}, \tag{A45}$$

so that S^L is given by equation (A38) with a_ν and b_ν replaced by a'_ν and b'_ν, respectively. In this way we have included the effects of other lines and continuum processes in the radiative transfer equation. From S^L we obtain S_ν and then obtain the mean intensity from

$$J_\nu = \Lambda_\nu \{S_\nu\}, \tag{A46}$$

instead of from equation (A32), in order to redetermine a'_ν and b'_ν.

After S^L is calculated for a given $j > i$ line transition, the number density ratio n_j/n_i is determined from equation (A24).

Only a given $j > i$ transition is discussed above. In the case of a multilevel atom, each radiative transition can be solved in this way, given the X and Y coupling terms in the statistical equilibrium equation (A17). This is the so-called equivalent-two-level-atom approach for solving multilevel problems. Iterations are required to correctly determine these coupling terms.

Another basic method of solution consists of simply iterating between equations (A25) and (A34) for S_ν^L and $\bar{J}$, instead of combining these equations as described above. This approach ordinarily converges very slowly. The ALI, or accelerated-lambda-iteration, method avoids slow convergence by analytically combining the diagonal part of the lambda operator with other terms; this is referred to as a preconditioning of the lambda operator. In addition, direct acceleration of the solution is often necessary. An advantage the ALI method in multilevel problems is that it can be applied to the set of statistical equilibrium equations (A17), with $\bar{J}$ for each j to i transition expressed in terms of n_j/n_i. See Hubeny (2003) for a comprehensive review.

A disadvantage of the ALI method is that in the case of strong line transitions, convergence cannot always be obtained in a reasonable number of iterations. An example is given by Avrett (2007b) of a simple problem that cannot readily be solved by the ALI method. That paper discusses a hybrid method in which preconditioned lambda iterations are used for the relatively weak radiative transitions, and the above simultaneous equations are solved for strong transitions, such as the hydrogen Lyα and Lyβ lines. Such a hybrid method is used to obtain the results given in this paper. A similar hybrid method is described by Hubeny & Lanz (2003) with the strong lines treated by a linearized combination of equations (A25) and (A34) and weak lines treated by the ALI method.

REFERENCES

Adams, T. G., Hummer, D. G., & Rybicki, G. B. 1971, J. Quant. Spectrosc. Radiat. Transfer, 11, 1365

Aggarwal, K. M., Berrington, K. A., Burke, P. G., Kingston, A. E., & Pathak, A. 1991, J. Phys. B, 24, 1385

Aggarwal, K. M., & Keenan, F. P. 1999, ApJS, 123, 311

Aguilar, A., et al. 2003, ApJS, 146, 467

Akiyama, S., Doschek, G. A., & Mariska, J. T. 2005, ApJ, 623, 540

Anderson, L. S. 1989, ApJ, 339, 558

Anderson, L. S., & Athay, R. G. 1989a, ApJ, 336, 1089

———.1989b, ApJ, 346, 1010

Arnaud, M., & Rothenflug, R. 1985, A&AS, 60, 425

Artzner, G., et al. 1997, Space Sci. Instrum., 3, 131

Asensio Ramos, A., Trujillo Bueno, J., Carlsson, M., & Cernicharo, J. 2003, ApJ, 588, 61

Asplund, M. 2005, ARA&A, 43, 481

Asplund, M., Grevesse, N., & Sauval, A. J. 2005, in ASP Conf. Ser. 336, Cosmic Abundances as Records of Stellar Evolution and Nucleosynthesis, ed. T. G. Barnes & F. N. Bash (San Francisco: ASP), 25

Asplund, M., Grevesse, N., Sauval, A. J., Allende Prieto, C., & Blomme, R. 2005, A&A, 431, 693

Asplund, M., Grevesse, N., Sauval, A. J., Allende Prieto, C., & Kiselman, D. 2004, A&A, 417, 751

Athay, R. G. 1976, The Solar Chromosphere and Corona: Quiet Sun (Dordrecht: Reidel)

Avrett, E. H. 1985, in Chromospheric Diagnostics and Modelling, ed. B. W. Lites (Sunspot, NM: National Solar Obs.), 67

———.1995, in Infrared Tools for Solar Astrophysics: What's Next, ed. J. R. Kuhn & M. J. Penn (Singapore: World Scientific), 303

———.2003, in ASP Conf. Ser. 286, Current Theoretical Models and High Resolution Solar Observations: Preparing for ATST, ed. A. A. Pevtsov & H. Uitenbroek (San Francisco: ASP), 419

———.2006, in SOHO 17, 10 Years of SOHO and Beyond, ed. H. Lacoste (ESA SP-617, CD ROM; Noordwijk: ESA)

———.2007a, in ASP Conf. Ser. 368, The Physics of Chromospheric Plasmas, ed. P. Heinzel, I. Dorotovič, & R. J. Rutten (San Francisco: ASP), 81

———.2007b, in Numerical Methods for Multidimensional Radiative Transfer, ed. E. Meinköhn, G. Kanschat, R. Rannacher, & R. Wehrse (Heidelberg: Springer), in press

Avrett, E. H., Chang, E. S., & Loeser, R. 1994a, in IAU Symp. 154, Infrared Solar Physics, ed. D. M. Rabin, J. T. Jefferies, & C. Lindsey (Dordrecht: Kluwer), 323

Avrett, E. H., Fontenla, J. M., & Loeser, R. 1994b, in IAU Symp. 154, Infrared Solar Physics, ed. D. M. Rabin, J. T. Jefferies, & C Lindsey (Dordrecht: Kluwer), 35

Avrett, E. H., Höflich, P., Uitenbroek, H., & Ulmschneider, P. 1996, in ASP Conf. Ser. 109, Cool Stars, Stellar Systems, and the Sun: 9th Cambridge Workshop, ed. R. Pallavicini & A. K Dupree (San Francisco: ASP), 105
Avrett, E. H., Kurucz, R. L., & Loeser, R. 2006, A&A, 452, 651
Avrett, E. H., & Loeser, R. 2003, in IAU Symp. 210, Modeling of Stellar Atmospheres, ed. W. Weise & N. Piskunov (Dordrecht: Kluwer), A-21
Avrett, E. H., Machado, M. E., & Kurucz, R. L. 1986, in The Lower Atmosphere of Solar Flares, ed. D. F. Neidig (Sunspot, NM: National Solar Obs.), 216
Ayres, T. R. 2002, ApJ, 575, 1104
———. 2003, in ASP Conf. Ser. 286, Current Theoretical Models and High Resolution Solar Observations: Preparing for ATST, ed. A. A. Pevtsov & H. Uitenbroek (San Francisco: ASP), 431
Ayres, T. R., Moos, H. W., & Linsky, J. L. 1981, ApJ, 248, L137
Ayres, T. R., & Wiedemann, G. 1989, ApJ, 338, 1033
Badnell, N. R., O'Mullane, M. G., Summers, H. P., Altun, Z., Bautista, M. A., Colgan, J., Gorczyca, T. W., Milnik, D. M., Pindzola, M. S., & Zatrarinny, O. 2003, A&A, 406, 1151
Baumüller, D., & Gehren, T. 1996, A&A, 307, 961
Bhatia, A. K., Kastner, S. O., & Behring, W. E. 1982, ApJ, 257, 887
Bocchialini, K., & Vial, J. C. 1994, A&A, 287, 233
Boreiko, R. T., & Clark, T. A. 1987, ApJ, 318, 445
Bowen, I. S. 1935, ApJ, 81, 1
Brekke, P. 1993a, ApJS, 87, 443
———.1993b, ApJ, 408, 735
Caccin, B., Gomez, M. T., & Severino, G. 1993, A&A, 276, 219
Carlsson, M. 2007, in ASP Conf. Ser. 368, The Physics of Chromospheric Plasmas, ed. P. Heinzel, I. Dorotovič, & R. J. Rutten (San Francisco: ASP), 49
Carlsson. M., & Judge, P. G. 1993, ApJ, 402, 344
Carlsson, M., Judge, P. G., & Wilhelm, K. 1997, ApJ, 486, L63
Carlsson, M., & Rutten, R. J. 1994, in IAU Symp. 154, Infrared Solar Physics, ed. D. M. Rabin, J. T. Jefferies, & C. Lindsey (Dordrecht: Kluwer), 341
Carlsson, M., & Stein, R. F. 1992, ApJ, 397, L59
———.1994, in Chromospheric Dynamics, ed. M. Carlsson (Oslo: Univ. Oslo, Inst. Theor. Astrophys.), 47
———.1995, ApJ, 440, L29
———.1997, ApJ, 481, 500
———.2002, ApJ, 572, 626
Chang, E. S., Avrett, E. H., & Loeser, R. 1991, A&A, 247, 580 (erratum 256, 724)
Chung, S., Lin, C. C., & Lee, E. T. P. 1993, Phys. Rev. A, 47, 3867
Clark, R. E. H., Abdallah, J., Jr., & Mann, J. B. 1991, ApJ, 381, 597
Cooper, J., Ballagh, R. J., & Hubeny, I. 1989, ApJ, 344, 949
Cox, D. P., & Tucker, W. H. 1969, ApJ, 157, 1157
Cram, L. E., & Damé, L. 1983, ApJ, 272, 355
Cuntz, M., Rammacher, W., & Musielak, Z. E. 2007, ApJ, 657, L57
Curdt, W., Brekke, P., Feldman, U., Wilhelm, K. Dwivedi, B. N., Schüle, U., & Lemaire, P. 2001, A&A, 375, 591
Curdt, W., & Heinzel, P. 1998, ApJ, 503, L95
Curdt, W., Heinzel, P., Schmidt, W., Tarbell, T., von Uexküll, & Wilken, V. 1999, in Magnetic Fields and Solar Processes, ed. A. Wilson (ESA SP-448; Noordwijk: ESA), 177
Degiacomi, C. G., Kneubühl, F. K., & Huguenin, D. 1985, ApJ, 298, 918
Dere, K. P., Landi, E., Mason, H. E., Monsignori Fossi, B. C., & Young, P. R. 1997, A&AS, 125, 149
Doschek, G. A., & Mariska, J. T. 2001, ApJ, 560, 420
Drawin, H. W. 1968, Z. Phys. 211, 404
———.1969, Z. Phys. 225, 483
Dunseath, K. M., Fon, W. C., Burke, V. M., Reid, R. H. G., & Noble, C. J. 1997, J. Phys. B, 30, 277
Dunseath, K. M., et al. 1993, JET Order JP2/11566
Fabbian, D., Asplund, M., Carlsson, M., & Kiselman, D. 2006, A&A, 458, 899
Feldman, U., Dammasch, I. E., & Wilhelm, K. 2001, ApJ, 558, 423
Feldman, U., Widing, K. G., & Warren, H. P. 1999, ApJ, 522, 1133 (erratum 529, 1145 [2000])
Ferguson, J. W., & Ferland, G. J. 1997, ApJ, 479, 363
Fon, W. C. et al. 1994, JET Order JP2/11566
Fontenla, J. M. 2005, A&A, 442, 1099
Fontenla, J. M., Avrett, E. H., & Loeser, R. 1990, ApJ, 355, 700
———.1991, ApJ, 377, 712
———.1993, ApJ, 406, 319
———.2002, ApJ, 572, 636
Fontenla, J. M., Avrett, E., Thuillier, G., & Harder, J. 2006, ApJ, 639, 441
Fontenla, J. M., Balasubramaniam, K. S., & Harder, J. 2007, in ASP Conf. Ser. 368, The Physics of Chromospheric Plasmas, ed. P. Heinzel, I. Dorotovič, & R. J. Rutten (San Francisco: ASP), 499
Fontenla, J., Reichmann, E. J., & Tandberg-Hanssen, E. 1988, ApJ, 329, 464
Fontenla, J., White, O. R., Fox, P. A., Avrett, E. H., & Kurucz, R. L. 1999, ApJ, 518, 480
Fossum, A., & Carlsson, M. 2005a, Nature, 435, 919
———.2005b, ApJ, 625, 556
———.2006, ApJ, 646, 579
Foukal, P. V. 2004, Solar Astrophysics (2d ed.; Weinheim: Wiley-VCH)
Fuhrmeister, B., Short, C. I., & Hauschildt, P. H. 2006, A&A, 452, 1083
Giovanardi, C., Natta, A., & Palla, F. 1987, A&AS, 70, 269
Giovanardi, C., & Palla, F. 1989, A&AS, 77, 157
Gnat, O., & Sternberg, A. 2007, ApJS, 168, 213
Gouttebroze, P. 1986, A&A, 160, 195
Grevesse, N., & Sauval, A. J. 2000, in Origin of Elements in the Solar System: Implications of Post-1957 Observations, ed. O. Manuel (New York: Kluwer), 261
Griffiths, N. W., Fisher, G. H., Woods, D. T., & Siegmund, O. H. W. 1999, ApJ, 512, 992
Hall, L. A., & Anderson, G. P. 1991, J. Geophys. Res., 96, 12927
Handy, B. N., et al. 1999, Sol. Phys., 187, 229
Hauschildt, P. H., Allard, F., & Baron, E. 1999, ApJ, 512, 377
Hauschildt, P. H., Baron, E., & Allard, F. 1997, ApJ, 483, 390
Heinzel, P., & Hubeny, I. 1985, in Progress in Stellar Spectral Line Formation Theory (Dordrecht: Reidel), 137
Hillier, D. J., & Miller, D. L. 1998, ApJ, 496, 407
Hubeny, I. 1985, Bull Astron. Inst. Czech., 36, 1
———.2003, in ASP Conf. Ser. 288, Stellar Atmospheric Modeling, ed. I. Hubeny, D. Mihalas, & K. Werner (San Francisco: ASP), 17
Hubeny, I., Hummer, D. G., & Lanz, T. 1994, A&A, 282, 151
Hubeny, I., & Lanz, T. 2003, in ASP Conf. Ser. 288, Stellar Atmospheric Modeling, ed. I. Hubeny, D. Mihalas, & K. Werner (San Francisco: ASP), 51
Hubeny, I., & Lites, B. W. 1995, ApJ, 455, 376
Hubeny, I., Oxenius, J., & Simonneau, E. 1983, J. Quant. Spectrosc. Radiat. Transfer, 29, 477
Hummer, D. G. 1962, MNRAS, 125, 21
Johnson, L. C. 1972, ApJ, 174, 227
Jordan, C., Bartoe, J.-D. F., Brueckner, G. E., Nicolas, K. R., Sandlin, G. D., & Van Hoosier, M. E. 1979, MNRAS, 187, 473
Judge, P. G. 2005, J. Quant. Spectrosc. Radiat. Transfer, 92, 479
Judge, P. G., Carlsson, M., & Stein, R. F. 2003, ApJ, 597, 1158
Judge, P. G., & Carpenter, K. G. 1998, ApJ, 494, 828
Judge, P. G., Tarbell, T. D., & Wilhelm, K. 2001, ApJ, 554, 424
Kalkofen, W. 2001, ApJ, 557, 376
Kalkofen, W., Ulmschneider, P., & Avrett, E. H. 1999, ApJ, 521, L141
Kariyappa, R., Varghese, B. A., & Curdt, W. 2001, A&A, 374, 691
Kastner, S. O., Behring, W. E., & Bhatia, A. K. 1983, ApJS, 53, 129
Kaulakys, B. 1985, J. Phys. B, 18, L167
———.1986, Sov. Phys.–JETP, 64, 229
Kazeminezhad, F., & Goodman, M. L. 2006, ApJS, 166, 613
Keenan, F. P., & Aggarwal, K. M 1989, ApJ, 344, 522
Keenan, F. P., Brekke, P., Byrne, P. B., & Greer, C. J. 1995, MNRAS, 276, 915
Kingdon, J. B., & Ferland, G. J. 1996, ApJS, 106, 205
Kneer, F. 1980, A&A, 87, 229
Koncewicz, R., & Jordan, C. 2007, MNRAS, 374, 220
Kurucz, R. L. 1991, in Solar Interior and Atmosphere, ed. A. N. Cox, W. C. Livingston, & M. S. Matthews (Tucson: Univ. Arizona Press), 663
Kurucz, R. L., van Dishoeck, E. F., & Tarafdar, S. P. 1987, ApJ, 322, 992
Landi, E., Del Zanna, G., Young, P. R., Dere, K. P., Mason, H. E., & Landini, M. 2006, ApJS, 162, 261
Leenaarts, J., & Wedemeyer-Böhm, S. 2006, in ASP Conf. Ser. 354, Solar MHD: Theory and Observations: A High Spatial Resolution Perspective, ed. J. Leibacher, R. F. Stein, & H. Uitenbroek (San Francisco: ASP), 306
Leenaarts, J., Wedemeyer-Böhm, S., Carlsson, M., & Hansteen, V. H. 2007, in ASP Conf. Ser. 368, The Physics of Chromospheric Plasmas, ed. P. Heinzel, I. Dorotovič, & R. J. Rutten (San Francisco: ASP), 103
Lemaire, P., Gouttebroze, P., Vial, J. C., & Artzner, G. E. 1981, A&A, 103, 160
Lites, B. W., & Mihalas, D. 1984, Sol. Phys., 93, 23
Lites, B. W., Shine, R. A., & Chipman, E. G. 1978, ApJ, 222, 333
Loukitcheva, M., Solanki, S. K., Carlsson, M., & Stein, R. F. 2004, A&A, 419, 747
Luo, D., & Pradhan, A. K. 1989, J. Phys. B, 22, 3377
Maltby, P., Avrett, E. H., Carlsson, M., Kjeldseth-Moe, O., Kurucz, R. L., & Loeser, R. 1986, ApJ, 306, 284
Mauas, P. J. D. 2007, in ASP Conf. Ser. 368, The Physics of Chromospheric Plasmas, ed. P. Heinzel, I. Dorotovič, & R. J. Rutten (San Francisco: ASP), 203
Mauas, P. J. D., Andretta, V., Falchi, A., Falciani, R., Tericca, L., & Cauzzi, G. 2005, ApJ, 619, 604
Mauas, P. J. D., Borda, R. F., & Luoni, M. L. 2002, ApJS, 142, 285
McCrea, W. H. 1929, MNRAS, 89, 718

Meier, R. R. 1995, ApJ, 452, 462 (erratum 468, 455)

Miller-Ricci, E., & Uitenbroek, H. 2002, ApJ, 566, 500

Moore, C. E. 1993, in Tables of Specta of Hydrogen, Carbon, Nitrogen, and Oxygen Atoms and Ions, ed. J. W. Gallagher (Boca Raton: CRC Press)

Nieva, M. F., & Przybilla, N. 2006, ApJ, 639, L39

Noyes, R. W., & Hall, D. N. B. 1972, ApJ, 176, L89

Oxenius, J. 1965, J. Quant. Spectrosc. Radiat. Transfer, 5, 771

Pequignot, D., & Aldrovandi, S. M. V. 1976, A&A, 50, 141

Pinfield, D. J., Mathioudakis, M., Keenan, F. P., Phillips, K. J. H., & Curdt, W. 1998, A&A, 340, L15

Przybilla, N., & Butler, K. 2004a, ApJ, 609, 1181

———.2004b, ApJ, 610, L61

Przybilla, N., Butler, K., Becker, S. R., Kudritzki, R. P., & Venn, K. A. 2000, A&A, 359, 1085

Przybilla, N., Butler, K., & Kudritzki, R. P. 2001, A&A, 379, 936

Przybilla, N., Kudritzki, R.-P., Butler, K., & Becker, S. R. 2003, in ASP Conf. Ser. 304, CNO in the Universe, ed. C. Charbonnel, D. Schaerer, & G. Meynet (San Francisco: ASP), 35

Rau, A. P. R. 1971, Phys. Rev. A, 4, 207

Rutten, R. J. 2007, in ASP Conf. Ser. 368, The Physics of Chromospheric Plasmas, ed. P. Heinzel, I. Dorotovič, & R. J. Rutten (San Francisco: ASP), 27

Rutten, R. J., & Carlsson, M. 1994, in IAU Symp. 154, Infrared Solar Physics, ed. D. M. Rabin, J. T. Jefferies, & C. Lindsey (Dordrecht: Kluwer), 309

Samain, D. 1978, Ph.D. thesis, Univ. Paris

———.1980, ApJS, 44, 273

Scholz, T. T., & Walters, H. R. J. 1991, ApJ, 380, 302

Scholz, T. T., Walters, H. R. J., Burke, P. G., & Scott, M. P. 1990, MNRAS, 242, 692

Schmidt, W., Knölker, M., & Westendorp Plaza, C. 1994, A&A, 287, 229

Schrijver, C. J. 1995, A&A Rev., 6, 181

Seaton, M. H. 1962, Proc. Phys. Soc., 79, 1105

Shah, M. B., Elliott, D. S., & Gilbody, H. B. 1987, J. Phys. B, 20, 3501

Short, C. I., & Hauschildt, P. H. 2005, ApJ, 618, 926

Sigut, T. A. A. 1996, ApJ, 473, 452

Socas-Navarro, H., & Norton, A. A. 2007, ApJ, 660, L153

Steenbock, W., & Holweger, H. 1984, A&A, 130, 319

Sturrock, P. A., Holzer, T. E., & Ulrich, R. K., eds. 1986, Physics of the Sun, Vol. 2 (Dordrecht: Reidel)

Suno, H., & Kato, T. 2006, At. Data Nucl. Data Tables, 92, 407

Tayal, S. S. 2003, ApJ, 582, 550

Thompson, W. R., Shah, M. B., & Gilbody, H. B. 1995, J. Phys. B, 28, 1321

Uitenbroek, H. 2001, ApJ, 557, 389

Ulmschneider, P., Rammacher, W., Musielak, Z. E., & Kalkofen, W. 2005, ApJ, 631, L155

van Regemorter, H. 1962, ApJ, 136, 906

Vernazza, J. E., Avrett, E. H., & Loeser, R. 1981, ApJS, 45, 635 (VAL)

Verner, D. A., Ferland, G. J., Korista, K. T., & Yakolev, D. G. 1996, ApJ, 465, 487

Vial, J. C., Lemaire, P., Artzner, G., & Gouttebroze, P. 1980, Sol. Phys., 68, 187

Voronov, G. S. 1997, At. Data Nucl. Data Tables, 65, 1

Vriens, L., & Smeets, A. H. M. 1980, Phys. Rev. A, 22, 940

Wahlstrom, C., & Carlsson, M. 1994, ApJ, 433, 417

Warren, H. P., Mariska, J. T., & Wilhelm, K. 1998, ApJS, 119, 105

Warren, H. P., Mariska, J. T., Wilhelm, K., & Lemaire, P. 1997, ApJ, 484, L91

Warren, H. P., & Winebarger, A. R. 2000, ApJ, 535, L63

Wedemeyer, S., Freytag, G., Steffen, M., Ludwig, H.-G., & Holweger, H. 2004, A&A, 414, 1121

Wedemeyer-Böhm, S., & Steffen, M. 2007, A&A, 462, L31

White, O. R. 1963, ApJ, 138, 1316

Wilhelm, K., & Kalkofen, W. 2003, A&A, 408, 1137

Wilhelm, K., Schüle, U., Curdt, W., Hilchenbach, M., Marsch, E., Lemaire, P., Bertaux, J.-L., Jordan, S. D., & Feldman, U. 2005, A&A, 439, 701

Wilson, N. J., Bell, K. L., & Hudson, C. E. 2005, A&A, 432, 731

Yelnik, J.-B., Burnett, K., Cooper, J., Ballagh, R. J., & Voslamber, D. 1981, ApJ, 248, 705

Zatsarinny, O., & Tayal, S. S. 2003, ApJS, 148, 575

Zirin, H. 1975, ApJ, 199, L63